

**DESIGN AND OPTIMIZATION OF A MICROFLUIDIC SYSTEM
FOR THE PRODUCTION OF PROTEIN DRUG LOADABLE
AND MAGNETICALLY TARGETABLE BIODEGRADABLE
MICROSPHERES**

by

Mehrdad Bokharaei

M.Sc., The University of Western Ontario, 2009

A THESIS SUBMITTED IN PARTIAL FULFILLMENT OF
THE REQUIREMENTS FOR THE DEGREE OF

DOCTOR OF PHILOSOPHY

In

THE FACULTY OF GRADUATE AND POSTDOCTORAL STUDIES

(Pharmaceutical Sciences)

THE UNIVERSITY OF BRITISH COLUMBIA

(Vancouver)

April 2016

© Mehrdad Bokharaei, 2016

Abstract

The overall goal of this dissertation was to develop a microfluidic system for the production of magnetic and non-magnetic drug-loaded polymer microspheres with narrow size distribution. The size of microspheres is a crucial parameter for their application, as the rate of drug release from the microspheres, the rate of microsphere degradation, and the microsphere biodistribution all correlate with particle size and size distribution. Conventional microsphere production methods generally lead to the formation of particles with broad size distribution. In this work, the conventional emulsification-evaporation method for the production of microspheres was miniaturized into microfluidic flow focusing system.

Using a self-designed flow focusing chip, quasi-monodisperse poly (lactic acid) microspheres were prepared. The spherical shape and narrow size distribution of the initial polymer-chloroform droplets generated at the orifice were retained throughout their movement in the channels. After complete solvent removal, the droplets turned into quasi-monosized microspheres with a coefficient of variation between 2% and 16%. To better understand the influence of different parameters on droplet generation, the behavior of the disperse phase and the continuous phase were simulated in a 3D computational multiphase droplet generation model. The experimentally determined droplet sizes correlated well with the computational model and never digressed more than 17% from the simulations.

The flow focusing system was then also used directly, for the first time, to produce superparamagnetic microspheres containing 15% magnetic nanoparticles. The microspheres' thermal properties showed their suitability for magnetic hyperthermia of large tumors in cancer therapy.

The microfluidic chip was then further altered into a novel device that is able to encapsulate proteins into the polymer microspheres by integrating flow focusing and passive droplet break up systems into one-chip which contained sections of differing surface properties. With this design, bovine serum albumin-loaded microspheres could be prepared with a protein encapsulation efficiency of up to 96%.

The work presented in this dissertation is the first to show that a microfluidic system can be used for the continuous production of quasi-monodisperse magnetic microspheres and protein-drug-loaded polymer microspheres. These microspheres will be useful in hyperthermia treatment, diagnostic imaging, and the targeted and controlled delivery of protein based drugs.

Preface

The principle author of this dissertation is **Mehrdad Bokharaei** who designed, performed and analyzed all the experiments and experimental data under the supervision of **Dr. Urs Häfeli**, who is the principal investigator for this project.

The project was done in collaboration with other researchers. Their contribution is explained below:

Chapter 2

Dr. Katayoun Saatchi synthesized the ^{99m}Tc chelator used in the lung perfusion and liver radioembolization study. The results of the lung perfusion study have been published in the journal of Biomacromolecules.

Häfeli UO, Saatchi K, Elischer P, Misri R, Bokharaei M, Labiris NR, Stoeber B (2010). *Lung perfusion imaging with monosized biodegradable microspheres*. Biomacromol **11**, 561-567.

Chapter 3

Dr. Thomas Schneider's expertise was invaluable for the simulation of droplet generation in the microfluidic system. Dr. Schneider did the coding and computational modeling, while the principal author came up with the experimental design and the analyses. The author also received technical advice from Dr. Schneider in the interpretation of the simulation data.

Chapter 4

Dr. O Thompson Mefford and **Dr. Roland Stone** synthesized and characterized the magnetic nanoparticles used in the magnetic microsphere production.

Dr. Silvio Dutz performed the thermal analysis of the fabricated magnetic microspheres. He also contributed to the data analysis and interpretation of the data.

The results of the chapters 2, 3, and 4 have been presented in several scientific conferences and have also been published in the Journal of Microfluidics and Nanofluidics.

Bokharaei M, Schneider T, Dutz S, Mefford OT, Stone R., Häfeli UO (2016). *Production of monodispersed magnetic polymeric microspheres in a microfluidic chip and 3D simulation*, Microfluidics and Nanofluidics, **20(1)**, DOI: 10.1007/s10404-015-1693-y.

Chapter 5

All the work in this chapter, including the chip design and fabrication, experimental design, experimental performance, and interpretation of data was done by **Mehrdad Bokharaei**. The results are currently being prepared for submission to a peer-reviewed journal.

Table of Contents

Abstract	ii
Preface	iv
Table of Contents.....	vi
List of Tables.....	xi
List of Figures	xii
List of Abbreviations.....	xxii
List of Symbols.....	xxiv
Acknowledgments.....	xxvii
Dedication.....	xxviii
Chapter 1: Background and Literature Review	1
1.1 Polymers in Pharmaceutical Sciences	1
1.1.1 Biodegradable Polymers in Drug Delivery	4
1.1.2 Mechanism of Microsphere Production from Poly(α -Ester) Polymers	7
1.1.3 Importance of Monodispersity	12
1.2 Microfluidics	14
1.2.1 Dimensionless Numbers in Microfluidics	14
1.2.2 Droplet Generation in Microfluidic Devices	17
1.3 Mixing in Microfluidic Systems.....	24
1.3.1 Passive Micromixers.....	25
1.4 Research Hypothesis.....	28

1.4.1	Specific Aim 1 (Chapter 2 and 3):	29
1.4.2	Specific Aim 2 (Chapter 4):	29
1.4.3	Specific Aim 3 (Chapter 5):	29
Chapter 2: Production of Non-Magnetic Polymer Microspheres		30
2.1	Material and Methods	31
2.1.1	Glass Chip Fabrication.....	31
2.1.2	Polymeric Microsphere Production	33
2.1.3	Microsphere Size Distribution Analysis	33
2.1.4	Scanning Electron Microscopy	34
2.2	Results and Discussion	34
2.2.1	Choice of Material for Chip Fabrication.....	34
2.2.2	Production of Quasi-Monosized Polymer Microspheres	35
2.2.3	Preparation of PEGylated Monosized PLLA Microspheres	44
2.2.4	Morphology of Produced PLLA Microspheres	49
2.3	Monosized PLLA Microspheres Production for Medical Applications.....	50
2.3.1	Diagnostic Lung Perfusion Imaging	50
2.3.2	Therapeutic Liver Radioembolization	53
2.4	Conclusions	60
Chapter 3: Three-Dimensional Computational Simulation of Droplet Generation in our Microfluidics Flow Focusing System.....		62
3.1	Introduction	62
3.2	Computational Flow Modeling and Data Analysis	64

3.2.1	Computational Fluid Dynamics	64
3.2.2	On-chip Droplet Generation	65
3.2.3	Droplet Size Distribution Analysis	65
3.3	Results and Discussion	66
3.3.1	Comparison to the Experimental Microsphere Production.....	66
3.3.2	Effect of Flow Rate on Droplet Size.....	69
3.4	Conclusions	76

Chapter 4: Encapsulation of Magnetic Nanoparticles in Polymer

Microspheres Using the Microfluidic Flow Focusing System77

4.1	Introduction	77
4.2	Material and Methods	79
4.2.1	Magnetic Nanoparticles	79
4.2.2	Magnetic Microsphere Production.....	79
4.2.3	Microsphere Size Distribution Analysis	79
4.2.4	Scanning Electron Microscopy	80
4.2.5	Thermal Property Measurement	80
4.3	Results and Discussion	80
4.3.1	Selection of Magnetic Nanoparticles	80
4.3.2	Magnetic Microsphere Production.....	82
4.3.3	Morphology of the Magnetic Microspheres	90
4.4	Conclusions	92

Chapter 5: Encapsulation of Protein in Polymer Microspheres using a

Microfluidic System94

5.1	Introduction	94
5.2	Material and Methods	99
5.2.1	Fabrication of the Double Emulsion Generating Microfluidic System	99
5.2.2	Coating of the Chip	101
5.2.3	Protein Loaded Microsphere Production	102
5.2.4	Protein Labeling	102
5.2.5	Protein Encapsulation Efficiency	104
5.3	Results and Discussion	104
5.3.1	Microchip Surface Coating	104
5.3.2	Protein Encapsulation in Microfluidic System	105
5.4	Conclusions	114

Chapter 6: Summary, Conclusions and Suggestions for Future Work.....115

6.1	Summary	115
6.1.1	Production of Polymer Microspheres in a Microfluidic Flow Focusing System..	116
6.1.2	Computational Modeling of Droplet Generation in Microfluidic Flow Focusing System	118
6.1.3	Encapsulation of Magnetic Nanoparticles in Quasi-Monodisperse Polymer Microspheres	118
6.1.4	Encapsulation of BSA in PLLA Quasi-Monodisperse Microspheres.....	119
6.2	Contributions	119
6.3	Conclusions	120

6.4	Suggestions for Future Work.....	121
References	123

List of Tables

Table 1-1. Molecular structure of some biodegradable polymers typically used for the production of microparticles.	3
Table 2-1. Common wafer materials used for microfluidic system microfabrication and criteria considered for selecting a suitable material for our work.	35
Table 2-2. Size and size distribution of PLLA microspheres produced at different flow rates. Size of the particles was determined after complete solvent removal in at least 200 microspheres per experiment.	36
Table 2-3. Activity distribution of the ^{99m}Tc-Microspheres 15 Min after Tail Vein Injection into C57Bl/6 Mice (n = 6).	53
Table 3-1: Simulation results of droplet formation in the microfluidic flow focusing system and comparison of results from simulations with experiments.	67
Table 4-1. Size distribution of the PLLA microsphere loaded with iron oxide magnetic nanoparticles. In all experiments, the continuous phase was 2% PVA in water and the dispersed phase 20 mg PLLA and 9.58 mg of MNPs in 250 μL of chloroform.	83
Table 4-2. Magnetic and thermal properties of PLLA magnetic microspheres (MMS).	90
Table 5-1. Comparison of encapsulation efficiency of the BSA in PLLA microspheres using the double emulsion generating microfluidic system at different IP and CP flow rates.	111

List of Figures

Figure 1-1. Schematic of polymer microcapsules and polymer microspheres structure	2
Figure 1-2. Lactic acid cyclic dimer ring opening polymerization.....	5
Figure 1-3. Molecular structure of lactic acid and lactide enantiomers.....	6
Figure 1-4. Poly(lactic-co-glycolic acid) synthesis by random ring-opening copolymerization.	6
Figure 1-5. Synthesis of poly(ϵ-caprolactone) through ring opening polymerization.....	7
Figure 1-6. Schematic diagram for the production of polymer microspheres by the phase separation method.....	8
Figure 1-7. Schematic diagram of a spray drying system used for the production of dry powders / microspheres.....	10
Figure 1-8. Polymer microsphere production steps in emulsification and solvent extraction / evaporation method.....	11
Figure 1-9. Schematic diagram of droplet generation in T-junction microfluidic system. a) Squeezing regime, b) dripping regime.	18
Figure 1-10. Schematic image of droplet generation in co-flowing system. (a) Dripping regime when $Ca < 1$, (b) Jetting regime at high $Ca > 1$, (c) widening jet when flow rate of dispersed phase is bigger than flow rate of continuous phase. Redrawn from [34]......	20
Figure 1-11. Schematic of a microfluidic flow focusing system. Parameters marked on the image are the ones used in equations 1-13 and 3-1.....	22

Figure 1-12. Schematic image of droplet generation in flow focusing system under (a) geometry-controlled regime and (b) dripping regime. Redrawn from Anna and Mayer (2006).....22

Figure 1-13. Schematic image of droplet generation under (a) jetting regime and (b) tip-streaming regime. Redrawn from Anna and Mayer [38].24

Figure 1-14. Schematic design of single lamination systems with (a) T-shaped and (b) Y-shaped inlets. Redrawn from [43].25

Figure 1-15. Schematic design of herringbone structure. Redrawn from [50].27

Figure 1-16. Schematic design of a micromixer with slanted groove at the bottom and barriers on the top. Redrawn from [51].28

Figure 2-1 : Schematic diagram of droplet generation in a microfluidic flow focusing system. Blue color indicates continuous aqueous phase, red color the disperse polymer solution phase.30

Figure 2-2: a) Fabrication process for the microfluidic flow focusing glass chip. Briefly, a 100 mm glass wafer was coated with chromium, gold, and a positive photoresist (a.1). After pattern transformation, coating was removed from the pattern area (a.2) and the photoresist was removed from the whole wafer (a.3). The glass was etched with highly concentrated HF (a.4) followed by removing all coated materials (a.5). The wafer was cut into 50×150 mm² slices and bonded onto another glass wafer of the same size to cover the channels. b) Fabricated glass chip after bonding. c) Glass chip and connectors used in all experiments. d) Schematic diagram of microfluidic design and channel dimensions on the mask before etching. e) Depth profile of the channels after etching.32

Figure 2-3: Droplet generation in the designed microfluidic flow focusing system. CP was aqueous 2% PVA and its flow rate was 30 $\mu\text{L}/\text{min}$. DP was 10% PLLA in chloroform and its flow rate was 1 $\mu\text{L}/\text{min}$38

Figure 2-4. Microscopic pictures and size distribution of PLLA microspheres produced in a glass microfluidic flow focusing system. CP is 1% PVA and its flow rate is 100 $\mu\text{L}/\text{min}$ and DP is 2% PLLA and its flow rate is 0.5 $\mu\text{L}/\text{min}$. The Y-axis shows the number weighted microsphere fractions.40

Figure 2-5. Microscopic pictures and size distribution of PLLA microspheres produced in a glass microfluidic flow focusing system. CP is 2% PVA and its flow rate is 80 $\mu\text{L}/\text{min}$ and DP is 10% PLLA and its flow rate is 1 $\mu\text{L}/\text{min}$. The Y-axis shows the number weighted microsphere fractions.41

Figure 2-6. Microscopic pictures and size distribution of PLLA microspheres produced in a glass microfluidic flow focusing system. CP is 2% PVA and its flow rate is 60 $\mu\text{L}/\text{min}$ and DP is 10% PLLA and its flow rate is 1 $\mu\text{L}/\text{min}$. The Y-axis shows the number weighted microsphere fractions.42

Figure 2-7. Microscopic pictures and size distribution of PLLA microspheres produced in a glass microfluidic flow focusing system. CP is 2% PVA and its flow rate is 30 $\mu\text{L}/\text{min}$ and DP is 10% PLLA and its flow rate is 1 $\mu\text{L}/\text{min}$. The Y-axis shows the number weighted microsphere fractions.43

Figure 2-8. Microscopic pictures and size distribution of pegylated PLLA microspheres with narrow size distribution produced in a glass microfluidic flow focusing system. The continuous phase was 2% PVA in water and its flow rate was 120 $\mu\text{L}/\text{min}$. Dispersed phase was 10% polymer in chloroform and its flow rate was 1 $\mu\text{L}/\text{min}$45

Figure 2-9. Microscopic pictures and size distribution of pegylated PLLA microspheres with narrow size distribution produced in a glass microfluidic flow focusing system. The continuous phase was 2% PVA in water and its flow rate was 120 $\mu\text{L}/\text{min}$. Dispersed phase was 10% polymer (95 % PLLA and 5% mPEG-b-PDLA) in chloroform and its flow rate was 1 $\mu\text{L}/\text{min}$46

Figure 2-10. Microscopic pictures and size distribution of pegylated PLLA microspheres with narrow size distribution produced in a glass microfluidic flow focusing system. The continuous phase was 2% PVA in water and its flow rate was 120 $\mu\text{L}/\text{min}$. Dispersed phase was 10% polymer (75 % PLLA and 25% mPEG-b-PDLA) in chloroform and its flow rate was 1 $\mu\text{L}/\text{min}$47

Figure 2-11. Microscopic pictures and size distribution of pegylated PLLA microspheres with narrow size distribution produced in a glass microfluidic flow focusing system. The continuous phase was 2% PVA in water and its flow rate was 120 $\mu\text{L}/\text{min}$. Dispersed phase was 10% polymer (50 % PLLA and 50% mPEG-b-PDLA) in chloroform and its flow rate was 1 $\mu\text{L}/\text{min}$48

Figure 2-12 : Effect of mPEG-PDLLA concentration in polymer blend on average particles size of the microspheres produced in the microfluidic flow focusing system. The flow rate of the continuous phase was 120 $\mu\text{L}/\text{min}$ and that of the dispersed phase 1 $\mu\text{L}/\text{min}$49

Figure 2-13 : Scanning electron microscopy images of PLLA microspheres. .50

Figure 2-14 : Size distribution and scanning electron microscopy (SEM) of the biodegradable PLLA microspheres.52

Figure 2-15. Volume-rendered microSPECT/CT image taken 5 minutes after tail vein injection of 0.2 mg of the $^{99\text{m}}\text{Tc}$ -radiolabeled microspheres into a healthy mouse. The radioactivity is shown in red.....52

Figure 2-16. Microscopic pictures and size distribution of large PLLA microspheres with narrow size distribution produced in a glass microfluidic flow focusing system. Continuous phase was aqueous 2% PVA and its flow rate was 20 $\mu\text{L}/\text{min}$. The dispersed phase was 16% PLLA in chloroform and its flow rate was 3 $\mu\text{L}/\text{min}$55

Figure 2-17. Microscopic pictures and size distribution of large PLLA microspheres with narrow size distribution produced in a glass microfluidic flow focusing system. Continuous phase was aqueous 2% PVA and its flow rate was 20 $\mu\text{L}/\text{min}$. The dispersed phase was 16% PLLA in chloroform and its flow rate was 2 $\mu\text{L}/\text{min}$56

Figure 2-18. Microscopic pictures and size distribution of large PLLA microspheres with narrow size distribution produced in a glass microfluidic flow focusing system. Continuous phase was aqueous 2% PVA and its flow rate was 20 $\mu\text{L}/\text{min}$. The dispersed phase was 16% PLLA in chloroform and its flow rate was 1 $\mu\text{L}/\text{min}$57

Figure 2-19. Microscopic pictures and size distribution of large PLLA microspheres with narrow size distribution produced in a glass microfluidic flow focusing system. Continuous phase was aqueous 2% PVA and its flow rate was 20 $\mu\text{L}/\text{min}$. The dispersed phase was 16% PLLA in chloroform and its flow rate was 0.5 $\mu\text{L}/\text{min}$58

Figure 2-20 : Size distribution of PLLA microspheres coated with $^{99\text{m}}\text{Tc}$ chelator and PEG fabricated for radioembolization study. The concentration of polymer in chloroform was 20% (w/v) and the polymer composition was 92% PLLA, 5% $^{99\text{m}}\text{Tc}$ chelator and 3% pegylated polymer. DP flow rate was 1 $\mu\text{L}/\text{min}$. The continuous phase consisted of 2% PVA at a flow rate of 20 $\mu\text{L}/\text{min}$59

Figure 3-1. Comparison of experimental and simulated droplet generation in the microfluidic chip.68

Figure 3-2. 3D simulation of sequential droplet generation in our microfluidic flow focusing system under geometry controlled conditions. Shown are the top-view of the channel with DP shown in red and CP shown in blue (see volume fraction legend). Flow rates used in the simulation were: $Q_{CP} = 5 \mu\text{L} / \text{min}$, $Q_{DP} = 0.1 \mu\text{L} / \text{min}$71

Figure 3-3. 3D simulation of sequential droplet generation in our microfluidic flow focusing system under geometry controlled conditions. Shown are the top-view of the channel with DP shown in red and CP shown in blue (see volume fraction legend). Flow rates used in the simulation were: $Q_{CP} = 10 \mu\text{L} / \text{min}$, $Q_{DP} = 0.1 \mu\text{L} / \text{min}$72

Figure 3-4. 3D simulation of sequential droplet generation in our microfluidic flow focusing system. Droplet generation is in transition to dripping regime. Shown are the top-view of the channel with DP shown in red and CP shown in blue (see volume fraction legend). Flow rates used in the simulation were: $Q_{CP} = 50 \mu\text{L} / \text{min}$, $Q_{DP} = 0.1 \mu\text{L} / \text{min}$73

Figure 3-5. 3D simulation of the sequential droplet generation in our microfluidic flow focusing system under geometry controlled conditions. Shown are the top-view of the channel with DP shown in red and CP shown in blue (see volume fraction legend). Flow rates used in the simulation were: $Q_{CP} = 20 \mu\text{L} / \text{min}$, $Q_{DP} = 1 \mu\text{L} / \text{min}$74

Figure 3-6. 3D simulation of the sequential droplet generation in our microfluidic flow focusing in a transition to jetting condition. Shown are the top-view of the channel with DP shown in red and CP shown in blue (see

volume fraction legend). Flow rates used in the simulation were: QCP = 100 $\mu\text{L} / \text{min}$, QDP = 1 $\mu\text{L} / \text{min}$75

Figure 4-1: Size distribution analysis and microscopic images of the magnetic microspheres produced in a glass microfluidic flow focusing system at CP = 30 $\mu\text{L}/\text{min}$ and DP = 0.3 $\mu\text{L}/\text{min}$. Continuous phase was 2% PVA dissolved in water and dispersed phase was 20 mg PLLA and 9.58 mg MNPs dissolved in 250 μL chloroform.84

Figure 4-2: Size distribution analysis and microscopic images of the magnetic microspheres produced in a glass microfluidic flow focusing system at CP = 60 $\mu\text{L}/\text{min}$ and DP = 0.3 $\mu\text{L}/\text{min}$. Continuous phase was 2% PVA dissolved in water and dispersed phase was 20 mg PLLA and 9.58 mg MNPs dissolved in 250 μL chloroform.85

Figure 4-3: Size distribution analysis and microscopic images of the magnetic microspheres produced in a glass microfluidic flow focusing system at CP =40 $\mu\text{L}/\text{min}$ and DP = 0.3 $\mu\text{L}/\text{min}$. Continuous phase was 2% PVA dissolved in water and dispersed phase was 20 mg PLLA and 9.58 mg MNPs dissolved in 250 μL chloroform.86

Figure 4-4: Size distribution analysis and microscopic images of the magnetic microspheres produced in a glass microfluidic flow focusing system at CP = 60 $\mu\text{L}/\text{min}$ and DP = 1 $\mu\text{L}/\text{min}$. Continuous phase was 2% PVA dissolved in water and dispersed phase was 20 mg PLLA and 9.58 mg MNPs dissolved in 250 μL chloroform.87

Figure 4-5 : Hysteresis curve of dry MMS confirms their superparamagnetic behavior as well as a magnetic concentration of about 20% by mass.89

Figure 4-6. Scanning electron microscopy images of PLLA microspheres. Continuous phase was 2% PVA in water and disperse phase was 20 mg PLLA and 9.8 mg MNPs in 250 μ L chloroform. The particles were produced at (a) CP = 60 μ L/min and DP = 1 μ L/min and (b) CP = 40 μ L/min and DP = 0.3 μ L/min.91

Figure 5-1: Different designs for performing double emulsion in microfluidic chip. (a) double T-junction system purposed by Okushima et al. [125], (b) single flow focusing system purposed by Utada et al. [126], (c) single flow focusing system purposed by Abbaspourrad et al. [122], (d) multiple flow focusing- co-flowing system for single or multiple core droplet generation purposed by Chu et al. [124], (e) single flow focusing system for multi-core droplet generation purposed by Adams et al. [123], and (f) Drop-pairing system for core-shell droplet generation proposed by Deng et al. [128].....98

Figure 5-2. Schematic microfabrication process of the microfluidic system for double emulsion generation system. A 100 mm glass wafer was coated with chromium, gold, and a positive photoresist (a.1). After microfluidic flow focusing pattern transformation, coating was removed from the pattern area (a.2) and the photoresist was removed from the whole wafer (a.3). The glass was etched with highly concentrated HF (a.4). The wafer was coated with the positive photoresist again (a.5). FF-PDB pattern on mask 1 is transferred and then photoresist in removed (a.6). Channels were etched by submerging the wafer into high concentration of HF solution (a.7) followed by removing all coated materials (a.8). The wafer was cut into 50 \times 15 mm² slices and bonded onto another glass wafer of the same size to cover the channels. (b) Fabricated microfluidic glass chip before bonding.100

Figure 5-3. Molecular structure of 1H, 1H, 2H, 2H-perfluorododecylchlorosilane.....101

Figure 5-4. Protein standard curve. Known concentration of BSA labelled with Alexa 555 (BSA-A555) was diluted in 5% SDS in 0.1 N NaOH solution. The fluorescent intensity of the solutions was measured at 550 nm and 585 nm excitation and emission wavelength, respectively.....103

Figure 5-5. Self-assembly mechanism of PFDTCS coating on the glass surface [131].105

Figure 5-6. Water droplets on the microfluidic glass chip (a) coated with PFDTCS, and (b) uncoated.105

Figure 5-7: Schematic diagram of the double emulsion generating microfluidic system used for BSA encapsulation in PLLA microsphere.106

Figure 5-8. (a) Light microscope image of double emulsion generation in the microfluidic system. (b-d) Bright field and fluorescent microscopy images of the PLLA microspheres that show successful encapsulation of the dye inside the polymer microspheres. (b) Bright field image of the microsphere. (c) Fluorescent image of the particles. The excitation wavelength was ~490 nm. (d) Superimposed image of the particles. The inner phase was fluorescein sodium dye dissolved in water and its flow rate was 0.2 μ L/min, the dispersed phase is 10% PLLA in chloroform and 10% Span 80 and its flow rate was 0.8 μ L/min, and the CP was 2% PVA and its flow rate was 30 μ L/min.....108

Figure 5-9: A snapshot of passive droplet break up section of the double emulsion generation microfluidic system that shows the phase separation between IP and DP when Span concentration is 1% (v/v).....110

Figure 5-10. Protein encapsulation efficiency in PLLA microsphere produced at different CP flow rate. In all experiments, inner phase was 5.4 mg/mL BSA-A555 in PBS and IP flow rate was 0.05 μ L/min, disperse phase was 10% (PLLA and PEG-PCL in 96 to 4 mass ratio) in chloroform and 4%(v/v) Span 80 and DP flow rate was 1 μ L/min, and CP was 2% PVA in water.111

List of Abbreviations

Anti-VEGF	Anti-vascular endothelial growth factor
BSA	Bovine serum albumin
CMC	Critical micelle concentration
CP	Continuous phase
CT	Computed tomography
DMSO	Dimethyl sulfoxide
DP	Dispersed phase
FDA	United States Food and Drug Administration
FEP	Fluorinated ethylene propylene
HCC	Hepatocellular carcinoma
I.D.	Inner diameter
IP	Inner phase
MAA	Macroaggregated human albumin
MMS	Magnetic microsphere(s)
MNP	Magnetic nanoparticle(s)
O.D.	Outer diameter
O/W/O	Oil-in-water-in-oil
PBS	Phosphate buffered saline
PCL	Poly (ϵ -caprolactone)
PDLLA	Poly (D,L-lactic acid)

PEG	Poly (ethylene glycol)
PEI	Poly(ethylene imine)
PFDTCS	1H, 1H, 2H, 2H-Perfluorododecyltrichlorosilane
PLA	Poly (lactic acid)
PLGA	Poly(lactic-co-glycolic acid)
PLLA	Poly (L-lactic acid)
PVA	Poly(vinyl alcohol)
SAM	Self-assembled mechanism
SAR	Specific absorption rate
SDS	Sodium dodecyl sulphate
SEM	Scanning electron microscope
SPECT	Single photon emission computed tomography
VOF	Volume of fluid
W/O/W	Water-in-oil-in-water

List of Symbols

μ_i	Viscosity of fluid
M_1^t	Mass of drug released from the particles at time t
M_1^∞	Mass of drug released from the particles at equilibrium
v_i	Average velocity of fluid
ρ_i	Density of fluid
μ	Fluid viscosity
μ_{CP}	Viscosity of continuous phase
μ_{DP}	Viscosity of disperse phase
^{90}Y	Yttrium radioisotope with 64.1 h half life
^{99m}Tc	Metastable isotope of technetium-99 with 6 h half life
a	Characteristic length
A	Cross sectional area
a_0	Initial radius of sphere
B_0	Magnetic field
Bo	Bond number
C_0	Initial concentration of solute in microsphere
Ca	Capillary number
C_{CP}	Surfactant concentration in continuous phase
C_{DP}	Polymer concentration in disperse phase
C_s	Solute concentration in solid phase
CV	Coefficient of variation
CV _n	Number based coefficient of variation
CV _{Pr}	Coefficient of variation of primary diameter
CV _v	Volume based coefficient of variation
d	Capillary diameter
D	Diffusion coefficient
D_e	Diffusivity of solute in polymer
D_H	Hydraulic diameter

D_n	Number based mean diameter
D_p	Average size of the particles
D_{Pr}	Mean diameter of primary particles
D_v	Volume based mean diameter
F_D	Drag force
F_{ext}	External force exerted on magnetic particles
g	Gravitational acceleration
H	Magnetic moment of the particles
h	Microfluidic channel depth
I.D.	Internal diameter
K_0	Erosion rate constant
K_p	Partition coefficient
l	Channel length
n	Number of fluid division(in micromixer section 1.3.1.1)
O.D.	Outer diameter
P	Perimeter of the cross section
P_{atm}	Atmospheric pressure
P_{outlet}	Pressure of fluid at the channels outlet
Q	Fluid flow rate in channel
Q_{CP}	Continuous phase flow rate
Q_{DP}	Disperse phase flow rate
r	Distance of solute from the center of the sphere
R	Radius of the particles
R_{ch}	Resistance to flow
Re	Reynolds number
t	Time
T_g	Glass transition temperature
T_m	Melting point
v	Velocity of the particles

V_{cont}	Velocity of continuous phase
V_l	Volume of liquid
W	Channel width
W_c	Width of the continuous phase channel
W_d	Width of the dispersed phase channel
W_{DP}	Half width of the disperse phase channel
We	Weber number
W_{OR}	Width of the orifice
W_{UP}	Width of the continuous phase channel upstream of the orifice
α	Correlation between liquid and solid volume
ΔP	Pressure drop along channel
ΔZ	Distance between the orifice and disperse phase channel
$\Delta \rho$	Difference of the densities
η	Dynamic viscosity
ρ_{CP}	Continuous phase density
χ	Magnetic susceptibility
σ	Interfacial tension between two fluids

Acknowledgments

I would like to sincerely thank my supervisor Dr. Urs Hafeli for his support, mentorship and dedication to this research work. I appreciate him for his enthusiasm and his limitless effort in providing all the necessary facilities and resources and facilitating collaboration for completion of this work. I would also like to thank my supervisory committee, Dr. Brian Rodrigues, Dr. Helen Burt, Dr. Dana Grecov and Dr. David Maberley, for their valuable advice and guidance.

I am very thankful of Dr. Kathy Saatchi for her unconditional support and assistance. I am also thankful of Dr. Boris Stoeber who prepared the initial microfluidic chip design for me and assisted me in the modification of the chip design. I would also like to thank Dr. Alina Kupa for assisting me in microfluidic chip fabrication. I appreciate Dr. Silvio Dutz's collaboration in magnetic microsphere characterization and his advice on data analysis. I would like to thank Dr. Thomas Schneider for his constructive critics on my chip design and data analysis and his assistance in the simulation part of this thesis

I am grateful of Mrs. Lydia Cartar for her time and her technical advice in editing this thesis and my other written work in the past few years. I learned a lot from her. I thank all my previous and current colleagues in the Hafeli lab for their support and friendship.

I am forever grateful of my parents for their endless support and for their encouragement and love.

My very special thanks to my dear wife, Nazanin, for her endless support, love, patience and understanding.

This research was supported by a Collaborative Health Research Projects grant from the Natural Sciences and Engineering Research Council (NSERC) in Canada and the Canadian Institutes of Health Research (CIHR).

To my beloved,

Nazanin

Chapter 1: Background and Literature Review

1.1 Polymers in Pharmaceutical Sciences

Polymers are long-chain molecules made from tens to thousands of repeats of smaller molecules [1]. Polymers have extensive application in medicine and pharmaceutical sciences such as polymer sutures, prosthetic devices, and drug carriers for external and internal usage [2].

As a drug carrier, polymers can be used to design controlled drug delivery systems in order to increase local drug concentration, reduce the drug dosage interval and administration frequency, and reduce unwanted toxicological and immunological responses [3,4]. As drug carriers, drugs are chemically bonded, covalently or non-covalently, to the polymer or are physically protected by polymer materials [3,5,6]. In the design of the controlled drug delivery system, physical entrapment of the drugs in polymer materials is superior to chemical bonding since it allows for better control of the drug release rate [7]. Microencapsulation is one of the common physical entrapment methods used in the design of a controlled drug delivery system. In pharmaceutical sciences, microencapsulation can be defined as entrapment of a therapeutic agent in spherical particles with diameters between 1 to 1000 μm [6]. The resulting particles are known as microparticles.

Two approaches can be used for the entrapment of a therapeutic agent into the microparticles. In the first approach, the drug is surrounded by a layer of polymer material and a drug reservoir system is created, forming microcapsules (**Figure 1-1 a**). In the second approach, the drug is distributed uniformly or non-uniformly throughout the polymer matrix, forming microspheres (**Figure 1-1 b**)

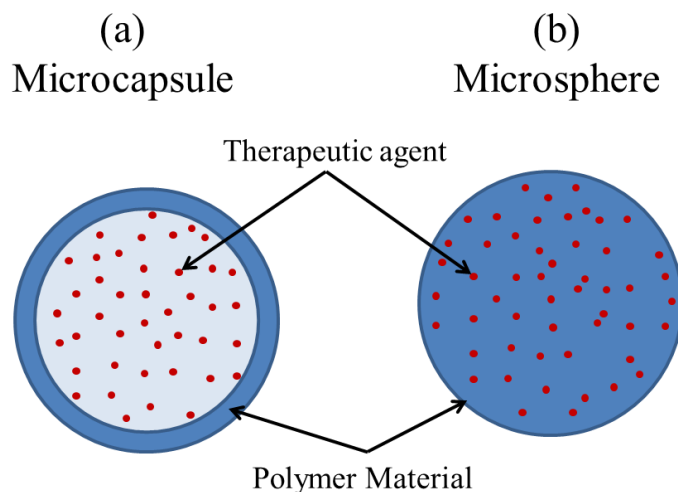
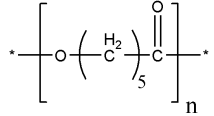
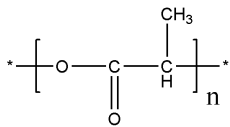
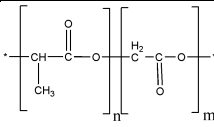
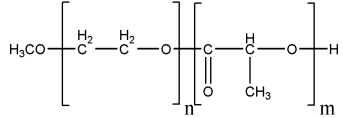
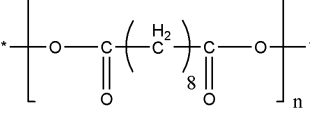
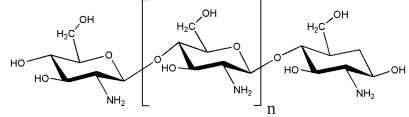
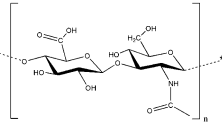
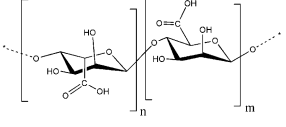
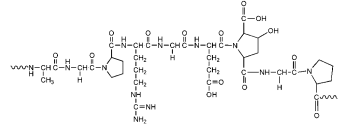


Figure 1-1. Schematic of polymer microcapsules and polymer microspheres structure

Both microcapsules and microspheres can be produced from many different kinds of polymer whose properties determine the route of application, rate of drug release and mechanism of particle production. For internal administration of microparticles, most important are biodegradability and biocompatibility of the polymer. A polymer is considered biodegradable when the polymer and its monomer in the body are non-toxic and can be cleared from the body without any side effects. A biocompatible polymer is a biodegradable or non-biodegradable polymer that does not show any negative physiological and immunological response after it is administered or implanted in the body [8]. While different biocompatible and biodegradable polymers have been synthesized or extracted from natural materials for biomedical applications (see **Table 1-1**), the focus of this thesis is on biodegradable polymers from the group of polyesters.

Table 1-1. Molecular structure of some biodegradable polymers typically used for the production of microparticles.

Polymer name	Polymer molecular structure
Poly (ϵ -caprolactone)	
Poly(lactic acid)	
Poly(lactic-co-glycolic acid)	
Poly(ethylene glycol)-b-poly(lactic acid)	
Poly(sebacic anhydride)	
Chitosan	
Hyaluronic acid	
Alginate	
Gelatine	

1.1.1 Biodegradable Polymers in Drug Delivery

Biodegradable polymers found their way into medicine in 1970, when for the first time, Herrmann et al. introduced and evaluated the usage of poly (glycolic acid) as suture materials [9]. Long term biocompatibility issues of non-degradable polymers and advancements in tissue engineering, regenerative medicine, gene therapy, and controlled drug delivery systems and technologies escalated the development of biodegradable polymers [10]. The major polymers in this group can be categorized as synthetic homopolymers, made of only one kind of monomer, synthetic copolymers, constituting at least two different types of monomers and natural polymers, extracted from natural materials. Samples from each group along with their chemical structure are shown in **Table 1-1**. Synthetic polymers are preferred in drug delivery since their properties can be adjusted for the application and they are less immunogenic [10].

Based on the degradation routes, these polymers can be divided into hydrolytically degradable polymers or enzymatically degradable polymers. Hydrolytically degradable polymers have a susceptible bond in their structures that can easily be broken down by a water molecule. The enzymatically degradable polymers are more stable in aqueous media and, as their names implies, are degraded by an enzyme. In spite of the higher stability of the enzymatically degradable polymers, the hydrolytically degradable polymers are more desirable as their degradation kinetics do not change in different body organs/tissues and are constant even among patients [10].

Different groups of hydrolytically degradable polymers have been synthesized such as polyesters, poly(ortho)esters, polyphosphazenes, polyanhydrides, polyphosphoesters, polyurethanes and poly(ester amides).

Among all, poly(α -ester) such as poly(lactic acid) (PLA), poly(lactic-co-glycolic acid)(PLGA) and poly (ϵ -caprolactone) (PCL) have received most attention since they are approved by the United States Food and Drug Administration (FDA) and most other countries regulatory bodies for pharmaceutical and medical applications and have good mechanical properties [11].

1.1.1.1 Poly (Lactic Acid)

Poly(lactic acid) is an FDA approved biodegradable aliphatic polyester. It is degraded through hydrolysis into lactic acid and then eliminated from the body through the Krebs cycle. Poly(lactic acid) is synthesized either by direct polymer condensation of lactic acid or by ring opening polymerization of lactide (lactic acid cyclic dimer). The ring opening method is preferable because the molecular weight of the polymer in this method is better controlled [12]

(Figure 1-2).

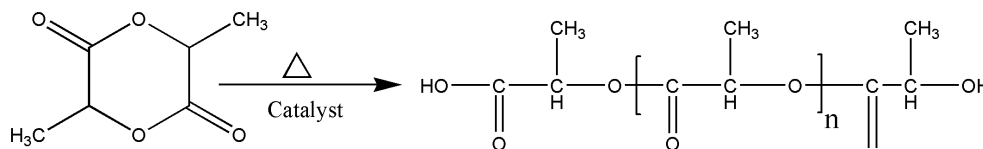


Figure 1-2. Lactic acid cyclic dimer ring opening polymerization.

Lactic acid has a chiral centre, and it has two enantiomers known as D-lactic acid and L-lactic acid. Therefore, the lactide can exist as L-lactide, D-lactide and meso-lactide (Figure 1-3). During ring opening polymerization, the fraction of L-lactic acid and D-lactic acid determines the level of crystallinity of the synthesized polymer. Semicrystalline poly (L-lactic acid) (PLLA) is formed only when the weight fraction of L-lactic acid is greater than 93%, otherwise, it forms amorphous poly (D,L-lactic acid) (PDLA) [13].

Semicrystalline poly (L-lactic acid) has a melting temperature between 130 – 180 °C and a glass transition temperature of 50 - 80 °C, it also has better mechanical properties (e.g., elasticity and tensile strength). At equal molecular weight, PLLA degrades slower than PDLLA [12,13].

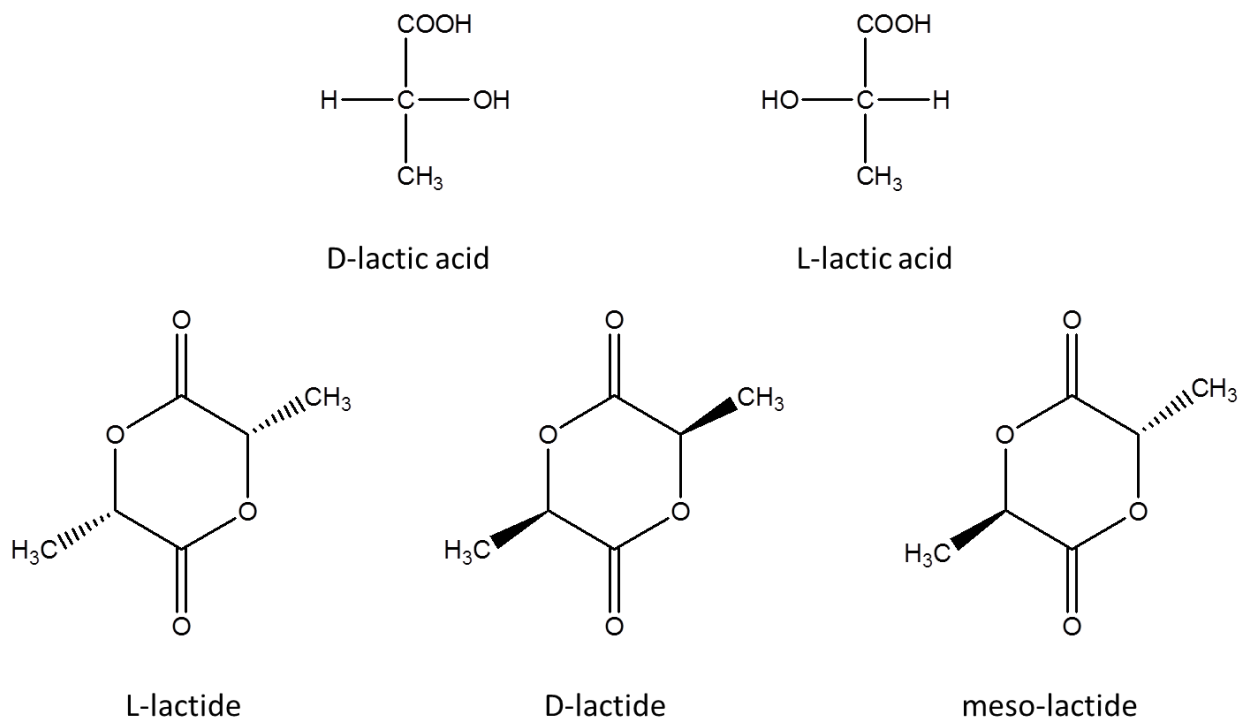


Figure 1-3. Molecular structure of lactic acid and lactide enantiomers.

1.1.1.2 Poly (Lactic-Co-Glycolic Acid)

Poly(lactic-co-glycolic acid) is another aliphatic biodegradable polyester approved by the FDA as drug carrier and for medical devices. It is a random copolymer of lactic acid and glycolic acid and is synthesized by random ring-opening copolymerization of the two monomers (**Figure 1-4**).

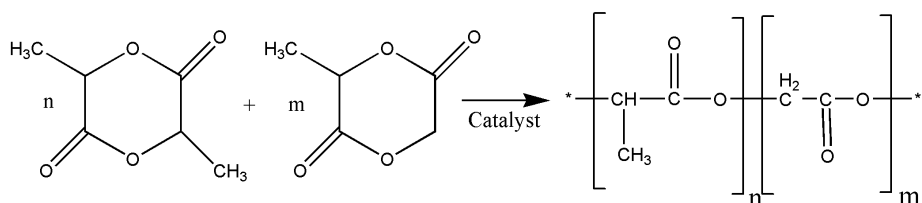


Figure 1-4. Poly(lactic-co-glycolic acid) synthesis by random ring-opening copolymerization.

PLGA is degraded by hydrolysis to glycolic acid and lactic acid and then eliminated in the body through the Krebs cycle.

1.1.1.3 Poly(ϵ -Caprolactone)

Poly(ϵ -caprolactone) is a biodegradable polymer which is produced by catalytic ring opening polymerization of ϵ -caprolactone (**Figure 1-5**).

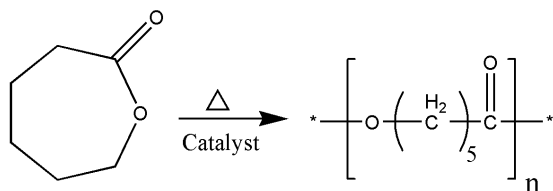


Figure 1-5. Synthesis of poly(ϵ -caprolactone) through ring opening polymerization.

The FDA has approved PCL as a drug delivery device and in surgical sutures. It has a low melting point (T_m) (60°C) and its glass transition temperature (T_g) is about -60°C . At ambient temperature, PCL is therefore in its plastic form and soft, which does not make it a good choice in pure form for microsphere preparation. However, it is added to other polymers to increase their mechanical properties (e.g., impact resistance) or is used in the synthesis of amphiphilic block copolymers where PCL forms the hydrophobic end of the polymer [12].

1.1.2 Mechanism of Microsphere Production from Poly(α -Ester) Polymers

Different manufacturing techniques have been reported for the production of poly(α -ester) polymer microspheres. In general, the polymer is dissolved in an organic solvent and polymer rich droplets of this phase are generated in an immiscible fluid. After solvent removal from the droplets, the polymer forms dried microspheres. The choice of the method depends on the polymer used, scalability of the method, size distribution of the particles required and kind of drugs used for encapsulation in the polymer microspheres. The three most common methods used for the preparation of poly (α -ester) polymer microspheres are briefly explained here.

1.1.2.1 Phase Separation (Coacervation)

The coacervation method is based on the difference in the solubility of a polymer in two different organic solvents. Initially the polymer is dissolved in a miscible solvent, and then a second solvent which is miscible with the initial solvent but cannot dissolve the polymer is gradually added to the solution while it is stirred. The second organic phase gradually mixes with the initial solvent and reduces the solubility of the polymer. At some point, phase separation occurs and polymer rich droplets form. For hardening purpose, the whole mixture is transferred to another container that consists of a large volume of an organic nonsolvent, miscible with the two organic solvents. At the end, the microspheres are collected and washed (**Figure 1-6**) [11,14].

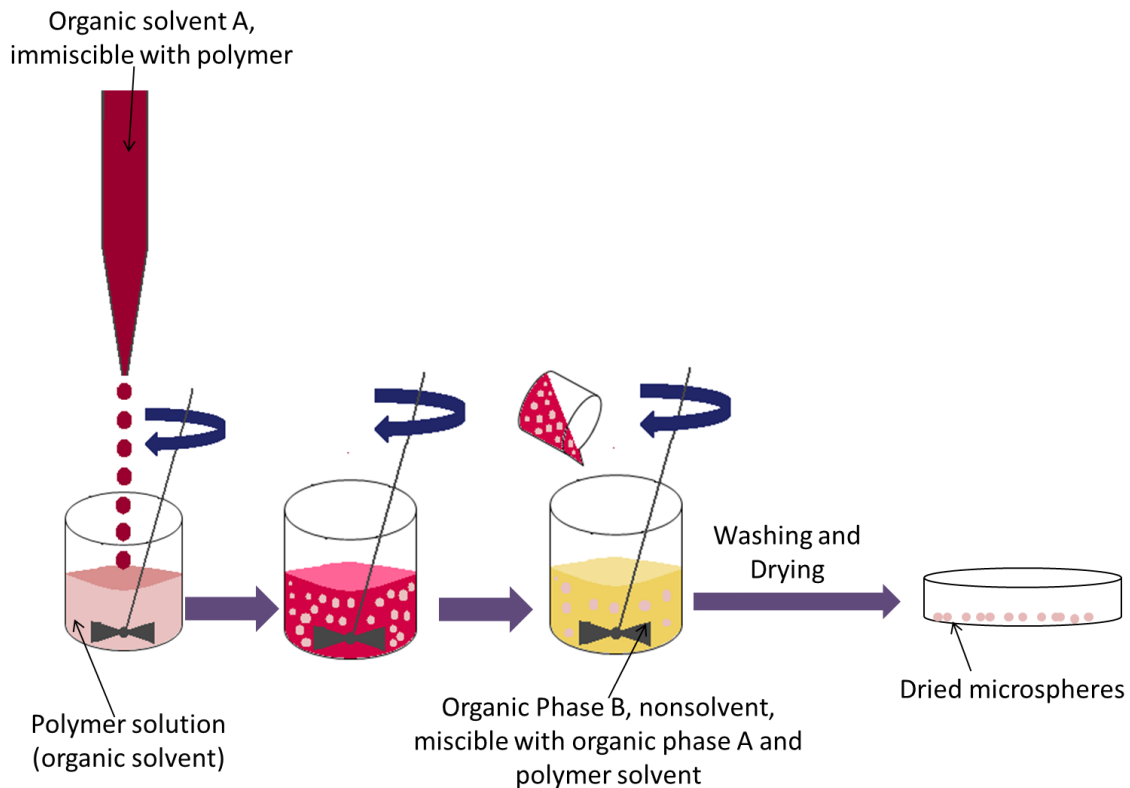


Figure 1-6. Schematic diagram for the production of polymer microspheres by the phase separation method.

This method was initially introduced by Bungenberg de Jong and Kruyt in 1929 [15]. Since then, effects of different parameters on the microspheres size and morphology of the microspheres have been investigated. It is a complicated method and size, size distribution and morphology of the formed microspheres depend on the several process variables such as stirring rate, rate of addition of the second organic solvent, concentration of polymer and viscosity of the organic solvents [14,16,17].

1.1.2.2 Spray Drying

Spray drying is a fast and inexpensive method for the production of polymer microspheres and one of the oldest methods developed for the powder production and encapsulation of drugs into polymer microspheres. It is based on the co-flowing of polymer solution and compressed air or nitrogen through a small nozzle to break the liquid stream into small droplets. The liquid is sprayed into a high temperature chamber to facilitate solvent evaporation from the droplets. Dried particles are collected at the bottom of the chamber (**Figure 1-7**).

Formation of the particles and their shape, size and size distribution depend on the solvent used for polymer dissolution, temperature of the solvent evaporation, the flow rate of the fluids, nozzle geometry and viscosity of the solution [18].

Spray drying usually leads to the formation of particles with broad size distribution. Additionally, due to the low shear force in the system, formation of fibres are very common even from very low polymer concentration solutions [11,18,19]. Moreover, the high temperature used for drying particles may affect the labile encapsulated drugs and may affect the polymer structure and the particles' shape when dried above the polymer glass transition temperature [18].

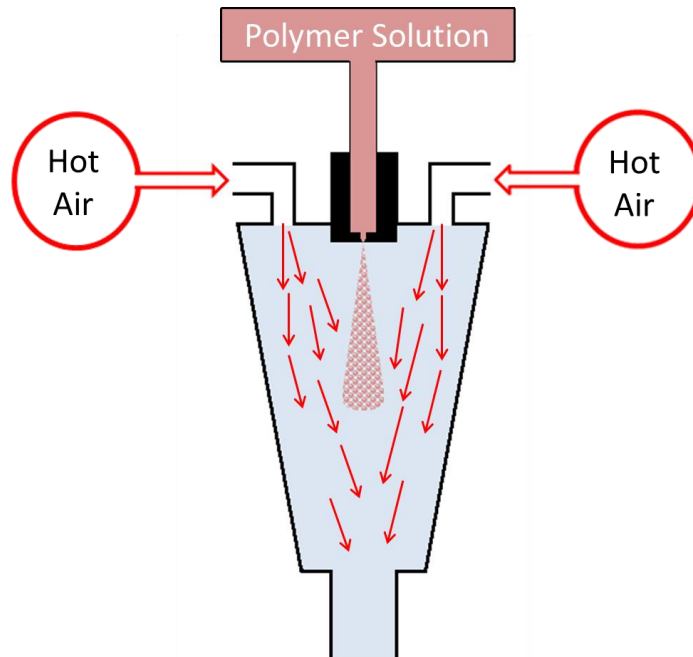


Figure 1-7. Schematic diagram of a spray drying system used for the production of dry powders / microspheres.

1.1.2.3 Emulsification and Solvent Extraction / Evaporation

Emulsification is the most common method used to produce polyester based polymeric microspheres. In this method, the polymer is dissolved in an organic solvent, the oil phase, and mixed with an aqueous base solution, the water phase, to generate an oil-in-water emulsion. The polymer rich droplets are then formed by applying shear stress to the system. From each droplet, a microsphere is obtained through the process of solvent evaporation or solvent extraction (Figure 1-8).

Efficacy and feasibility of the drug encapsulation by the emulsification-solvent evaporation method depends on the hydrophilicity and hydrophobicity of the drug. Water insoluble drugs can be encapsulated by single oil-in-water emulsion. The oil phase is mixed with the drug which stays inside the polymer-containing droplet when added to the water phase. An extra step is required for the encapsulation of hydrophilic drugs. The drug solution is first mixed with the

polymer phase to generate a water-in-oil emulsion. This initial emulsion is added to a second aqueous phase to form a water-in-oil-in-water emulsion where the drug is entrapped inside the polymer-containing droplets generated after applying shear stress to the system.

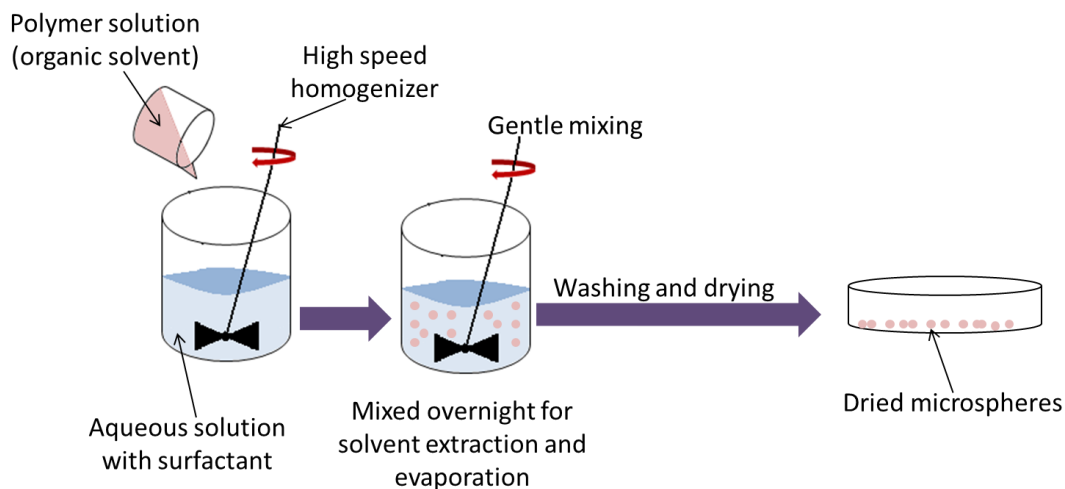


Figure 1-8. Polymer microsphere production steps in emulsification and solvent extraction / evaporation method.

The size of the formed droplets and their polydispersity in this system is proportional to the magnitude of the force applied to each droplet, the total time that the force is applied to the system, physicochemical properties of the fluids used (concentration, viscosity, interfacial tension, etc.) and the volume of the fluids used. The effects of each parameter have been described by Li *et al.* in their thorough review paper [8]. Controlling the size of the particles is difficult and requires optimization of all of the parameters, yet microspheres still show a relatively broad size distribution due to the variability of shear stress in different locations of the vessel. For example, the shear stress is high near the propeller and declines towards the vessel wall. Therefore, controlling the shear stress around the interface of the two immiscible liquids might be one method of forming monodispersed droplets. Towards this aim, several emulsification methods have been developed such as membrane emulsification, ink-jet printing

and microfluidic systems for specific application, and all of them have their unique advantages and limitations [20]. We focused in this thesis on microfluidic systems for the production of monosized magnetic and non-magnetic polymer microspheres. The mechanism of droplet generation in microfluidic systems is discussed in section 1.2.

1.1.3 Importance of Monodispersity

The production of monosized microspheres is crucial in the design of controlled and targeted drug delivery systems. The rate of the drug release from the microspheres, the movement of the particles in the blood stream, and the controlled and guided movement of the particles by an external force, i.e., magnetic force, all depend on the particle size.

Drug release from microspheres takes place by diffusion of the drug, the microsphere disintegration or a combination of both. For spherical particles, when drug release from particles is only controlled by diffusion, Fick's law of diffusion (**Eq. 1-1**) can be applied to calculate the rate of drug release:

$$\frac{\partial C_s}{\partial t} = \frac{1}{r^2} \left[\frac{\partial}{\partial r} \left(D_e r^2 \frac{\partial C_s}{\partial r} \right) + \frac{1}{\sin \theta} \frac{\partial}{\partial \theta} \left(D_e \sin \theta \frac{\partial C_s}{\partial \theta} \right) + \frac{D_e}{\sin^2 \theta} \frac{\partial^2 C_s}{\partial \phi^2} \right] \quad 1-1$$

where: C_s = solute concentration in solid phase, r = distance from the centre of sphere, D_e = diffusivity of solute in polymer, and t = time.

Crank has solved this equation for spherical particles immersed into a finite liquid volume with three assumptions: (i) diffusion is only radial, (ii) no mass transfer resistance exists in the liquid phase, and (iii) the diffusion coefficient is constant [21,22]. The solution (**Eq. 1-2**) shows the exponential relationship between drug release rate and particle radius.

$$\frac{M_l^t}{M_l^\infty} = 1 - \sum_{n=1}^{\infty} \frac{6\alpha(1+\alpha)}{9+9\alpha+\alpha^2 q_n^2} \exp \left[\frac{-D_e q_n^2 t}{R^2} \right] \quad 1-2$$

where M_l^t and M_l^∞ are mass of the drug released from the particle at time t and at equilibrium, respectively. R is the radius of the particle, α is a correlation between liquid and solid volume and partition coefficient **Eq.1-3**) and q_n is a mathematical term defined in **equation 1-4**

$$\alpha = \frac{V_l}{4\pi R^3 K_p} \quad 1-3$$

where V_l is Volume of liquid in diffusion vessel, K_p is the partition coefficient and R is the radius of the particle.

$$3 \tan(q_n) + \alpha q_n^2 \tan(q_n) - 3q_n = 0 \quad 1-4$$

Drug release from the particles can be due to microsphere disintegration. The rate of drug release from spherical particles has also been modeled when surface erosion controls solute release (**Eq. 1-5**) [23].

$$\frac{M_l^t}{M_l^\infty} = 1 - \left[1 - \frac{k_0 t}{C_0 a_0} \right]^3 \quad 1-5$$

where k_0 is erosion rate constant, C_0 is initial concentration of solute in the microsphere, a_0 is initial radius of the sphere and t is time.

Both **equations 1-2** and **1-5** show that drug release has a high dependency on the size of the particles under both release rate mechanisms. Having a narrower size distribution can therefore help to predict drug release profiles more accurately.

In addition, movement of the particles in the blood stream is a size dependent parameter. In the case of magnetic drug targeting, the magnetic force applied to a particle is proportional to the cube of its radius according to **equation 1-6** [24,25].

$$F_{ext} = \chi \frac{4}{3} \pi R^3 H \frac{dB_0}{dx} \quad 1-6$$

where F_{ext} is the force exerted on the particles, χ is the particle magnetic susceptibility, R is the radius of the particle, H is the magnetic moment on the particle, and B_0 is the magnetic field.

Meanwhile, when particles are moving in a fluid drag force acts on particles from fluid which has a linear correlation with particle size at low Re number (**Eq. 1-7**) [24,25].

$$F_D = 6\pi\eta Rv \quad 1-7$$

where F_D is Drag force, η is dynamic viscosity, R is radius of the particle and v is velocity of the particles relative to the fluid.

In summary, monosized particles are desirable to gain control over the required force to reliably manipulate microspheres and to predict a system's drug release rate, something that is not possible in a polydispersed system.

1.2 Microfluidics

Microfluidics can be defined as systems and techniques that were developed to control fluids in channels with at least one dimension smaller than 1 mm [20,26,27]. Droplet based microfluidic systems were for the first time introduced by Kawakatsu *et al.* which in 1997 pioneered the controlled formation of micrometer-sized emulsions [28,29].

1.2.1 Dimensionless Numbers in Microfluidics

The small dimensions of the microfluidic channels result in a low Reynolds number ($Re < 2300$) and the formation of a laminar fluid stream inside the channels, leading to better control over the local fluid elements. As a result, droplets can be generated with better size control [30,31].

Due to the small scale of the channels, surface effects play a crucial role in the manipulation of fluids and generation of droplets. The droplet based microfluidics requires at least two immiscible fluids that come into contact with each other at a junction and form an interface. Droplets are pinched off from this stream due to interfacial instability created along the interface [32]. The interfacial instability in this system is determined by the geometry of the junction, physicochemical properties of the fluids (density and viscosity), interfacial tension between the fluids, and the flow rate of the fluids [30-32]. The size of the generated droplets is defined by interaction between deforming fluid stresses on the interface and resistance capillary pressure [31]. The correlation between these factors is described by three different dimensionless numbers.

The most important number is the capillary number (Ca) that defines the correlation between viscous stress and interfacial stress along the interface between two fluids which can be two immiscible liquids or a gas and a liquid (**Eq. 1-8**).

$$Ca = \frac{\mu_i v_i}{\sigma} \quad 1-8$$

where μ_i is the viscosity of continuous phase, v_i is its average velocity and σ is the interfacial tension between two fluids. The capillary number in microfluidic systems ranges between 10^{-3} to 10. Higher Ca values show dominant effects of viscous force. At these higher Ca values, large irregularly shaped droplets are generated. With decreasing Ca numbers, the interfacial stresses suppress the effect of the viscous stress, and the droplets become smaller and spherical [31,32].

The ratio between the inertia force and interfacial stress is defined by Weber number (We) (**Eq.1-9**). Due to the small fluid velocities, the Weber number effect in liquid-liquid system is minimal and can be ignored. The Weber number is given by

$$We = \frac{\rho_i v_i^2 a}{\sigma} \quad 1-9$$

where ρ is the density of the fluid and ‘a’ is defined as characteristic length.

To determine the importance of inertial force to viscous stresses, the Reynolds number (Re, **Eq.1-10**) is calculated. The value of the Reynolds number determines the flow regime in the channels. In fluid mechanics, a flow with a Reynolds number below 2300 is considered laminar, above which the fluid flow can be turbulent. The Reynolds number in a microfluidic systems is usually below 1 [31].

$$Re = \frac{\rho_i v_i D_H}{\mu_i} \quad 1-10$$

D_H is hydraulic diameter of channels and calculated according to the equation (**Eq.1-11**),

$$D_H = \frac{4A}{P} \quad 1-11$$

while A is the cross sectional area of the channel and P is perimeter of this cross section that is wet.

The Bond number (Bo, **Eq. 1-12**) is a dimensionless number that compares the importance of gravitational force to interfacial tension. In our system due to the horizontal movement of the fluids, effect of the Bo number is not significant

$$Bo = \frac{\Delta\rho g a^2}{\sigma} \quad 1-12$$

where $\Delta\rho$ is the difference in density of the two immiscible fluids.

To control the stresses on the interface and droplet breakup in microfluidic systems different geometries have been developed. They are categorized in three different groups: (i) T-junctions, (ii) co-flowing and (iii) flow focusing devices and will be discussed next.

1.2.2 Droplet Generation in Microfluidic Devices

1.2.2.1 T-Junction

Droplet generation in a T-junction microfluidic system was first introduced by Thorsen *et al.* in 2001 [33]. In this system, two immiscible fluids come into contact with each other perpendicularly and droplets are formed due to the stresses created at the fluids interface (**Figure 1-9**). The size of the formed droplets depends on the ratio of the channels width (w_d/w_c ; w_d is the width of the dispersed phase (DP) channel and w_c is the width of the continuous phase (CP) channel) and the capillary number [31,32].

The mechanism of droplet generation in the T-junction systems can be divided into three different groups:

- (i) At very low continuous phase capillary number ($Ca < 0.002$) and when the width of the continuous phase channel is very close to the width of the dispersed phase channel, the dispersed phase will block the continuous phase path that causes an increase in the upstream pressure in CP. As a result of high pressure, the dispersed phase is squeezed and at a certain point, the DP stream breaks into droplets (squeezing regime, **Figure 1-9 a**) [20,31,32]. Due to the low capillary number, the flow rate of the continuous phase does not affect droplet formation as long as its flow rate is higher than the flow rate of the dispersed phase. In this regime, the size of the droplets formed is mainly controlled by the viscosity ratio of the fluids rather than their flow rate ratio [31,32]. When the DP flow rates become larger than the CP flow rates, no droplet is formed and the DP and CP flow in parallel in the downstream channels [31,32].

(ii) When the width of the continuous phase channel is at least 5 times bigger than the width of the dispersed phase channel and the capillary number is further increased ($0.01 < Ca < 0.3$), the DP cannot block the CP channel and the droplets are formed only when the shear stress on the interface exceeds the viscose force (dripping regime, **Figure 1-9 b**). The size of the droplets depends on the CP flow rate and it decreases as the continuous phase flow rate increases [20,31].

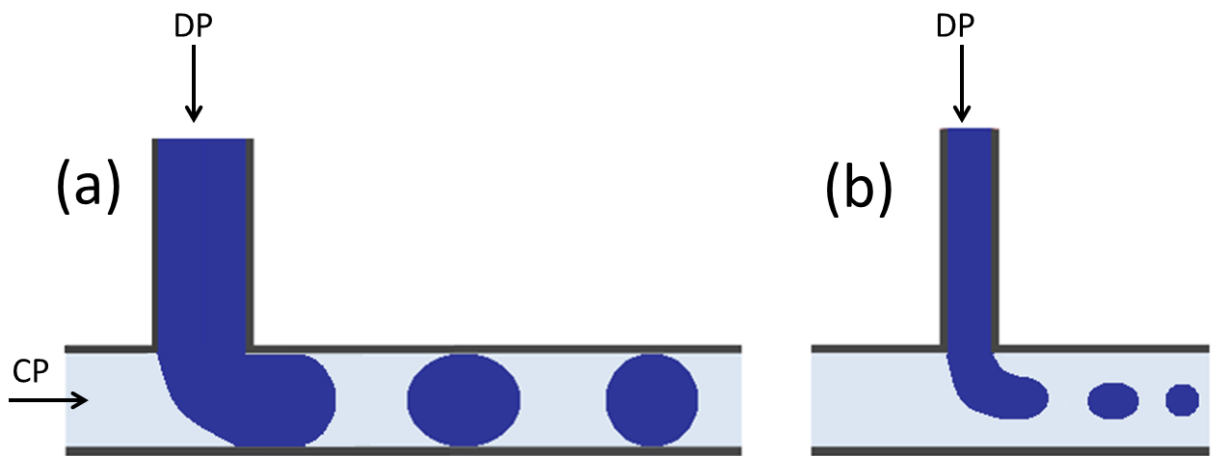


Figure 1-9. Schematic diagram of droplet generation in T-junction microfluidic system. a) Squeezing regime, b) dripping regime.

(iii) If the capillary number becomes too high, the dispersed phase is stretched and the droplets form in the continuous phase channel under an unstable jetting regime [20].

Although the droplets generated in the T-junction systems are polydisperse, it is a desirable system for droplet generation when particle monodispersity is not of essence [30] due to its easy fabrication and simple operation.

1.2.2.2 Co-Flowing

Co-flowing is the simplest designed system for the generation of droplets in microfluidic systems. In co-flowing, two concentric tubes are aligned precisely and the dispersed phase is injected through the inner tube and exits at the other end into a fully developed parallel

continuous phase. [31,32,34,35]. The droplets are pinched off from the dispersed phase stream either near the tip of the inner capillary tube (dripping regime) at low flow rates due to the imbalance between the viscous drag force and interfacial tension [35] or from an extended dispersed phase downstream of the channels (jetting regime) at high flow rates due to the Rayleigh-Plateau instability (**Figure 1-10**) [34].

At low flow rates, when the $Ca < 1$, the interfacial stress dominates the viscous shear stress, therefore, the droplets form under the dripping regime (**Figure 1-10 a**). By increasing the flow rates the mechanism of droplet formation changes. Utada et al. studied the mechanism of transition from dripping to jetting regime in co-flowing system and they could identify two different kinds of transition mechanisms [34].

The first kind of transition from dripping to jetting regime happens, when at constant dispersed phase flow rate, the velocity of the continuous phase (v_{cont}) increases. By increasing the v_{cont} , drag forces exerts from the continuous phase to the interface increases. It initially causes a reduction in the size of the droplets that form under the dripping regime. Eventually, when the v_{cont} reaches its critical value, at $Ca > 1$ and when the size of the formed droplet is equal to the diameter of the inner tube [34], the dispersed phase flow is suddenly stretched into the channel and forms a thin thread. Droplets form from the tip of this thread due to the Rayleigh-Plateau instability (**Figure 1-10 b**) [31,34,35]. The droplet size formed under this jetting condition is slightly bigger than the inner tube diameter.

The second kind of transition from dripping to jetting regime occurs when the dispersed phase flow rate is increased and it passes the continuous phase flow rate. Jet formation in this class is significantly different. By increasing the dispersed phase flow rate, the size of the droplets increases and the droplet detachment point moves downstream. A thread is formed between the

capillary tip and the droplet pinch off point. The diameter of the thread increases as it is stretched into the channel. Yet, the droplets are formed under dripping conditions and the $We < 1$ (**Figure 1-10 c**). Therefore, after separation of each droplet since the inertial force of the inner phase is smaller than interfacial tension, the thread is retracted back to the tip of the capillary and the process repeats again [34]. By further increasing the dispersed phase flow rate, the inertial forces of the dispersed phase eventually become large enough to overcome interfacial tension ($We > 1$). It forms a jet by pushing the droplet growth and breakup point further away from the tip of the capillary. After droplet separation, the thread is only pulled back slightly.

Overall, the behavior of the disperse phase and continuous phase in co-flowing system can be predicted by determining the We of the inner phase, Ca of the outer phase, Re for both phases and the ratio of velocity of dispersed phase to continuous phase [34].

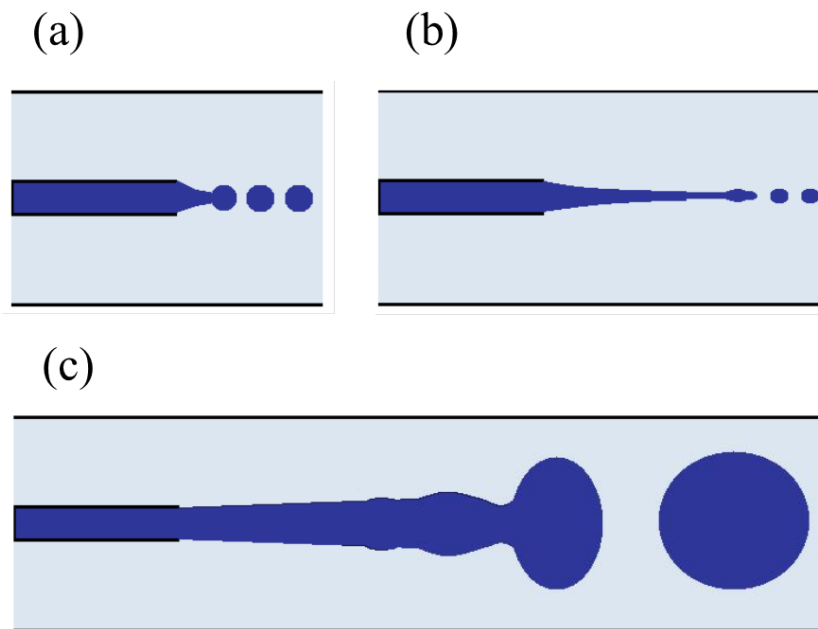


Figure 1-10. Schematic image of droplet generation in co-flowing system. (a) Dripping regime when $Ca < 1$, (b) Jetting regime at high $Ca > 1$, (c) widening jet when flow rate of dispersed phase is bigger than flow rate of continuous phase. Redrawn from [34].

1.2.2.3 Flow Focusing

Anna *et al.* introduced an alternative method for droplet generation in a liquid-liquid microfluidic system [20,30,32,36]. In this new design, two immiscible fluids are forced coaxially through an orifice and droplets are formed either at the orifice or in the downstream channels depending on the geometry of the system, properties of the fluids and their flow rates (**Figure 1-12**). The droplet generation in the flow focusing system has four distinct mechanisms: Squeezing or geometry controlled regime, dripping regime, jetting regime and tip-streaming [20,31,32,37-39]. Each mechanism is characterized by the capillary number and location of the dispersed phase relative to the orifice. For Flow focusing systems, more complicated capillary number has been defined by Anna and Mayer that incorporate the dimensions of the channels upstream of the orifice (**Eq. 1-13**)

$$Ca = \frac{\mu_{CP} W_{DP} Q_{CP}}{2\sigma h \Delta Z} \left[\frac{1}{W_{OR}} - \frac{1}{2W_{UP}} \right] \quad 1-13$$

where, μ_{CP} is viscosity of the CP, Q_{CP} is the CP flow rate, σ is the interfacial tension between CP and DP, ρ_{CP} is the CP density, h is the depth of the channels, W_{OR} is the width of the orifice, W_{UP} is the width of the CP channels upstream of the orifice, ΔZ is the distance between the orifice and DP channel, and ' W_{DP} ' is the half-width of the DP channel at the intersection with the CP channel (**Figure 1-11**).

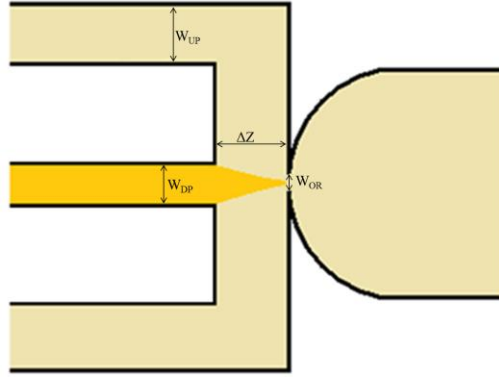


Figure 1-11. Schematic of a microfluidic flow focusing system. Parameters marked on the image are the ones used in equations 1-13 and 3-1.

1.2.2.3.1 Squeezing or Geometry Controlled Regime

At very low capillary numbers, the dispersed phase fills the orifice and creates a narrow space for the continuous phase to pass through the orifice. It causes an increase in the dynamic pressure in the continuous phase upstream of the orifice. This high pressure squeezes the dispersed phase and eventually pinches off a droplet (**Figure 1-12 a**). The dispersed phase then retracts and the process repeats itself [20,38,40]. The size of the droplets generated is almost equal to the size of the orifice or slightly bigger with a very narrow size distribution ($CV < 2\%$) [38].

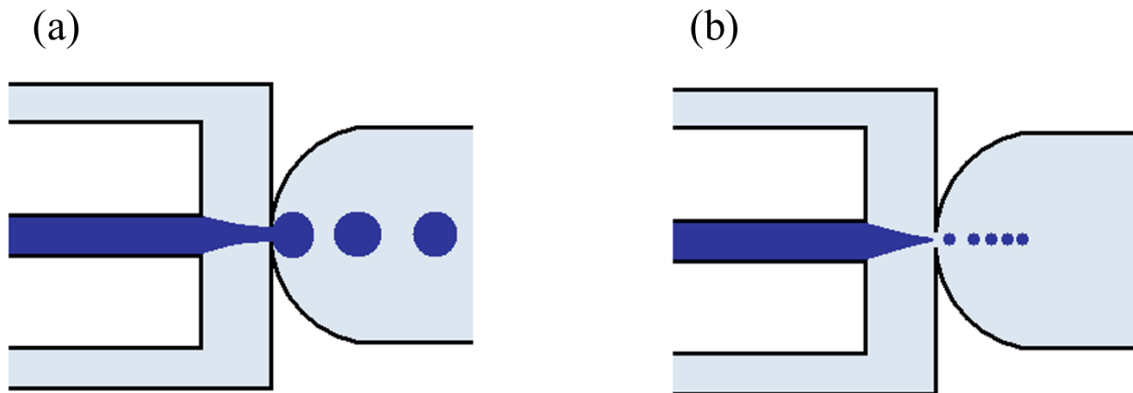


Figure 1-12. Schematic image of droplet generation in flow focusing system under (a) geometry-controlled regime and (b) dripping regime. Redrawn from Anna and Mayer (2006).

1.2.2.3.2 Dripping Regime

By increasing the capillary number, the viscous stress of the continuous phase increases and causes the dispersed phase to be squeezed and to form a short thread with a diameter smaller than the orifice width [20,38]. The thread extends into the orifice and the droplets pinch off from the thread (**Figure 1-12 b**) when the viscous stress is high enough to overcome the interfacial tension between the fluids [37]. In contrary to the geometry-controlled regime, the dispersed phase does not retract after droplet separation. The size of the formed droplets in this regime is smaller than the orifice size with a narrow size distribution [20,31].

1.2.2.3.3 Jetting Regime

Further increasing the capillary number causes further extension of the dispersed phase into the downstream channel. The length of the formed thread is three or more times longer than the width of the orifice [31]. The jet breaks into droplets of a broad size distribution due to the Rayleigh-Plateau instability, with droplets that can be as big as the orifice size (**Figure 1-13 a**) [20,31,37,38].

1.2.2.3.4 Tip-Streaming Regime

The fourth mode of droplet generation in a microfluidic flow focusing system happens at capillary numbers between the dripping and geometry-controlled regime and when the continuous phase to dispersed phase flow rate is greater than 300 [20,31,38]. Under this condition, a very thin thread is formed that breaks into droplets that can be as small as 1/20 of the orifice size (**Figure 1-13 b**) [20]. Anna and Mayer (2006) first reported this mode of droplet generation that can be used for the generation of very small droplets. They also reported the importance of surfactant concentration and showed that the thin thread will not form when the ratio of surfactant concentration to critical micelle concentration (CMC) is smaller than 0.5 [38].

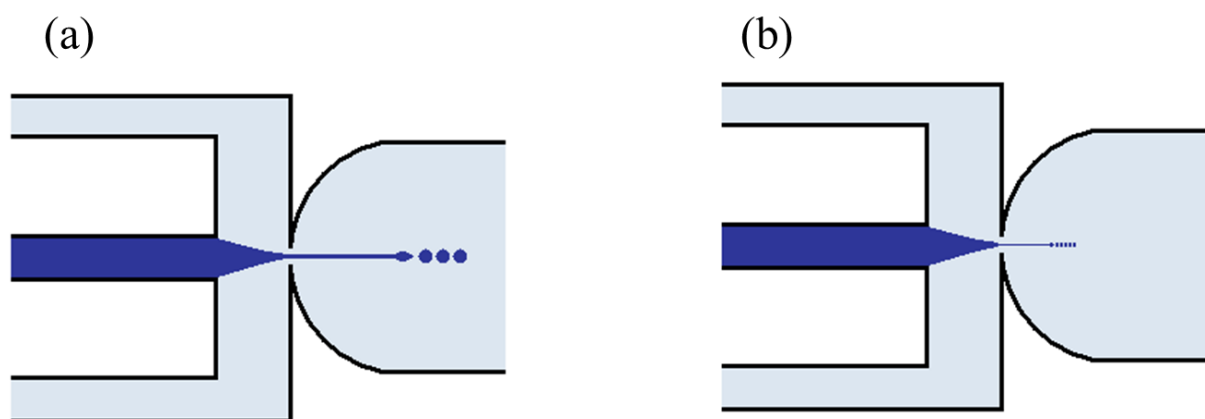


Figure 1-13. Schematic image of droplet generation under (a) jetting regime and (b) tip-streaming regime. Redrawn from Anna and Mayer [38].

Overall, the monodispersity of the droplets generated in a microfluidic flow focusing system is higher compared to T-junction and co-flowing systems. It is mostly used when the size distribution of the droplets is a crucial factor, although the device fabrication is more complicated [30].

1.3 Mixing in Microfluidic Systems

Homogenous mixing at microscale is a crucial factor for the performance of micro-system-analysis, lab-on-a chip devices, micro-reactions and drug encapsulation in polymer microspheres [41-43]. At macroscale, mixing is either done by the generation of turbulent fluid flow at high Reynolds numbers ($Re > 2300$) or by stirring and creating chaotic advection in the system [43]. The small dimensions of the microfluidic channels do not allow for the generation of turbulent flow. Chaotic advection and molecular diffusion are thus mechanisms of mixing in microfluidics [42,43]. Different microscale mixing devices have been designed that can broadly be categorized into active and passive micromixers. Active micromixers are powered by external energy to mix fluids with disturbance methods such as pressure, electrohydrodynamics, dielectrophoresis, electrokinetics, magneto hydrodynamics, acoustic pressure wave and heating [42,43]. Active

micromixers perform better than passive micromixers, but they are less desirable due to their complicated and challenging fabrication process [42-44].

Passive micromixers are simpler in design and do not use any external power. Our emphasis is on passive micromixers which are explained in detail in the following sub-sections.

1.3.1 Passive Micromixers

The goal of passive micromixers is to reduce the diffusion path or increase the contact time between fluids, in diffusion based micromixers, or to induce chaotic advection in the system by creating barriers or grooves in the channels, chaotic-based micromixers, to perform better mass transfer in the system [42,45,46]. Based on these requirements different types of micromixers have been designed.

1.3.1.1 Lamination Micromixers

Lamination is one of the simplest forms of passive micromixers. Two fluids come into contact with each other in microchannels and a contact surface is created between the two phases with short diffusion paths (**Figure 1-14**). The method relies solely on molecular diffusion, which makes the mixing rate depend on contact time and contact surface between the fluids [42].

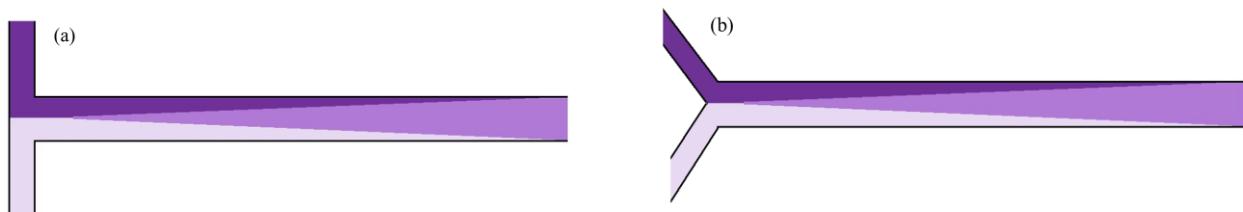


Figure 1-14. Schematic design of single lamination systems with (a) T-shaped and (b) Y-shaped inlets. Redrawn from [43].

Single lamination systems generally require a long channel for complete mixing [43]. The mixing time and channel length can be reduced, by using multi-lamination designs where each fluid stream is divided into two or more streams with narrower width in order to increase the

contact surface area and reduce the diffusion path [41,42,47]. For this purpose, two approaches have been proposed. The first approach is known as parallel lamination. In this technique, each stream is divided into several sub-streams and then they pass through narrow channels in parallel and at the end after complete mixing, the streams are combined [41,43,47,48]. In the second approach which is known as sequential lamination or split and recombination method, the fluids are constantly divided into two streams and then combined again.

A correlation between the diffusion time and the number of divisions was proposed by Erbacher *et al.* in 1999 [9,49]. They showed that diffusion time is reduced by the square of the division number (**Eq. 1-13**).

$$t = \frac{d^2}{2n^2D} \quad 1-14$$

where t is the diffusion time, d is the capillary diameter, D is diffusion coefficient and n is the number of fluid divisions. A significant reduction in mixing time is thus observed with multiple lamination steps, although the flow is laminar and the only mechanism of mixing is diffusion. To further improve the mixing quality, different designs were proposed that cause fluid mixing with chaotic advection.

1.3.1.2 Chaotic Advection

Advection is a method of mass transfer which takes place in the direction of the flow due to the bulk movement of fluid, while mixing in micromixers is a transversal mass transfer. To be able to use advection along with diffusion for mixing in micromixers, chaotic advection must be generated by special geometries or by external power [41-43].

Several designs have been proposed in the literature that generate chaotic advection and thus improve mixing performance significantly and reduce mixing length and time. The ability of each design in generation of chaotic advection in the micromixer depends on the Reynolds

numbers of the fluids. At high Reynolds number ($Re > 100$), simple twisting in the channels or zig-zag channel structure is enough to create chaotic advection in the system. As the Reynolds number decreases ($Re < 10$), simple changes in the direction of the fluids will not be enough for generation of chaotic advection in the system. Stroock *et al.* proposed a design in order to generate chaotic advection in systems with low Reynolds numbers ($Re < 100$) [50]. They showed that creating herringbone structures at the bottom of channels causes the axial pressure gradient in the system leads to the generation of a transverse flow in the system and consequently formation of chaotic flow in the micromixer (**Figure 1-15**).

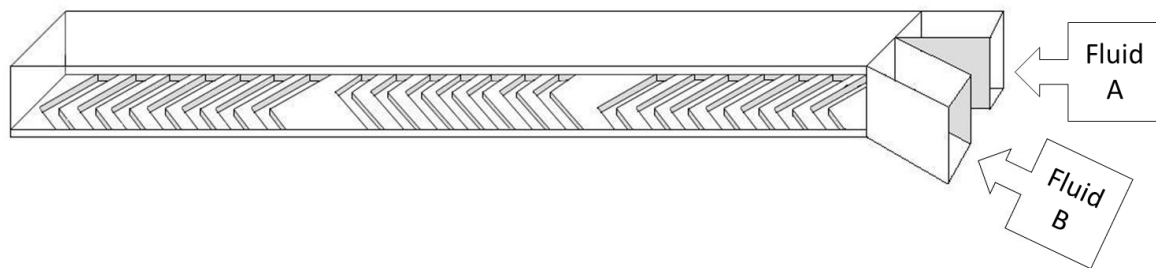


Figure 1-15. Schematic design of herringbone structure. Redrawn from [50].

The grooves at the bottom of the system cause constant rotation and extension of the local flow. Changing the orientation of the herringbone throughout the channel enhanced mixing even further [50]. The same phenomena were observed by Kim *et al.* who created slanted grooves at the bottom of the channels and built a periodic barrier at the top surface (**Figure 1-16**). They also showed that the mixing time in the chaotic micromixer is significantly lower (4 to 10 time) than in a T-shaped micromixer [51].

The aforementioned designs were initially proposed for the mixing of two miscible fluids and formation of a homogenous solution. Emulsion generation in micromixers from two immiscible fluids at low flow rate and low Reynolds number is much more challenging. The formation of an

emulsion requires a substantial amount of energy to overcome the interfacial tension between the two fluids.

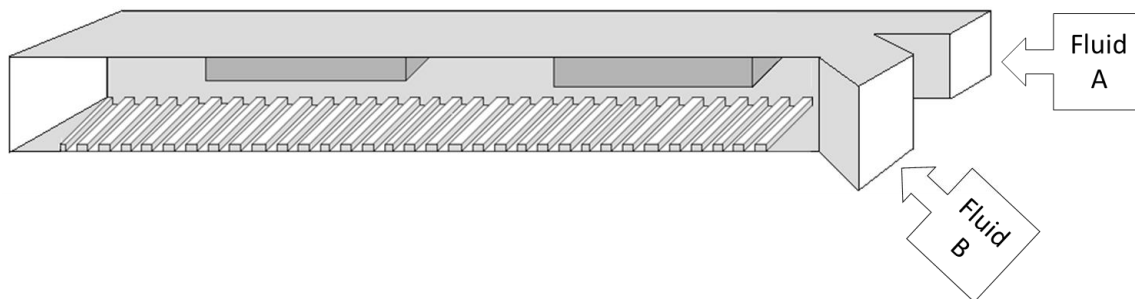


Figure 1-16. Schematic design of a micromixer with slanted groove at the bottom and barriers on the top. Redrawn from [51].

Mae *et al.* used the split and recombination design for the mass production of water in oil emulsion. They showed that stable emulsions could be produced when the combined flow rate of the two fluids was 1.2 L/h, although they saw no stable droplet generation at lower flow rates [52]. Further research is thus required to design a micromixer for the stable emulsion generation at low flow rates which is useful for handling low quantity of biological samples.

1.4 Research Hypothesis

Particle size distribution is a crucial parameter in engineering a reliable and efficient drug delivery system. Both the rate of drug release and particle behavior in the blood stream depend on the size of the particles and they are predictable in the systems with narrow size distribution. Different techniques have been developed for the production of microparticles with emulsification being the most common one. Emulsification in microfluidic systems is a technique developed more than two decades ago for the production of monosized microspheres which gives a better control over particle size, as compared to the standard methods such as solvent extraction. In addition, the microsphere production in microfluidic systems is a continuous process whereas conventional emulsification techniques are a batch process.

Therefore, batch to batch variation in particles size, loading efficiency and particles recovery can be eliminated when microfluidic systems are used for microsphere production.

Droplet generation in microfluidic systems and the production of polymer microspheres with these methods have been studied extensively in the last twenty years. Yet, to the best of our knowledge, production of hydrophilic and protein loaded polymer microsphere using microfluidic systems has not been addressed and it needs more investigation. The focus of this thesis is in the design of a microfluidic system for the production of drug loaded microspheres.

The thesis hypothesis is:

“Continuous encapsulation of proteins and magnetic nanoparticles in monosized polymer microspheres using microfluidic systems is possible by integrating different microfluidic units into one chip”.

To prove the hypothesis, three specific aims were defined:

1.4.1 Specific Aim 1 (Chapter 2 and 3):

“To design and optimize a microfluidic flow focusing system for the production of biodegradable polymer microspheres with narrow size distribution”

1.4.2 Specific Aim 2 (Chapter 4):

“To optimize the microfluidic system for the production of magnetic nanoparticle-loaded microspheres”

1.4.3 Specific Aim 3 (Chapter 5):

“To design and optimize a microfluidic system that integrates different microfluidic units in one chip for the production of albumin loaded microspheres, as a model for protein drug encapsulation”

Chapter 2: Production of Non-Magnetic Polymer Microspheres

To overcome the wide size distribution of bulk emulsification, the most common method for the production of polymeric microspheres, microfluidics systems have been developed that are able to produce monosized microspheres. From the many proposed designs for the microfluidic channels (see Chapter 1, Section 1.2), flow focusing is one of the most common designs (**Figure 2-1**). The mechanism of droplet generation in flow focusing systems has been studied extensively and factors affecting size and size distribution of the droplets have been well defined [38,53-58]. The applications considered in these cited studies were mainly the separation of biological materials like DNA and bacteria [56], encapsulation of mammalian cells in microfluidic cell culture [57], and the study of chemical reactions inside the droplets [58].

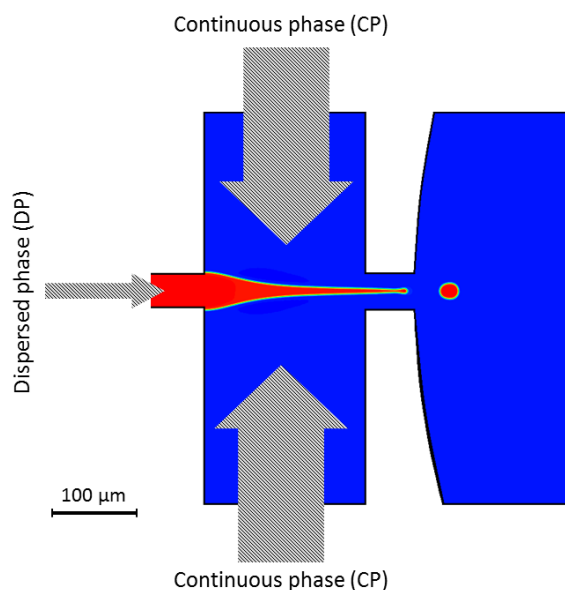


Figure 2-1 : Schematic diagram of droplet generation in a microfluidic flow focusing system. Blue color indicates continuous aqueous phase, red color the disperse polymer solution phase.

Another important application is drug delivery, where not only the formation of the droplet is important, but also its immediate aftermath in the microfluidic channel. During that time, solvent removal takes place. It must be ensured that the generated droplets remain intact and do not

break into smaller droplets or fuse with each other inside the chip, as that would increase polydispersity of the final microspheres. To overcome these issues, it helps to conduct the solvent-removal process partially in the chip. Therefore, additional parameters need to be taken into account that include the choice of the chip material (i.e., solvent resistant materials such as glass), operational conditions (i.e., flow rates, and concentration of fluids) and geometry of the channels (i.e., length of the downstream channels after the orifice) to ensure sufficient solvent extraction from the surface layer of the droplets.

In this chapter, I will present a microfluidic design that is capable of producing polymer microspheres with narrow size distributions. The choice of the materials for chip fabrication, effects of operational conditions on the size and size distribution of particles and the effect of copolymer on size and size distribution of the particles are also discussed. In the last section of the chapter, two clinical applications of produced monosized microspheres are described.

2.1 Material and Methods

2.1.1 Glass Chip Fabrication

The microfluidic flow focusing channel was microfabricated on a 100 mm diameter and 2 mm thick borofloat glass wafer with one reference flat and standard transparent finish 60/40 (Valley Design Corp., Shirley, MA, USA). The wafer was coated with 0.02 μm of chromium and 0.25 μm gold and then spin coated with positive photoresist (Shipley S1813; MicroChem Corp., Newton, MA, USA; **Figure 2-2a.1**). The pattern was transferred using a Canon PLA-501F mask aligner and developed with MF-319 photo developer (Rohm and Hass Electronic Material LLC, Marlborough, MA, USA; **Figure 2-2a.2**). After removing the photoresist (**Figure 2-2a.3**), channels were etched 45-50 μm deep using concentrated HF (49%; Avantor Performance

Materials, Central Valley, PA, USA; **Figure 2-2a.4**). Gold and chromium coatings were removed (**Figure 2-2a.5**) and the wafer was diced into 50×15 mm² chips.

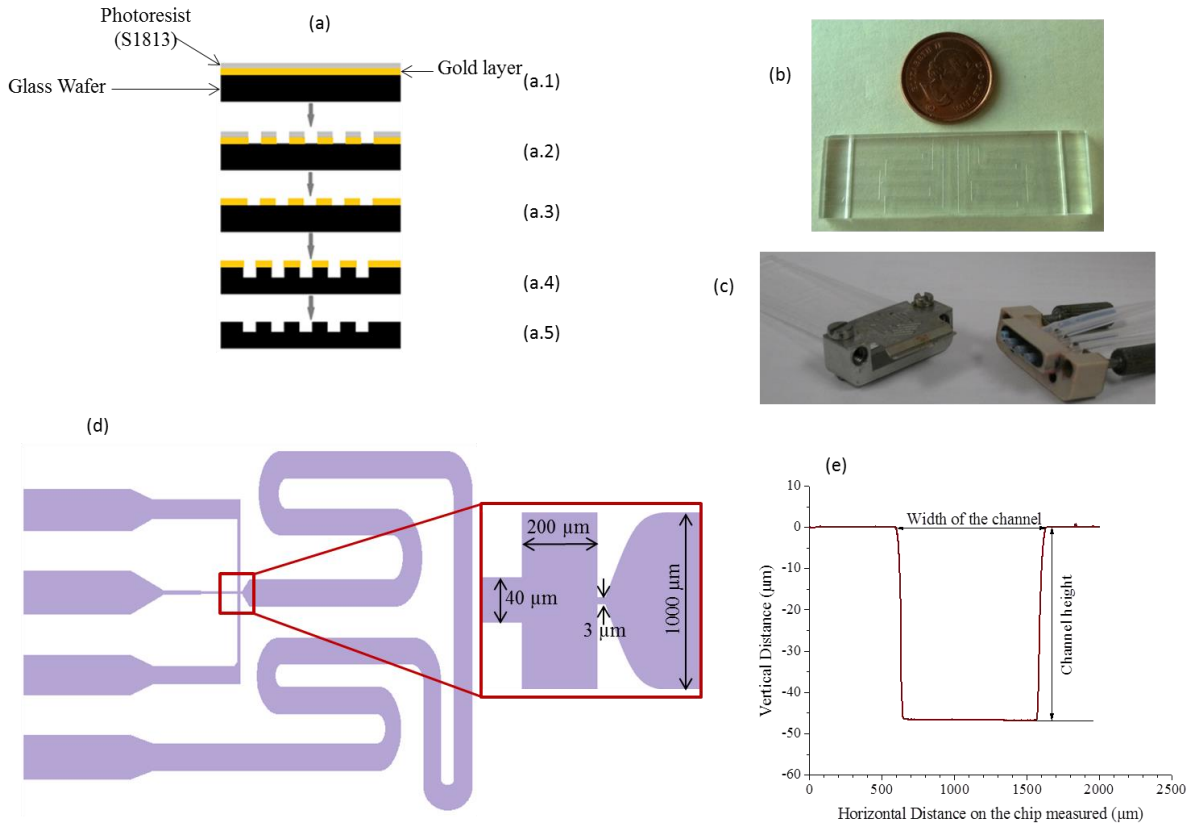


Figure 2-2: a) Fabrication process for the microfluidic flow focusing glass chip. Briefly, a 100 mm glass wafer was coated with chromium, gold, and a positive photoresist (a.1). After pattern transformation, coating was removed from the pattern area (a.2) and the photoresist was removed from the whole wafer (a.3). The glass was etched with highly concentrated HF (a.4) followed by removing all coated materials (a.5). The wafer was cut into 50×150 mm² slices and bonded onto another glass wafer of the same size to cover the channels. b) Fabricated glass chip after bonding. c) Glass chip and connectors used in all experiments. d) Schematic diagram of microfluidic design and channel dimensions on the mask before etching. e) Depth profile of the channels after etching.

Glass lids of the same size were cut from another wafer and thermally bonded to the microchips (6 h at 650 °C; **Figure 2-2b**). The chip features were measured by contact profilometry (DEKTAK 150 profilometer; Veeco, Plainview, NY, USA). The channels

dimensions mentioned in the **Figure 2-2 d** are dimensions on the mask. After etching, the width of the orifice at the narrowest point was 90 to 100 μm .

2.1.2 Polymeric Microsphere Production

The dispersed phase was prepared by dissolving poly(L-lactic acid; PLLA; Resomer L104, MW 2-3 kDa, Boehringer Ingelheim GmbH, Germany) in chloroform. The continuous phase consisted of 2% (w/v) poly(vinyl alcohol) (PVA; MW 13-23 kDa, 87-89% hydrolyzed, Sigma Aldrich) aqueous solution sterile filtered with a 0.22 μm filter. Both CP and DP were filled into glass syringes and loaded onto syringe pumps (Fusion 400 High Precision Dual syringe Pump and Nanojet XF pump, Chemyx Inc., Stafford, TX, USA) and connected to the microfluidic chip using fluorinated ethylene propylene (FEP) tubing with I.D. = 0.5 mm and O.D. = 1.6 mm (IDEX Health and Science, Oak Harbor, WA, USA), and a 4-hole connector (Mitos Edge Connector, Dolomite, Roystone, UK; **Figure 2-2c**). Droplets from the outlet were collected into a beaker filled with 2% PVA solution and the solvent extracted from the droplets into the PVA solution followed by complete solvent removal. The solvent was removed by injecting a low flow of air into the beaker and mixing the particles gently for at least 8 hours. Microspheres were then washed three times with distilled water to remove PVA from their surface. The particles were resuspended in distilled water and stored at 4 $^{\circ}\text{C}$ for further analysis or lyophilized if long-term storage was required.

2.1.3 Microsphere Size Distribution Analysis

The size analysis of the microspheres was done after completion of the solvent evaporation. The particles were resuspended in distilled water and an aliquot imaged under an inverted microscope (Motic AE31). ImagePro software was used to analyze the size of each microsphere. The size distribution of microspheres was determined using Origin 7 (OriginLab, Northampton,

MA, USA) using at least 200 particles for each analysis. The polydispersity of the particles was determined by calculating the coefficient of variation (CV) as

$$CV(\%) = \left(\frac{\sigma}{D_p} \right) \times 100 \quad 2-1$$

where D_p is the average diameter of the particles and σ is the standard deviation of the particle diameters. For CV calculations, both primary droplets and satellite droplets were included in all cases unless stated otherwise

2.1.4 Scanning Electron Microscopy

The surface morphology of polymer microspheres was examined by Scanning Electron Microscopy (SEM; Hitachi S-4700, Tokyo, Japan). A droplet of aqueous microsphere suspension was placed on an aluminum stub covered with carbon adhesive, air dried and subsequently coated with 5 nm of gold/palladium under reduced pressure (<5) using a JFC-1600 fine coater (JEOL, Tokyo, Japan). The samples were imaged at 2 keV.

2.2 Results and Discussion

2.2.1 Choice of Material for Chip Fabrication

The choice of the materials for microfluidic chip fabrication depends on different factors such as surface property of the channels, ease of fabrication, resistance to different solvents, transparency, and fabrication cost. For our purpose, the required properties for selection of material for microfluidic chip fabrication were i) surface hydrophilicity, ii) resistance to chloroform and iii) transparency of the chip to be able to see droplet generation under the microscope (**Table 2-1**). The first substrate considered for the fabrication of microfluidic channels was silicone since its structure and methods of shaping it are well known. However, silicone is not transparent enough for our purposes. Polymers are a second type of substrate that

is often chosen because of being the cheapest material. Furthermore, the fabrication processes are simple and channel surface properties can easily be modified. However, the available polymers are not chloroform resistant and were thus precluded. Glass is used when transparency and chemical and biochemical resistance of the channels are important [59]. Among the different glasses considered for the fabrication of microfluidic chip (**Table 2-1**), borofloat glass was found to be the most appropriate that fulfilled all the required criteria and was relatively inexpensive.

Table 2-1. Common wafer materials used for microfluidic system microfabrication and criteria considered for selecting a suitable material for our work.

Wafer Material	Hydrophilic Surface	Chloroform Resistance	Transparency	Price
Silicon	✓	✓	✗	Medium
Polydimethylsiloxane (PDMS)	✗	✗	✓	Low
Quartz	✓	✓	✓	High
Borofloat glass	✓	✓	✓	Medium

2.2.2 Production of Quasi-Monosized Polymer Microspheres

A microfluidic flow focusing system was designed (**Figure 2-2d**), fabricated out of borofloat glass, and optimized for the production of biodegradable PLLA microspheres at different flow rates. Particle size and size distribution of the microspheres depended on the flow rates of the fluids and their flow rate ratio (CP/DP) (**Table 2-2**). By increasing the flow rate ratio we found that the size of the particles decreased except at $Q_{cp} = 80 \mu\text{L}/\text{min}$ where the particle size increased. Further investigations are required to find the cause for this effect.

Under all operational conditions, a dual mode size distribution was observed (**Figure 2-4** to **Figure 2-7**). The second peak in the graphs describes the microspheres formed from the primary droplets and the first peak describes the microspheres formed from the satellite droplets generated after the primary droplets. A droplet is considered as satellite droplet when its volume

is smaller than 1% of the volume of the primary droplet [60]. The analysis of the size of the primary microspheres shows that the majority of the microspheres produced are quasi-monodispersed particles (**Table 2-2**), which means its coefficient of variation is less than 16%.

Table 2-2. Size and size distribution of PLLA microspheres produced at different flow rates. Size of the particles was determined after completer solvent removal in at least 200 microspheres per experiment.

<i>Continuous Phase</i>		<i>Dispersed Phase</i>		D_n [μm]	CV_n [%]	D_{pr} [μm]	CV_{pr} [%]
C_{CP} [% (w/v)]	Q_{CP} [$\mu\text{L}/\text{min}$]	C_{DP} [%(w/v)]	Q_{DP} [$\mu\text{L}/\text{min}$]				
1	10	2	0.50	23.13 ± 6.69	37.57	23.50 ± 8.35	35.53
1	50	2	0.50	16.30 ± 6.20	36.04	18.40 ± 3.40	18.48
1	100	2	0.50	14.45 ± 3.27	22.03	14.87 ± 2.47	16.61
1	150	2	0.50	11.54 ± 5.00	42.23	12.47 ± 4.54	36.41
2	30	10	0.25	26.90 ± 13.21	49.11	35.14 ± 5.26	31.94
2	30	10	0.60	34.70 ± 11.63	33.51	38.06 ± 6.24	16.40
2	40	10	0.25	31.01 ± 10.39	33.51	33.47 ± 6.84	20.44
2	40	10	0.60	35.04 ± 10.62	30.31	37.96 ± 5.18	13.65
2	40	10	1.00	39.62 ± 12.71	32.08	43.78 ± 4.61	10.53
2	60	10	0.25	26.48 ± 9.03	34.10	28.54 ± 6.69	22.39
2	60	10	0.60	28.85 ± 4.87	16.88	29.75 ± 1.66	5.58
2	60	10	1.00	28.59 ± 4.44	15.53	30.26 ± 2.21	7.30
2	80	10	0.25	26.38 ± 4.41	16.72	26.86 ± 2.99	11.13
2	80	10	0.60	22.69 ± 7.65	33.72	25.66 ± 2.57	9.64
2	80	10	1.00	21.92 ± 5.81	26.51	23.33 ± 3.12	13.37

Q = flow rate; C = Concentration; D_n = Number based mean diameter; CV_n = Number based coefficient of variation, D_{pr} = mean diameter of the primary microspheres, CV_{pr} = coefficient of variation of primary diameter, CP = Continuous phase; DP = Dispersed phase.
Primary microspheres are microspheres without satellite microspheres (see text).

The mechanism of droplet formation in a flow focusing system starts first with an elongation of the DP through an orifice followed by pinching off of the DP through different regimes that include geometry-control, dripping, jetting and tip-streaming, which in turn depend on the viscosity and flow rates of the fluids and the interfacial tension between the fluids [38,40,53,54,61,62]. Details of each mechanism were discussed in chapter 1 (section 1.2.4).

Anna and Mayer described criteria that define each regime based on the Ca number of the fluids calculated from **equation 1-13**. The authors showed in a comprehensive study that the geometry-controlled droplet breakup mode occurs at very low flow rates and low capillary numbers ($Ca < 0.1$). By increasing the capillary number, the breakup mode transfers to the dripping regime. At even higher capillary numbers above 0.2, the droplets are generated under the jetting regime. In general, jetting generates polydisperse droplets whereas the droplet size distribution in the geometry-controlled and dripping modes is highly monodisperse.

In our system, the highest Ca number achieved was 0.4 at a CP flow rate of 150 $\mu\text{L}/\text{min}$ which is in the range of Ca number defined by Anna and Mayer for jetting condition. During the droplet generation in our system, jetting conditions were observed characterized by the formation of a long thread into the collecting chamber. At lower flow rates of $Q_{\text{CP}} = 30 \mu\text{L}/\text{min}$ and $Q_{\text{DP}} = 1 \mu\text{L}/\text{min}$, Ca was 0.07. According to the criteria defined by Anna and Mayer [38], at these low flow rates, droplets should be generated under the geometry controlled regime, and therefore, the DP should retract after each droplet separates from the fluid. Microscopic images of the droplet generation at this flow rate (**Figure 2-3**), however, showed that in our chip, no changes in the location of the DP stream was observed during the droplet separation. The observed droplet formation thus seems to be characteristic for the droplet generation under dripping condition.

We speculate that the deviation between our results and criteria defined by Anna and Mayer [38] is due to the type of fluids used in the system. In their study, they used light mineral oil and water and they generated a water in oil emulsion. In our system, we used aqueous PVA solution and polymer solution in chloroform and generated an oil in water emulsion. Substituting the mineral oil with the polymer solution changed the fluids' behavior from Newtonian to non-Newtonian, as the polymer solution is a viscoelastic fluid. These major changes might thus have

influenced the droplet generation considerably. To better characterize the mechanism of droplet generation in our system further investigations are required.

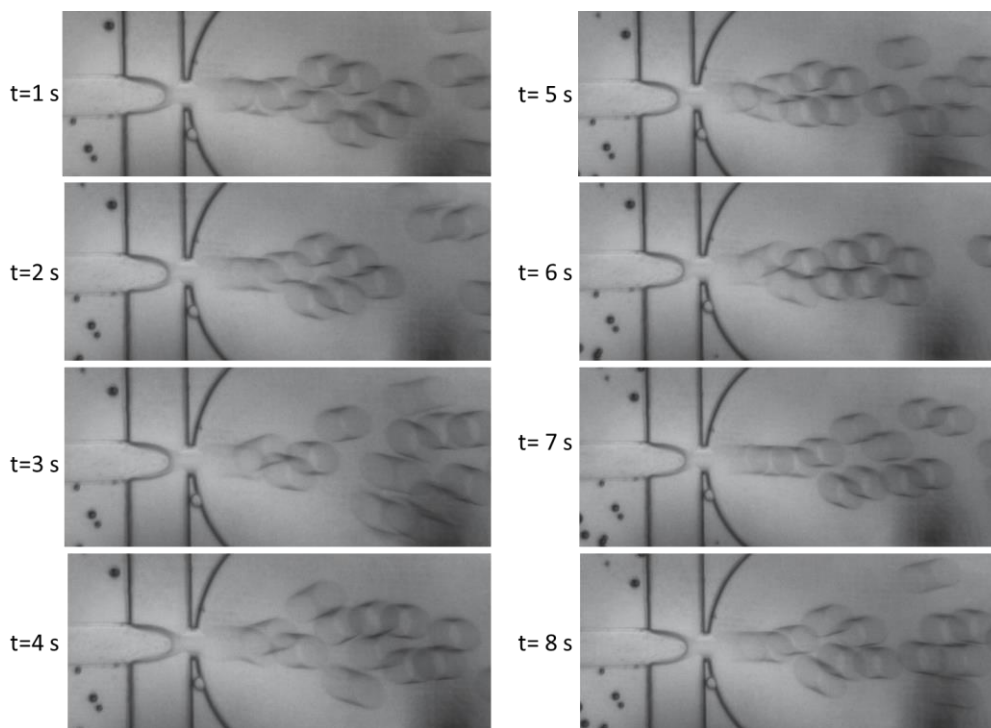


Figure 2-3: Droplet generation in the designed microfluidic flow focusing system. CP was aqueous 2% PVA and its flow rate was 30 $\mu\text{L}/\text{min}$. DP was 10% PLLA in chloroform and its flow rate was 1 $\mu\text{L}/\text{min}$.

In a viscoelastic system, like ours, the formation of satellite droplets depends greatly on the necking process and the pinch off time of the droplet [54,62]. Droplet generation is controlled by both capillary and elastic stresses [53]. Capillary stress will cause squeezing of the fluid stream and thread formation that eventually breaks into droplets whereas elastic stress counteracts the break-off [53,63]. Wagner *et al.* showed that in gravity assisted droplet generation, the balance between the capillary stress and elastic stress causes symmetrical elongation of the dispersed phase followed by necking, thread formation, and droplet pinch off [62]. They showed that the satellite droplets will not form if the neck remains symmetrical when the thread forms and

droplet is separated. Steinhaus *et al.* reported that a symmetrical neck is only observed in microfluidic flow focusing for high molecular weight polymer solutions (1000 kDa) [53]. In our experiments, symmetrical necking was observed during the droplet separation, however, we could not completely eliminate the formation of satellite droplets.

Drezsi *et al.* (2013) showed that the formation of satellite droplets in viscoelastic systems is also influenced by the viscosity ratio of the fluids. They reported that satellite droplet formation can be eliminated or significantly reduced at a viscosity ratio greater than 1 ($\mu_{DP}/\mu_{CP} > 1$) [54].

In our experiments, the dispersed phase was selected as 10% PLLA dissolved in chloroform. Based on the Yue *et al.* discussion, low concentration polymer solution such as ours can be considered as a viscoelastic fluid [64]. Its viscosity at low shear rate (1/s) was equal to 2.92 cP. The viscosity of the continuous phase, 2% PVA in water, was similar to water, 1 cP. The viscosity ratio of the fluids in our system (μ_{DP}/μ_{CP}) was therefore 2.92 which should have eliminated satellite droplet formation.

The combination effects of symmetrical necking of the dispersed phase and viscosity ratio of dispersed phase to continuous phase reduced the number of satellite droplets formed in our system, but could not completely eliminate it. Other factors might thus cause formation of satellite droplets, such as the accuracy and precision of the pumps which are not able to deliver the exact flow rate without fluctuation. Further investigation is required to establish a mathematical correlation between these parameters.

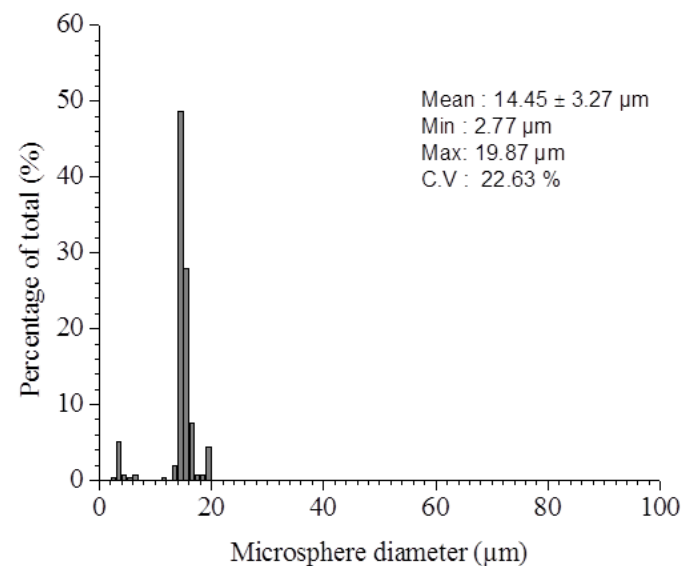
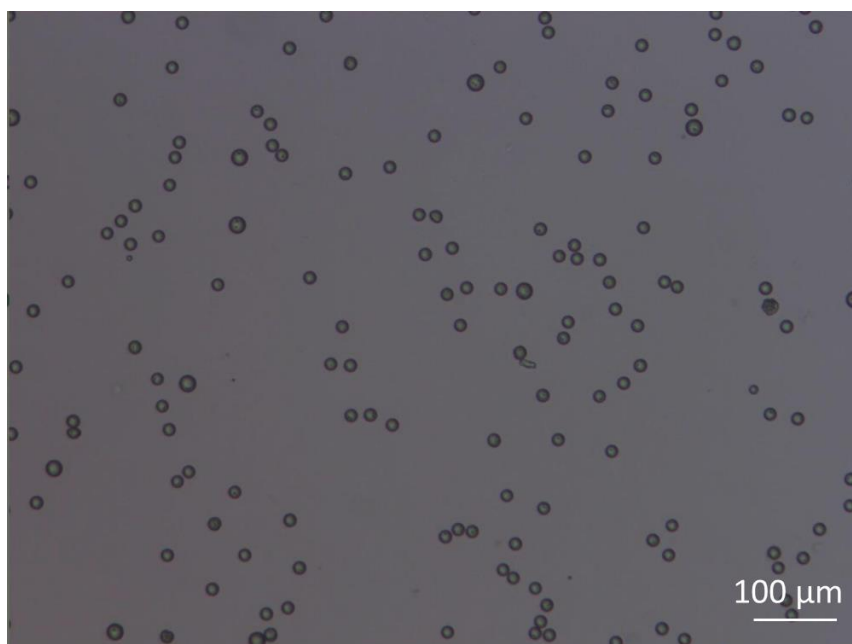


Figure 2-4. Microscopic pictures and size distribution of PLLA microspheres produced in a glass microfluidic flow focusing system. CP is 1% PVA and its flow rate is 100 $\mu\text{L}/\text{min}$ and DP is 2% PLLA and its flow rate is 0.5 $\mu\text{L}/\text{min}$. The Y-axis shows the number weighted microsphere fractions.

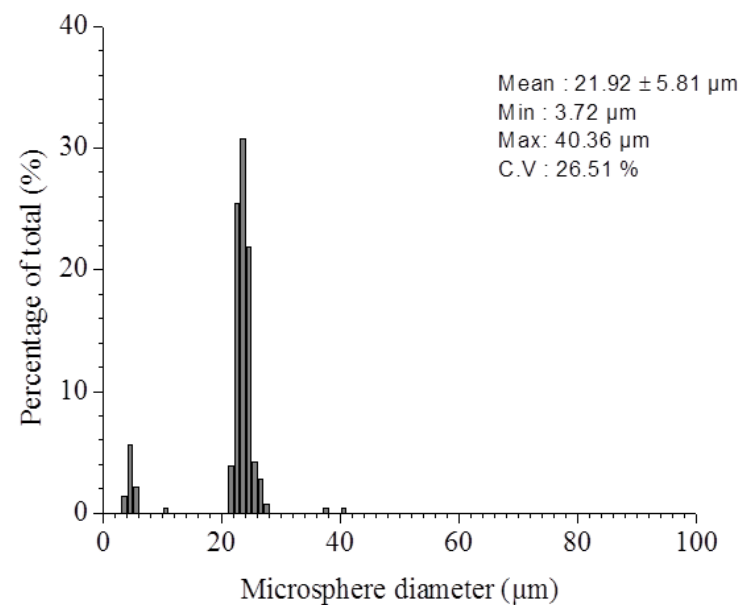
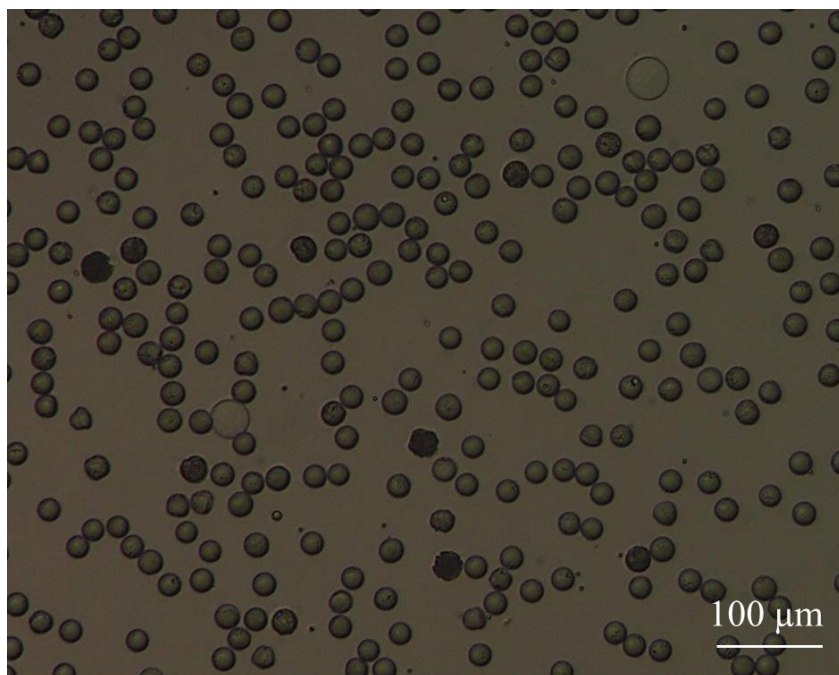


Figure 2-5. Microscopic pictures and size distribution of PLLA microspheres produced in a glass microfluidic flow focusing system. CP is 2% PVA and its flow rate is $80 \mu\text{L}/\text{min}$ and DP is 10% PLLA and its flow rate is $1 \mu\text{L}/\text{min}$. The Y-axis shows the number weighted microsphere fractions.

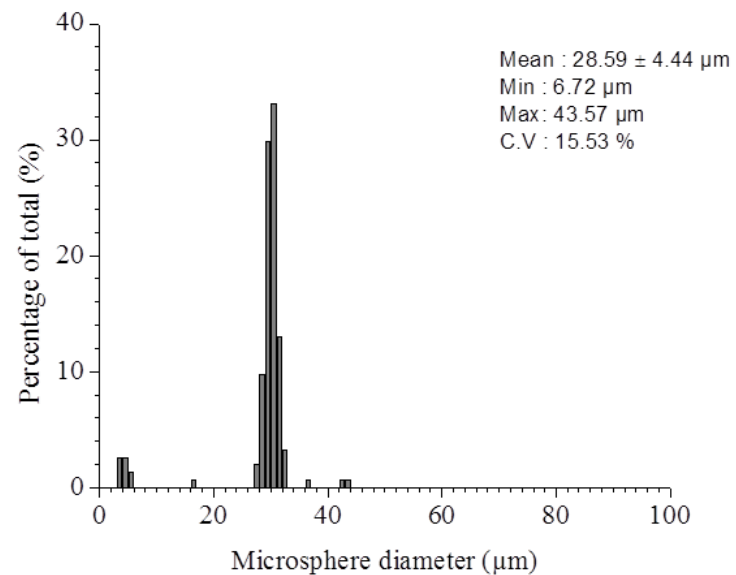
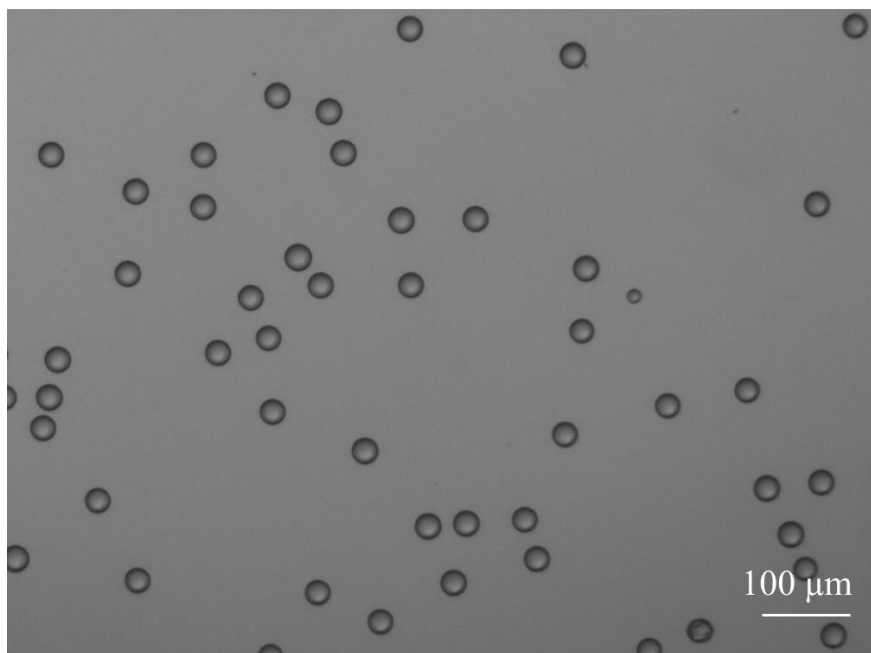


Figure 2-6. Microscopic pictures and size distribution of PLLA microspheres produced in a glass microfluidic flow focusing system. CP is 2% PVA and its flow rate is 60 μL/min and DP is 10% PLLA and its flow rate is 1 μL/min. The Y-axis shows the number weighted microspheres fractions.

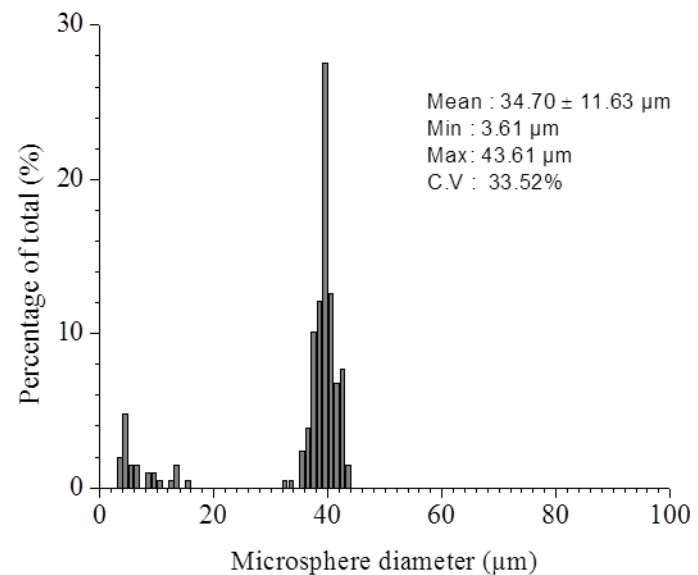
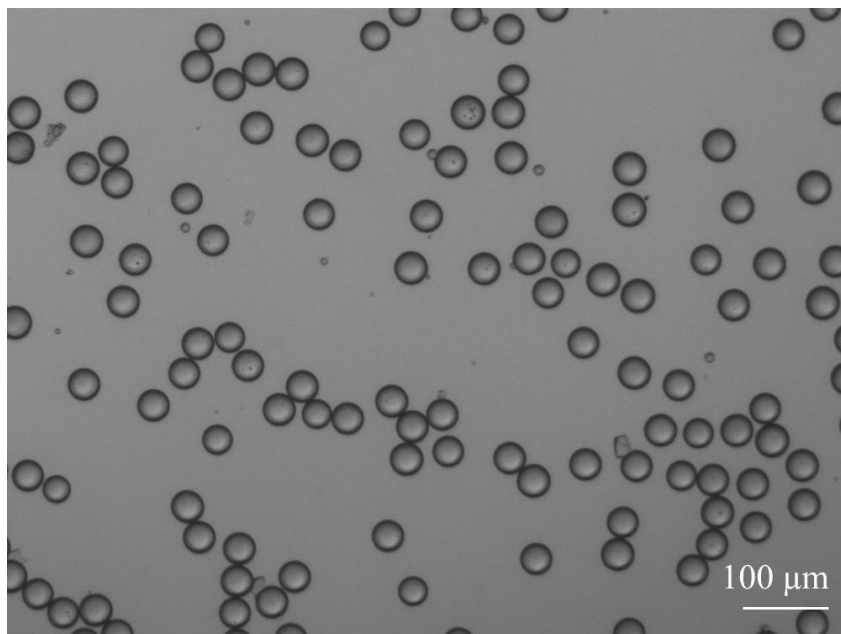


Figure 2-7. Microscopic pictures and size distribution of PLLA microspheres produced in a glass microfluidic flow focusing system. CP is 2% PVA and its flow rate is $30 \mu\text{L}/\text{min}$ and DP is 10% PLLA and its flow rate is $1 \mu\text{L}/\text{min}$. The Y-axis shows the number weighted microsphere fractions.

2.2.3 Preparation of PEGylated Monosized PLLA Microspheres

PEGylation, covalent bonding of poly (ethylene glycol) to polymer, can improve bioavailability, biocompatibility, safety and immunogenicity of the polymer microspheres. It is also known that conjugating PEG to proteins can prevent protein denaturation during protein encapsulation [65]. Therefore, it is important to be able to produce monosized PLLA microspheres containing a PEG coating in one step in the microfluidic flow focusing system. Since PEG is a hydrophilic polymer, it does not dissolve in chloroform, so instead of a PEG homopolymer, mPEG-b-PDLLA copolymer is used. This copolymer behaves like a surfactant at the water-chloroform interface. The hydrophobic end of the polymer (PDLLA) remains in the chloroform phase while the hydrophilic end (PEG) goes into the water phase which results in uniform coating of dried PLLA microspheres with PEG.

The addition of a second polymer to the dispersed phase affects the physicochemical properties of the DP and consequently is expected to affect the size and size distribution of the particles generated. **Figure 2-8** to **Figure 2-11** shows the size distributions of microspheres prepared at different mPEG-b-PDLLA concentrations.

Adding the copolymer leads to a reduction in the size of the particles produced (**Figure 2-12**). The amphiphilic molecule mPEG-b-PDLLA reduces the interfacial tension at the interface of water and chloroform that results in the lower interfacial energy. Lower interfacial tension results in higher Ca number. It was discussed in chapter 1 that increasing the Ca number results in production of droplets with smaller diameters as mechanism of droplets generation is changing from geometry controlled to jetting mode.

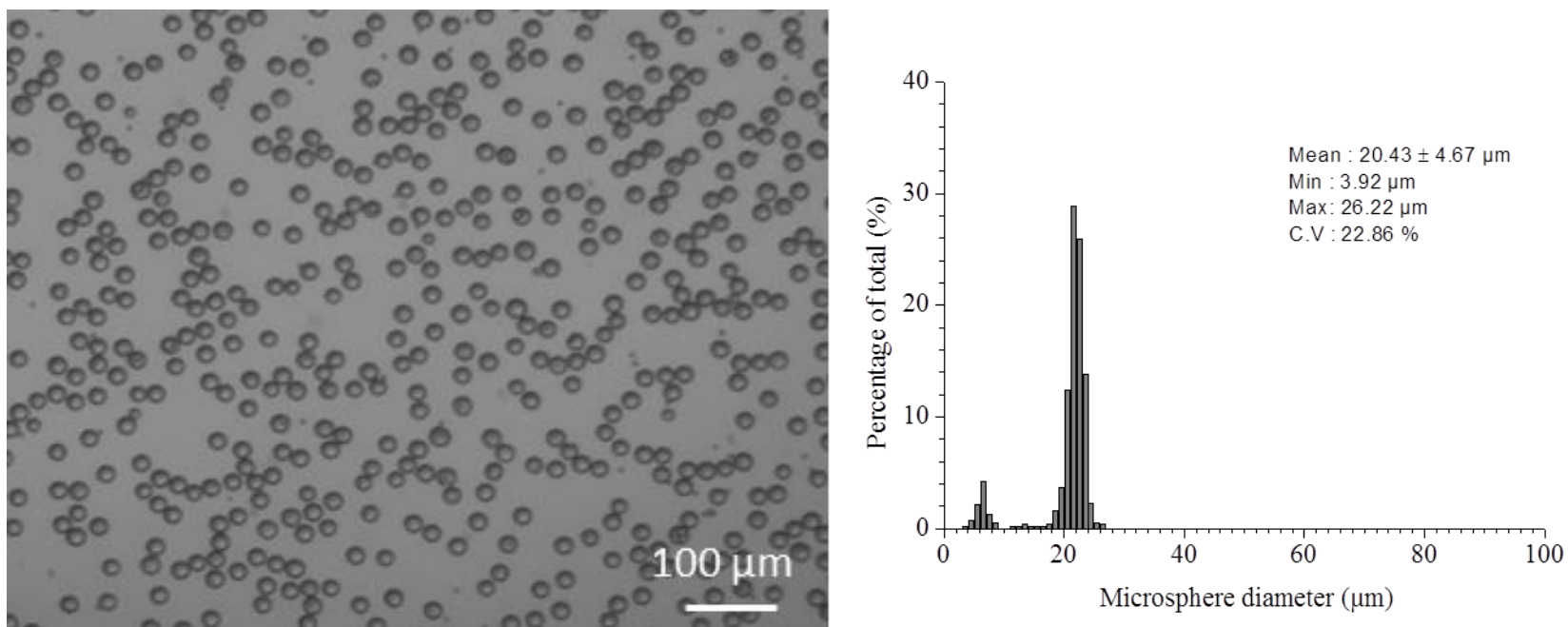


Figure 2-8. Microscopic pictures and size distribution of pegylated PLLA microspheres with narrow size distribution produced in a glass microfluidic flow focusing system. The continuous phase was 2% PVA in water and its flow rate was 120 μL/min. Dispersed phase was 10% polymer in chloroform and its flow rate was 1 μL/min.

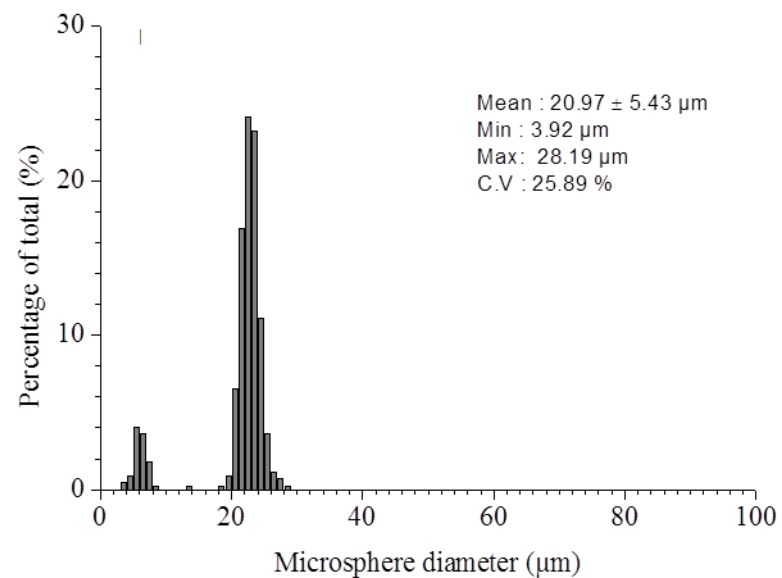
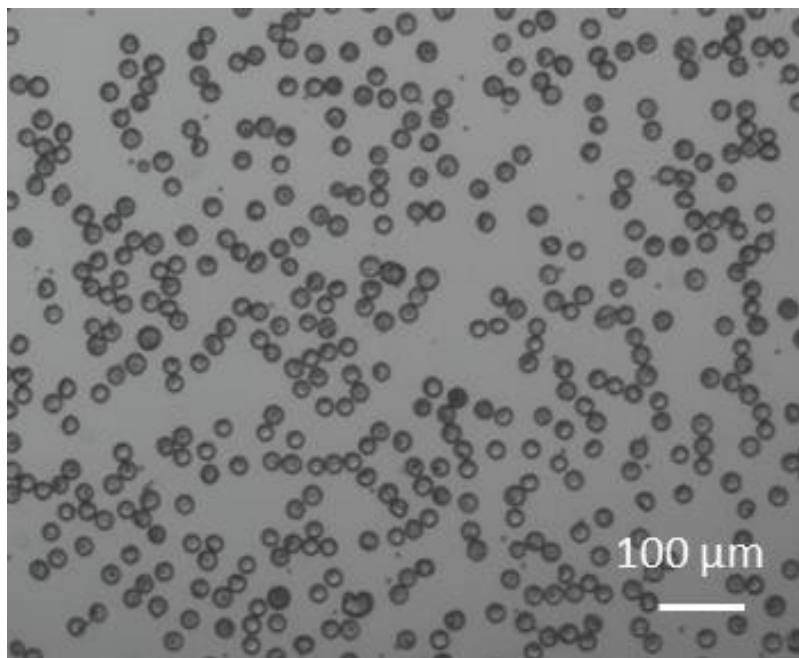


Figure 2-9. Microscopic pictures and size distribution of pegylated PLLA microspheres with narrow size distribution produced in a glass microfluidic flow focusing system. The continuous phase was 2% PVA in water and its flow rate was 120 $\mu\text{L}/\text{min}$. Dispersed phase was 10% polymer (95 % PLLA and 5% mPEG-b-PDLA) in chloroform and its flow rate was 1 $\mu\text{L}/\text{min}$.

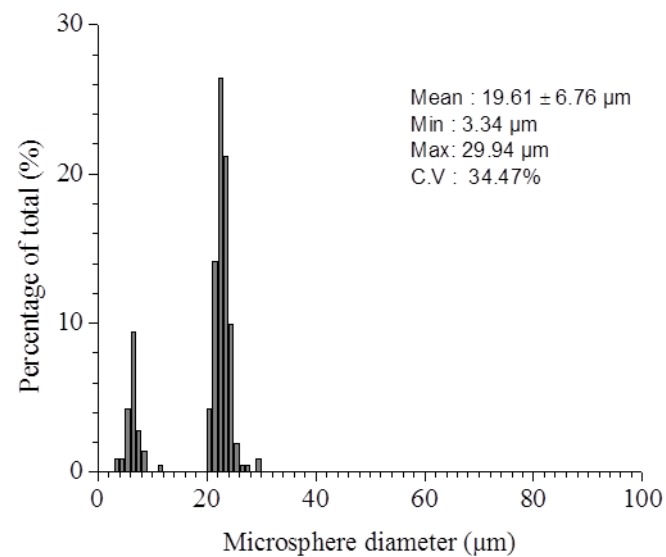
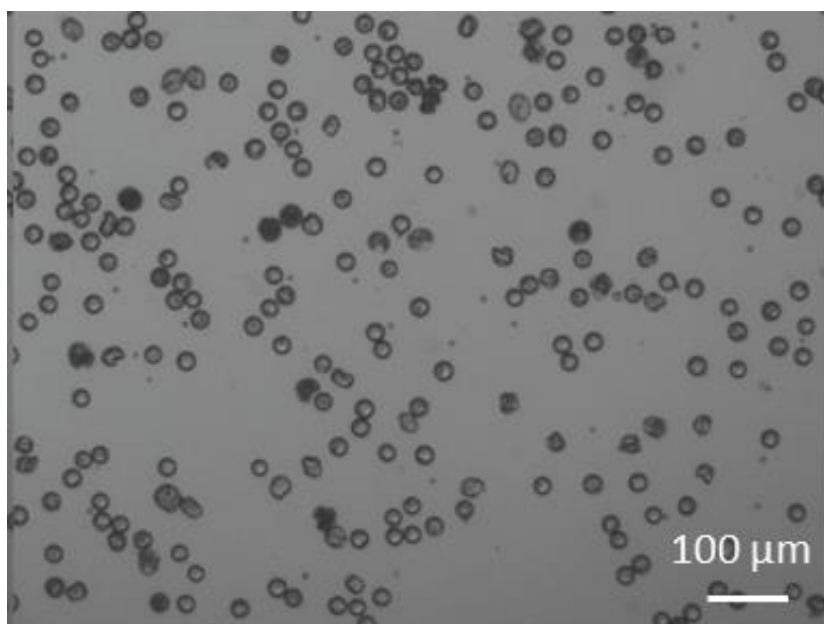


Figure 2-10. Microscopic pictures and size distribution of pegylated PLLA microspheres with narrow size distribution produced in a glass microfluidic flow focusing system. The continuous phase was 2% PVA in water and its flow rate was 120 μL/min. Dispersed phase was 10% polymer (75 % PLLA and 25% mPEG-b-PDLA) in chloroform and its flow rate was 1 μL/min.

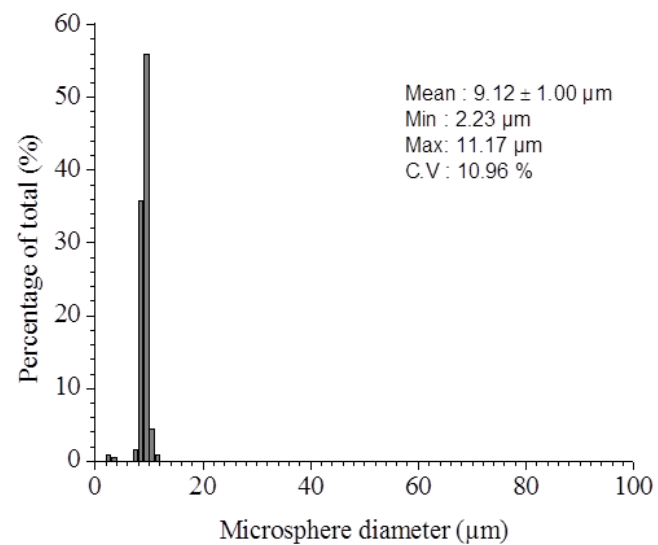
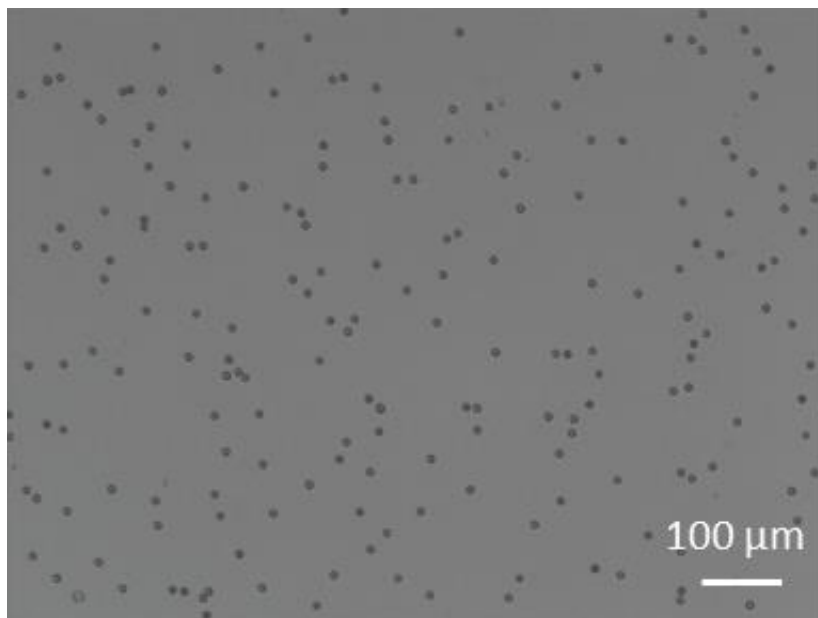


Figure 2-11. Microscopic pictures and size distribution of pegylated PLLA microspheres with narrow size distribution produced in a glass microfluidic flow focusing system. The continuous phase was 2% PVA in water and its flow rate was 120 μL/min. Dispersed phase was 10% polymer (50 % PLLA and 50% mPEG-b-PDLA) in chloroform and its flow rate was 1 μL/min.

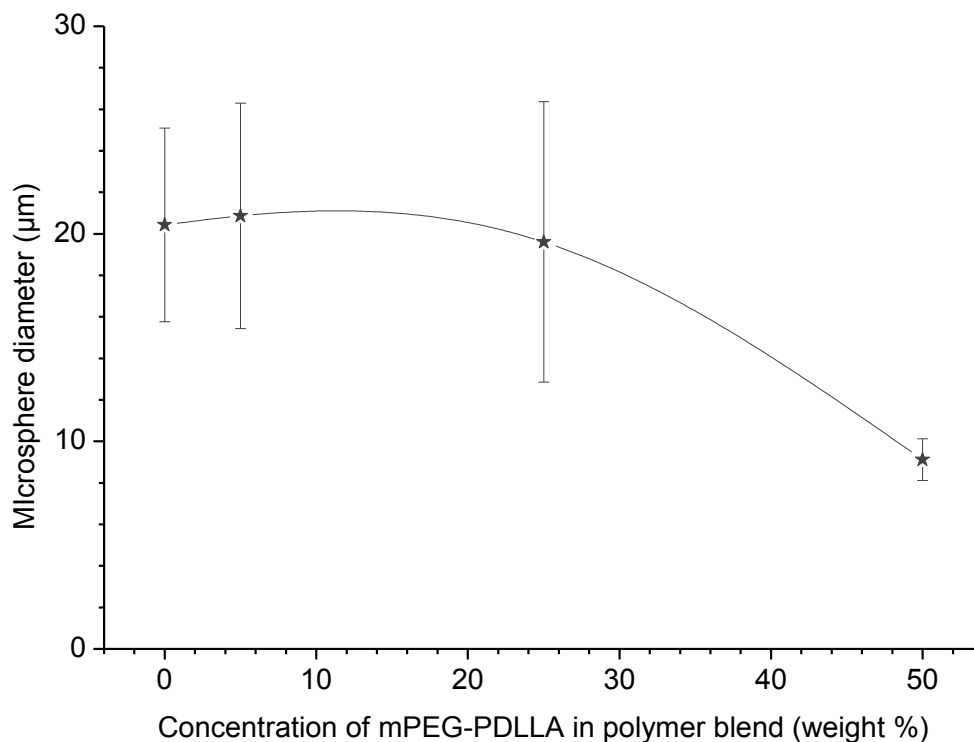


Figure 2-12 : Effect of mPEG-PDLLA concentration in polymer blend on average particles size of the microspheres produced in the microfluidic flow focusing system. The flow rate of the continuous phase was 120 µL/min and that of the dispersed phase 1 µL/min.

2.2.4 Morphology of Produced PLLA Microspheres

The surface smoothness of the poly(lactic acid) and poly(lactic-co-glycolic acid) microparticles produced by emulsification depends on the mechanism and rate of solvent removal from the droplets [66-69]. Fast solvent removal results in the formation of particles with a smooth surface [67]. In our experiments, the polymer droplets were added slowly (1 µL/min) to a beaker containing 2% PVA solution (10 mL). The dilution rate thus was large, and solvent extraction from the droplets relatively fast, leading to smooth surfaces. SEM of the microspheres confirms that all the generated microspheres have smooth surface (**Figure 2-13**). In addition, the relatively narrow size distribution was also confirmed.

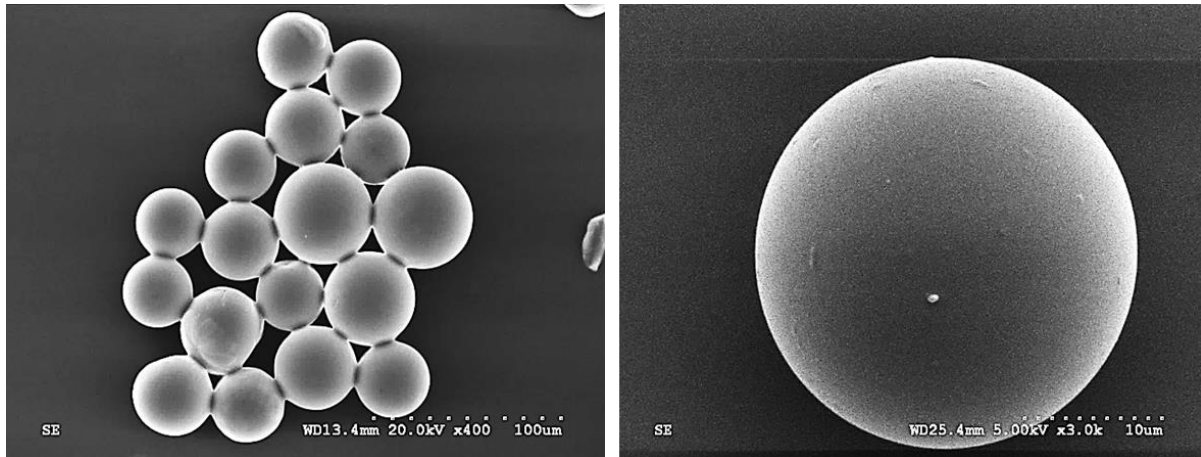


Figure 2-13 : Scanning electron microscopy images of PLLA microspheres.

2.3 Monosized PLLA Microspheres Production for Medical Applications

Monosized polymer microspheres are useful for different therapeutic and diagnostic applications [49,70,71]. They can be used for active and passive drug targeting, for sustained release of therapeutic compounds, as carriers in gene therapy and as imaging tools in nuclear medicine. Here, we show how our narrowly sized PLLA microspheres can be used in two medical applications: in diagnostic lung perfusion imaging and therapeutic liver radioembolization.

2.3.1 Diagnostic Lung Perfusion Imaging

Lung perfusion imaging is a very common diagnostic technique used to determine blood circulation deficiencies in the lung. For this purpose, macroaggregated human albumin (MAA) is labeled with ^{99m}Tc and injected into the left arm vein. The radiolabeled particles will reach the lung after passing through the right heart chamber where they will be trapped by the lung capillaries. Any blood flow abnormalities in the lung will become visible as hypoactive areas on the nuclear medicine lung scan.

Macroaggregated albumin is a non-spherical particle with a wide size distribution generally between 10-100 μm [72]. Such a wide size distribution of particles may cause entrapment of the

radiolabeled particles inside arterioles of the lung and also affect the particles' biodistribution [72]. Therefore, monosized biodegradable polymer microspheres with a chelator on its surface for ^{99m}Tc attachment might be an improved substitute for MAA. Similar to MAA, the PLLA microspheres are biodegradable and are eliminated from the body without any side effect. They are biocompatible and FDA-approved with no risk of immunogenicity.

2.3.1.1 Production of Functional Monosized PLLA Microspheres

Monosized PLLA microspheres were produced based on the protocol explained in section 2.1.2. The continuous phase was an aqueous 2% PVA solution, while the dispersed phase was a 5% chloroform solution of PLLA, bis(picolyamine)-functionalized PLA [73] and pegylated polycaprolactone (MePEG₁₇-b-PCL₁₀) [74]. Bis(picolyamine)-functionalized PLA was used as the ^{99m}Tc -chelating polymer and pegylated polycaprolactone provided the microspheres with a hydrophilic surface to minimize sticking to surfaces.

2.3.1.2 Results

The particle size distribution was narrow and monodisperse (**Figure 2-14**) with a coefficient of variation of 4.9%.

The applicability of the produced microspheres for lung perfusion imaging was tested by injecting 0.2 mg of the ^{99m}Tc labeled particles into the tail vein of a mouse followed by microSPECT/CT imaging on an X-SPECT instrument (Gamma Medica, Northridge, California, U.S.A.; now Siemens) at McMaster's Centre for Preclinical and Translational Imaging (MCPTI) in Hamilton, Ontario, Canada. MicroSPECT/CT imaging showed that most of the particles accumulated uniformly in the mouse' lung (**Figure 2-15** and **Table 2-3**). Only minor amounts of the radioactivity were found in other organs (**Table 2-3**). A detailed discussion of the results is

beyond the scope of this thesis and can be found in the article published in the journal of Biomacromolecules [69].

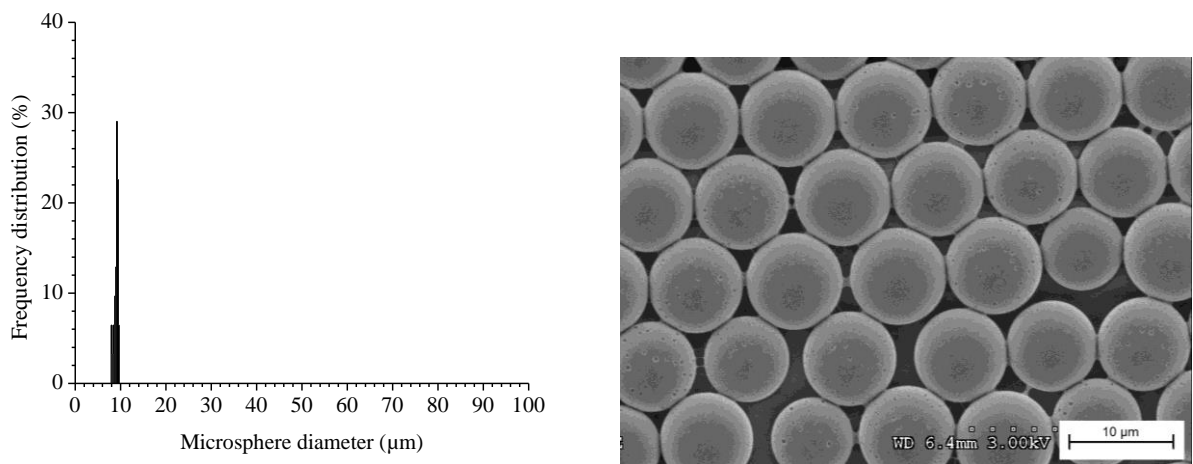


Figure 2-14 : Size distribution and scanning electron microscopy (SEM) of the biodegradable PLLA microspheres.



Figure 2-15. Volume-rendered microSPECT/CT image taken 5 minutes after tail vein injection of 0.2 mg of the ^{99m}Tc -radiolabeled microspheres into a healthy mouse. The radioactivity is shown in red.

Table 2-3. Activity distribution of the ^{99m}Tc-Microspheres 15 Min after Tail Vein Injection into C57Bl/6 Mice (n = 6).

	Injected Dose (%) ± SD	Organ/Blood Ratio ± SD	Injected Dose (%/g) ± SD
Blood	5.90 ± 0.95	1.00 ± 0.00	2.50 ± 0.09
Heart	0.18 ± 0.05	0.35 ± 0.09	0.98 ± 0.30
Lungs	79.61 ± 3.79	103.47 ± 27.10	333.65 ± 83.79
Liver	7.88 ± 1.44	1.72 ± 0.04	4.29 ± 0.14
Kidney	1.28 ± 0.11	0.94 ± 0.02	2.34 ± 0.03
Spleen	0.87 ± 0.14	3.06 ± 0.39	7.69 ± 0.82
Intestine	0.48 ± 0.15	0.20 ± 0.04	0.50 ± 0.10
Stomach	0.39 ± 0.51	0.99 ± 1.24	2.48 ± 3.11
Muscle	3.34 ± 0.77	0.07 ± 0.01	0.18 ± 0.04
Brain	0.07 ± 0.03	0.04 ± 0.01	0.10 ± 0.08

2.3.2 Therapeutic Liver Radioembolization

Radioembolization is a cancer treatment method in which micron size particles labeled with radioisotope material are injected into the blood stream which leads to the tumour as directly as possible. The particles are trapped in the capillary bed of the tumor because their diameter is larger than the size of the capillaries. The radioactive particles then emit radiation that can kill the nearby tumor cells [75]. The method is mainly used for the treatment of liver cancer, in particular for inoperable hepatocellular carcinoma (HCC). In this method, microspheres of between 25-35 µm are directly injected into the hepatic artery. The blood transports the particles toward the liver where they are trapped inside capillaries surrounding the tumor. Since liver tumors receive their blood supply mainly through the hepatic artery and normal liver cells receive their blood supply mainly through the portal vein, the blockage of tumor capillaries by radiolabeled particles does not, or only minimally, affect the normal liver cell survival [76].

The effectiveness of the treatment depends on the average size and size distribution of the particles. The optimum particle size is between 20-40 μm [76]. Smaller particles might not be retained inside the tumor capillaries and can pass into the venous circulation and leave the liver while very large particles might not reach the capillaries and clog other parts of the hepatic artery and arterioles away from the tumor [76]. Currently approved microspheres for liver radioembolization are yttrium-90 (^{90}Y) labeled resin particles (SIR-Spheres, SIRTEX, North Sydney, Australia) and glass particles (TheraSpheres, BTG International, Ottawa, Ontario, Canada). The particles sizes are between 20-60 μm and 20-30 μm , respectively, and are non-biodegradable.

To further improve the efficacy of the method, current microspheres should be replaced by monosized biodegradable polymer microspheres, so that the biodistribution of the particles is more predictable and that they are eliminated from the body after the radioisotope has decayed completely. Biodegradable poly (L-lactic acid) is an appropriate candidate for this application when it is produced with averages sizes between 30-40 μm .

Therefore, to be able to produce large monosized microspheres in our microfluidic system, the polymer concentration was increased to 16% and DP flow rate was changed from 0.5 $\mu\text{L}/\text{min}$ to 3 $\mu\text{L}/\text{min}$. Increasing the polymer concentration led to the production of large particles with narrow size distribution (**Figure 2-16** to **Figure 2-19**). There was no significant effect of DP flow rate on the size and size distribution of the particles. The best results, however, were obtained at DP = 1 $\mu\text{L}/\text{min}$.

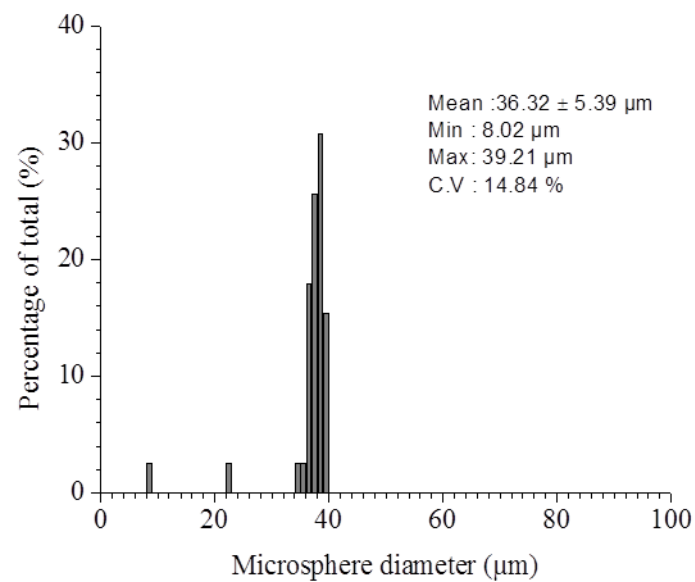
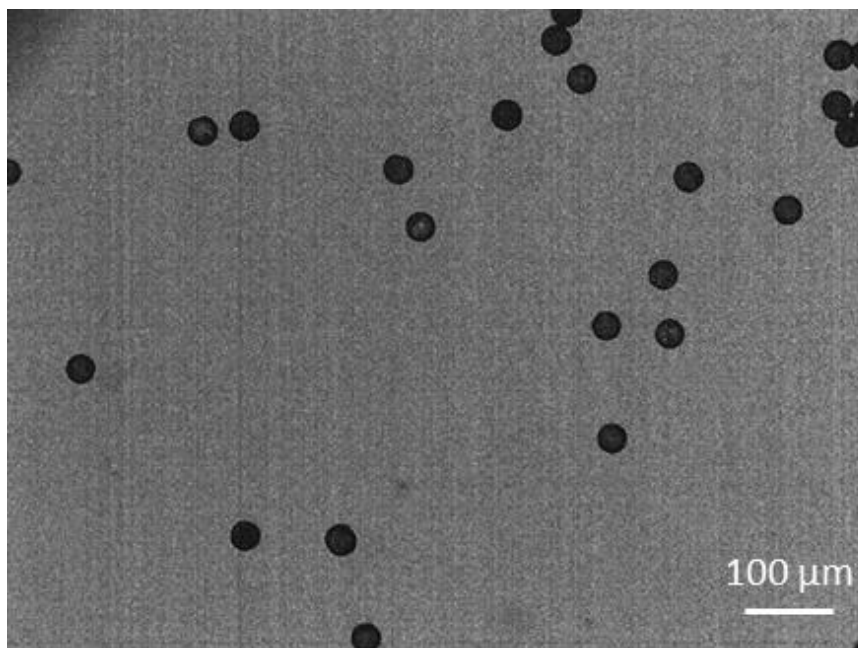


Figure 2-16. Microscopic pictures and size distribution of large PLLA microspheres with narrow size distribution produced in a glass microfluidic flow focusing system. Continuous phase was aqueous 2% PVA and its flow rate was 20 $\mu\text{L}/\text{min}$. The dispersed phase was 16% PLLA in chloroform and its flow rate was 3 $\mu\text{L}/\text{min}$.

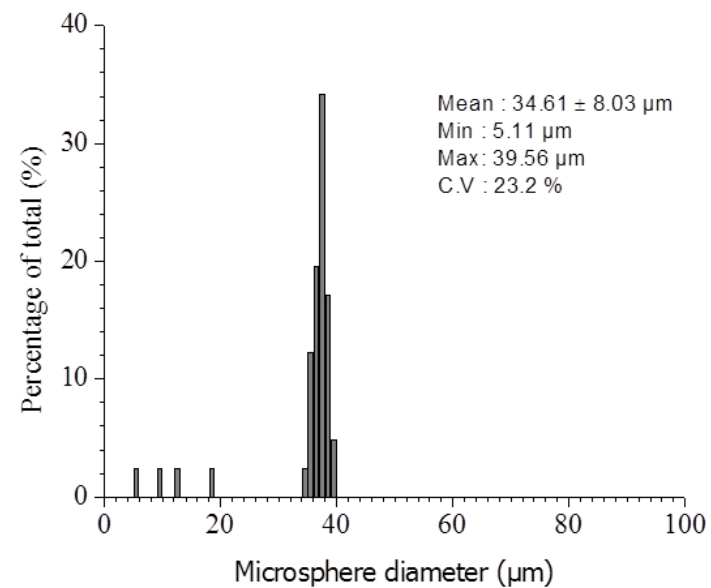
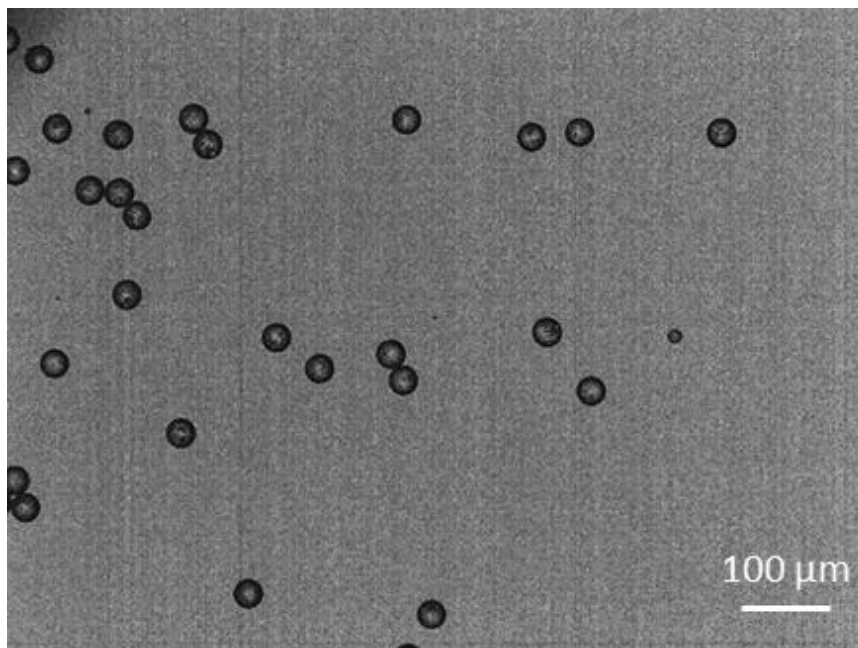


Figure 2-17. Microscopic pictures and size distribution of large PLLA microspheres with narrow size distribution produced in a glass microfluidic flow focusing system. Continuous phase was aqueous 2% PVA and its flow rate was 20 $\mu\text{L}/\text{min}$. The dispersed phase was 16% PLLA in chloroform and its flow rate was 2 $\mu\text{L}/\text{min}$.

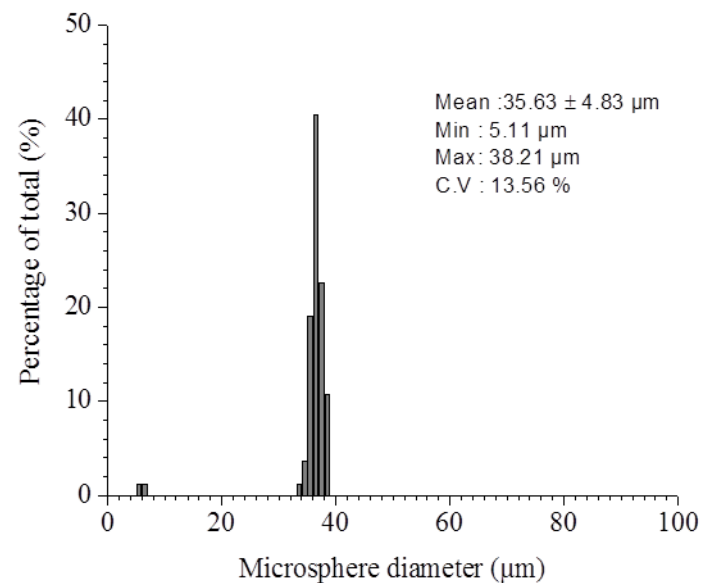
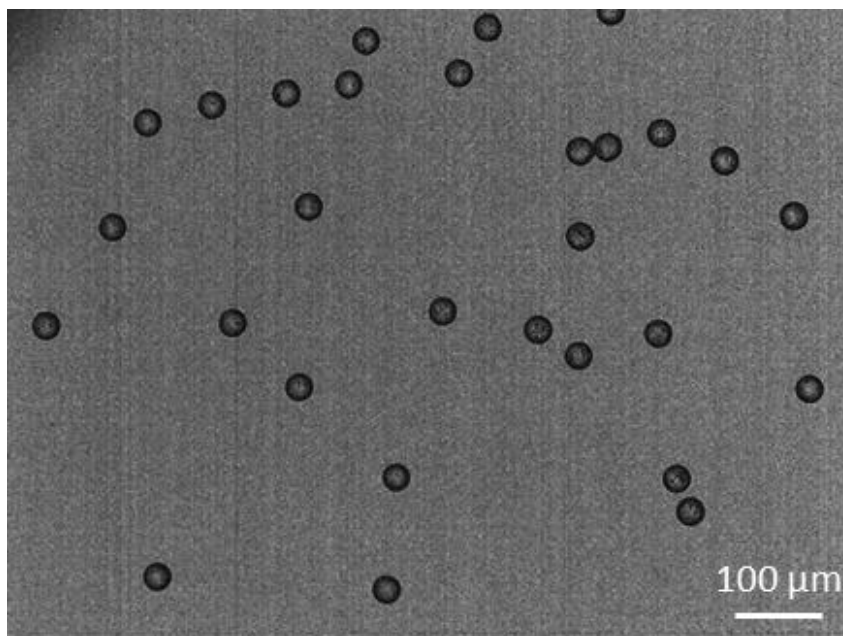


Figure 2-18. Microscopic pictures and size distribution of large PLLA microspheres with narrow size distribution produced in a glass microfluidic flow focusing system. Continuous phase was aqueous 2% PVA and its flow rate was 20 μL/min. The dispersed phase was 16% PLLA in chloroform and its flow rate was 1 μL/min.

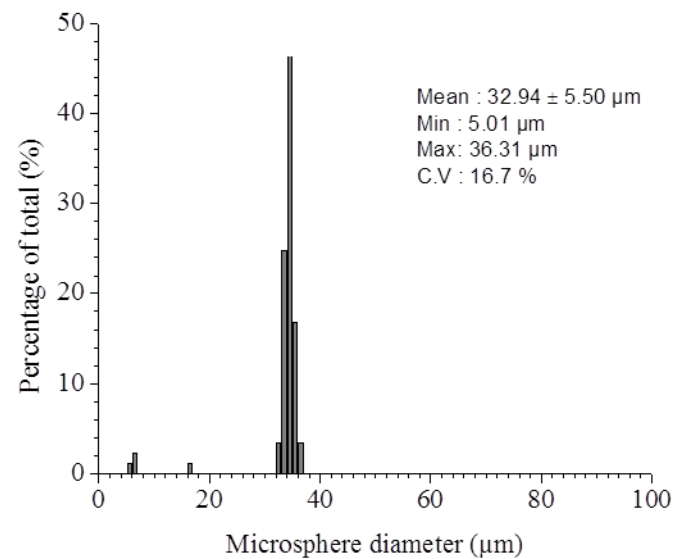
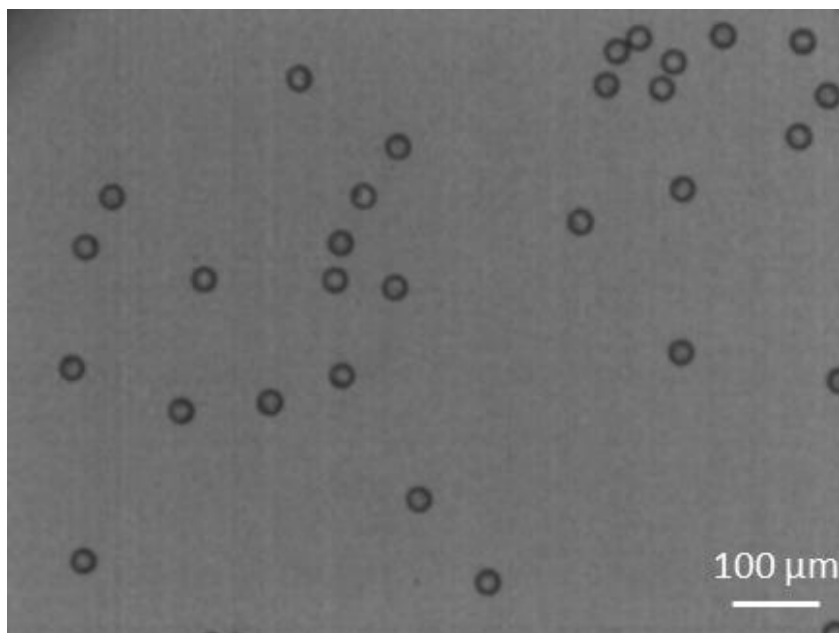


Figure 2-19. Microscopic pictures and size distribution of large PLLA microspheres with narrow size distribution produced in a glass microfluidic flow focusing system. Continuous phase was aqueous 2% PVA and its flow rate was 20 μL/min. The dispersed phase was 16% PLLA in chloroform and its flow rate was 0.5 μL/min.

To produce microspheres for the application in radioembolization, it is necessary to mix the polymers with a chelator and PEG. Both will arrange themselves on the surface of the particles after solvent removal. The chelator is used to bind radioisotopes to the particles right before injection, while PEG gives the particles better circulation properties in the blood stream. It has been shown that the addition of PEG reduces the size of the particles (discussed in the section 2.2.4) , so to compensate for that, the polymer concentration in the DP was increased to 20%.

Figure 2-20 shows the microscopic image and the size distribution of the generated microspheres. Increasing the polymer concentration not only increased the average size of the particles, but it also had the effect of reducing the number of satellite droplets, further improving the size distribution. The reduction of satellite droplets was due to the higher viscosity of the polymer solution, as explained before (see section 2.2.2).

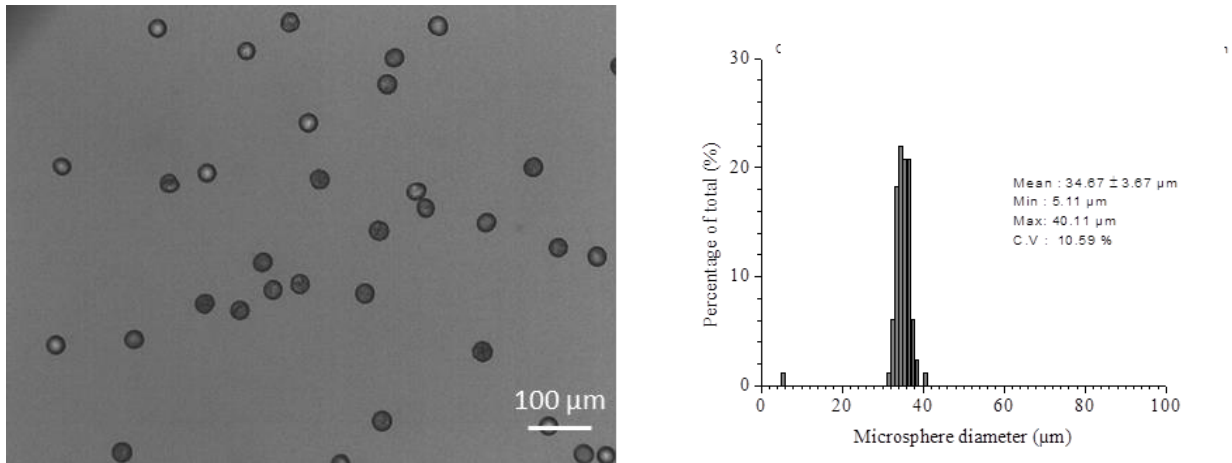


Figure 2-20 : Size distribution of PLLA microspheres coated with ^{99m}Tc chelator and PEG fabricated for radioembolization study. The concentration of polymer in chloroform was 20% (w/v) and the polymer composition was 92% PLLA, 5% ^{99m}Tc chelator and 3% pegylated polymer. DP flow rate was 1 $\mu\text{L}/\text{min}$. The continuous phase consisted of 2% PVA at a flow rate of 20 $\mu\text{L}/\text{min}$.

The labeling efficiency was tested and high labeling efficiency was obtained with good stability *in vitro* (data not shown). The effectiveness of these particles will be tested in an animal model of liver cancer. Preparations for these *in vivo* experiments are ongoing.

2.4 Conclusions

A microfluidic flow focusing chip was designed and fabricated that can produce quasi-monosized PLLA microspheres with distinct sizes between 7 to 40 μm . Monosized particles result from monosized polymer-rich droplets generated within the system by carefully controlling the flow rate of the fluid and their physicochemical properties. The results indicate that the optimal flow rates for the production of quasi-monosized microspheres occur when droplets are produced under the dripping regime. Yet, further optimization of physicochemical properties of the fluid (e.g., adjustment of viscosity, density and interfacial tension) and geometry of the chip are required to reduce the number of satellite droplets formed and to be able to produce larger microspheres.

The morphology of the PLLA particle surface was smooth as shown by SEM.

The functional particles with $^{99\text{m}}\text{Tc}$ chelator and PEG on the surface were also of narrow size distribution. The addition of these amphiphilic polymers to the PLLA polymer solution, however, reduced the size of the microspheres by decreasing the interfacial tension between CP and DP.

Overall, our results show that the designed microfluidic flow focusing chip can generate polymer microspheres with narrow size distribution reliably and reproducibly. The same chip was successfully used for the production of PLGA microspheres as well in our lab. We are expecting that our chip can also be used for the production of polymeric microspheres from other

polymeric materials that are currently produced by bulk emulsification / evaporation techniques, such as poly(anhydrides).

Chapter 3: Three-Dimensional Computational Simulation of Droplet Generation in our Microfluidics Flow Focusing System

3.1 Introduction

Modern microfluidic technologies are able to generate droplets in a precise way, which can then be turned into also very precisely sized microspheres. The production of such monodisperse microspheres depends on flow characteristics in co-flowing, immiscible fluids, the geometry of the microfluidic channels, the physicochemical properties of the fluids, and the interfacial tension between the fluids. Small variations in any of these parameters can have a great impact on the size and the size distribution of the initial droplets and therefore on the final particles, and on the reproducibility of the process. The required optimization of the system is a demanding and time-consuming process. One method for fast, inexpensive, accurate, and precise prediction of the appropriate conditions and geometries for the production of the monodispersed droplets is computational simulation.

The computational simulation of droplet generation in microfluidic flow focusing requires a multiphase flow modeling system as two or more immiscible fluids are involved in the process. The immiscible fluids are separated from each other due to differences in their physicochemical properties and form distinct interfaces. Droplet generation takes place as a result of differences in the flow of these fluids and the forces along their interface [27].

Constantly moving and changing fluid interfaces make the numerical modeling of changes in the flow system complicated [64]. To allow modeling of these changes, the flow system is broken into small segments (or grids), creating a 2- or 3-dimensional mesh of the flow system under investigation. The corner points (or nodes) of these segments are used to define local boundary conditions, starting points for the numerical analysis of the entire flow system. There

are several approaches used to define a fluid boundary and to simulate droplet generation in microchannels. Among the more prominent are: (i) interface tracking where the motion of the interface is followed and the grid points move with the same velocity as the average fluid velocity at that point. This method can accurately simulate the onset of droplet break up, but it requires re-meshing after the droplet formation, which increases the complexity of the model and significantly increases the computational resources needed [64,77]; (ii) interface capturing, which uses a static grid and where the interface is defined by a finite thickness and the mesh along the interface is reconstructed after each time step [64,78,79]. Interface capturing is considered less complicated and can be used for the simulation of droplet break up in microfluidic systems with good accuracy [63,64,77,80-82]; and (iii) static meshing, where the flow system is defined by a discrete mesh that can be non-uniform to increase the number of nodes around areas of interest (e.g., fluid interfaces, areas of droplet breakup). The interface in this method is reconstructed based on a Volume of Fluid (VOF) approach and the spatial discretization between nodes is defined by a gradient.

The majority of the numerical models in the scientific literature used to investigate the droplet generation in microfluidic systems use the interface capturing method in planar 2D. As a result, a variation of flow parameters in the z -direction (depth of the channels) has been ignored or assumed to have no impact on the process. It can be argued that the instability condition of the disperse phase (DP) thread in 3D would be different from the one observed in 2D [83]. More accurate predictions of the droplet size are thus expected from a 3D model.

Here, a simple 3D model is used based on a static non-uniform grid and the VOF method to simulate droplet generation in a microfluidic flow focusing system and to investigate effects of operational conditions on the mechanism of droplet generation and the size of the droplets.

3.2 Computational Flow Modeling and Data Analysis

3.2.1 Computational Fluid Dynamics

The three-dimensional multiphase fluid software Fluent (ANSYS Inc., Canonsburg, PA, USA) was used to simulate the fluid flow profiles, droplet formation and droplet breakup in our glass chip geometry. To allow for a comparison to the on-chip experiments, different flow rates of the DP and CP were studied. In order to minimize computational time while retaining accuracy of the simulation, only a half-symmetry of the flow focusing design was simulated. The design was converted into finite elements using a hexahedral meshing strategy with a non-uniform mesh density (~482,000 nodes). The phase material properties used in the simulations were the same as those used in the bench-top studies. Properties of a 10% PLLA (2-3 kDa) solution ($\rho = 1480 \text{ kg / m}^3$, $\mu = 2.92 \times 10^{-3} \text{ kg / m}\cdot\text{s}$) were used for the DP, while properties of water ($\rho = 998 \text{ kg / m}^3$, $\mu = 1.03 \times 10^{-3} \text{ kg / m}\cdot\text{s}$) were used for the CP. The concentration of poly(vinyl alcohol) used in the aqueous solution was low and the difference to the properties of water were negligible in terms of density and viscosity.

A “Volume of Fluid” (VOF) multiphase model was used for the two phase explicit VOF scheme, a volume fraction cutoff of 10^{-6} , and a Courant number of 0.25. The phase interaction was defined with wall adhesion properties and an interfacial tension of 5 mN / m (measured by pendant droplet method using an optical tensiometer; Attension Theta, KSV Instrument, Helsinki, Finland). The boundary conditions were then defined as follows: DP and CP inlets had a flat velocity profile with varying flow velocities depending on the parameter studied (with values ranging from $2.98 \times 10^{-4} \text{ m / s}$ to $5.95 \times 10^{-3} \text{ m / s}$ and $2.21 \times 10^{-2} \text{ m / s}$ to $1.10 \times 10^{-1} \text{ m / s}$, respectively); the outlet was defined as outflow with constant pressure ($P_{\text{outlet}} = P_{\text{atm}} = 101,325 \text{ Pa}$); the walls enclosing the chip were defined as a stationary wall, with no slip, and a contact

angle of 175° . The DP inlet channel was initialized with the DP phase. The model solver was defined as 3D, pressure-based, transient with absolute velocity formulation, non-iterative time advancement, and a first order implicit transient formulation. The pressure velocity coupling was set to fractional step. The spatial discretization was defined by a Least Square Cell Based gradient, a PREssure STaggering Option (PRESTO!) for the pressure, and a second order upwind formulation for the momentum. The Geo-Reconstruct option was used for the volume fraction. All residual tolerances were set to 0.001. The simulations were subsequently iterated with time steps ranging from 1.0 to 5.0 μ s. The time required to complete the simulations on a Desktop PC with an Intel[®] Core™ i7-3770 CPU at 3.40 GHz and 16.0 GB RAM was around 100 h.

3.2.2 On-chip Droplet Generation

In all experiments, the DP was 10% poly (L-lactic acid) (PLLA; Resomer L104, MW 2-3 kDa, Boehringer Ingelheim GmbH, Germany) dissolved in chloroform. The CP was 2% poly (vinyl alcohol) (PVA; MW 13-23 kDa, 87-89% hydrolyzed, Sigma Aldrich) aqueous solution sterile filtered with a 0.22 μ m filter. Both CP and DP were filled into glass syringes and loaded onto syringe pumps (Fusion 400 High Precision Dual syringe Pump and Nanojet XF pump, ChemyxInc., Stafford, TX, USA) and connected to the microfluidic chip using fluorinated ethylene propylene (FEP) tubes with I.D. = 0.5 mm and O.D. = 1.6 mm (IDEX Health and Science, Oak Harbor, WA, USA), and a 4-hole connector (Mitos Edge Connector, Dolomite, Roystone, UK; **Figure 2-2c**). The flow rates were the same as those used in the simulations.

3.2.3 Droplet Size Distribution Analysis

The droplet formation at the orifice of the glass chip was visualized in bright field using an inverted microscope (Motic AE31; Motic Instruments Inc., Richmond, BC, CA) and acquired in

flow by a high speed camera (Miro M4; Vision Research Inc.; Wayne, NJ, USA) at rates up to 7,155 frames per second. Automated custom software (LabVIEW; National Instruments Corporation, Austin, TX, USA) was then used to determine the size distribution of at least 400 droplets per production run.

3.3 Results and Discussion

Our simulations were performed for five different flow rate combinations. At constant DP flow rate, the size of the droplets decreases with increasing CP to DP flow rate ratio. Decreasing both CP and DP flow rate, and at the same time increasing the flow rate ratio leads to the formation of larger particles (**Table 3-1**). This clearly indicates the dependence of the droplet size on both the flow rates of the fluids and their flow rate ratio.

3.3.1 Comparison to the Experimental Microsphere Production

To validate the results from the simulations and determine the accuracy of the model, droplets were generated in a glass microfluidic chip under the operational conditions used for the simulation (**Table 3-1**). The average droplet diameter measured from experimental data agreed well with the results from the 3D simulations (**Table 3-1** and **Figure 3-1**).

The small deviations between 1 and 17% observed between the experimental and simulation results can be attributed to several factors impacting the droplet generation. A main component in our experimental study that has a great impact on size distribution is the accuracy of the syringe pumps used to drive the fluids. As it was discussed in chapter 2, the size of the droplets is greatly influenced by the flow rates of the fluids. Therefore, any fluctuations in the volumetric flow rates the fluids will affect the size of the droplets and in turn affect the size distribution of the droplets in bench-top experiment.

Table 3-1: Simulation results of droplet formation in the microfluidic flow focusing system and comparison of results from simulations with experiments.

Q_{CP} [$\mu\text{L} / \text{min}$]	Q_{DP} [$\mu\text{L} / \text{min}$]	Q_{CP}/Q_{DP}	D [μm]		Difference [%]
			Simulation	Experiment	
20	1	20	90.9	75.5 ± 1.6	16.9
100	1	100	70.6	$65.4 \pm 4.3^{\text{a}}$	7.4
5	0.1	50	94.9	95.5 ± 5.2	0.7
10	0.1	100	90.5	85.5 ± 2.4	5.6
50	0.1	500	69.5	$58.0 \pm 2.5^{\text{a}}$	16.5

^{a)} At these flow rates, higher optical magnification (40x) had to be used to track the generated droplets under a microscope. Due to the limitations of the high speed camera at the higher magnification, the resolution of the captured movies was not sharp enough for the image analyzing software. As a result, the size of the droplets for these experiments was measured manually. Images were captured at high magnification and droplets were sized with ImagePro software. Size distribution was analyzed by Origin 7.

Droplet production was recorded with a high speed camera. For each experiment at least 400 droplets were counted.

Factors contributing to variations or differences in the droplet size in computational studies include assumptions in the physicochemical properties of CP and DP used in the model. In addition, limitations in the mesh used to discretize the flow channel (i.e., size, density) and assumptions on surface properties of the channel walls (i.e., roughness, contact angle) may affect the accuracy of the simulation when compared to experimental results. As Zhou et al. (2010) discussed, 3D interface simulations are difficult to perform, demanding and require larger computational systems. To simplify the method, it was assumed that both CP and DP are Newtonian fluids. Therefore, viscosity was considered to be constant and independent of the shear rate. In addition, the mesh size greatly impacts the accuracy of the model, but also significantly impacts the time required to complete the simulation. In our study the mesh density used was optimized to balance model accuracy with the time required to complete the simulation (i.e., increase in mesh size had negligible impact on the simulated droplet breakup and droplet

size, but significantly increased the time required to complete the analysis). In spite of these simplified assumption, the results from the computational model and the experiment were in good agreement.

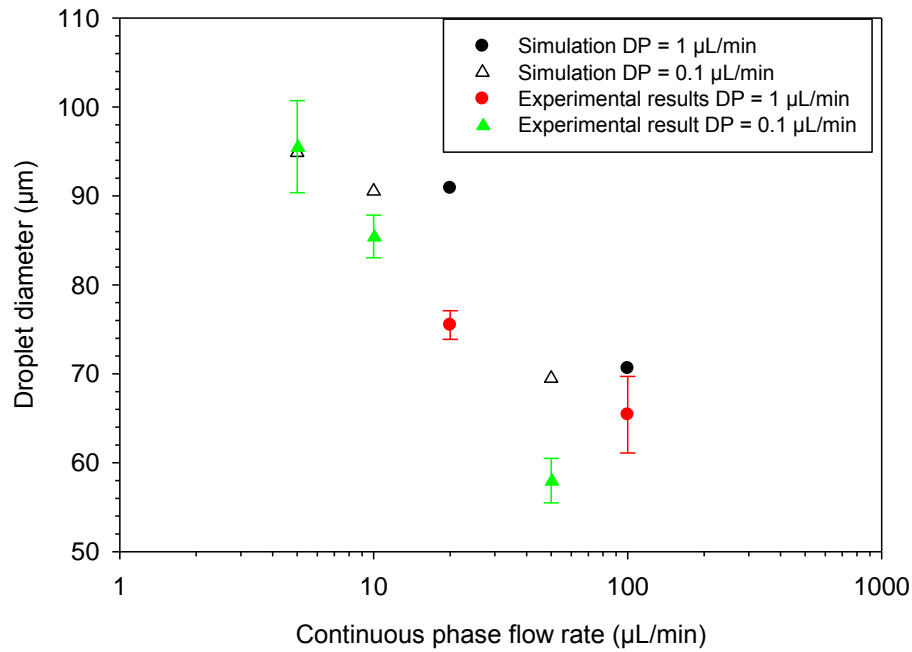


Figure 3-1. Comparison of experimental and simulated droplet generation in the microfluidic chip.

A deviation that was observed between the simulation and experiment was the interaction between the satellite droplets and primary droplets in the chip. In the simulation results, smaller droplets merge with large droplets at some point while this effect was not observed in the experiment. In the experiments, the use of the surfactant PVA in the continuous phase prevents droplet coalescence. The satellite droplets and primary droplets are therefore stabilized and remain as individual droplets

In the simulation, the distinction between two droplets is defined by the distance between the droplets. Larger droplets experience a drag in flow (i.e., due to interactions with the channel

walls), while smaller droplets flow freely and catch up with the parent droplet. The numerical simulation omits surface interactions between droplets due to the presence of surfactants (such as PVA in experimental studies). As a result, the smaller droplets collide with the parent droplet and merge, thereby increasing the parent droplet volume. Addition of surface effect parameters to our simulation increases the level of complexity of the model to a level beyond the scope of our simulation. Our study aimed at investigating the effect of operational conditions on the size of the primary droplets in a microfluidic flow focusing system.

3.3.2 Effect of Flow Rate on Droplet Size

The droplet generation mechanism was further studied by analyzing sequential droplet generation from simulations (**Figure 3-2** to **Figure 3-6**). At low flow rates, $CP < 20 \mu\text{L} / \text{min}$, the DP completely filled the orifice and large droplets that were larger than the size of the orifice formed right at the orifice. By increasing the CP flow rates, the DP extended further into the collecting chamber and the size of the droplets decreased, as was expected from the vast literature on droplet formation by flow focusing [38]. Increased CP flow rates resulted in changing the mechanism of droplet generation from a geometry controlled regime (below a flow rate of $20 \mu\text{L}/\text{min}$) to the jetting condition, as described by Anna and Mayer [38].

To better define the correlation between the flow rates and droplet generation regime, the capillary and Reynolds number for the continuous phase was calculated from **equation 3-1** and **3-2** defined by Anna and Mayer [38].

$$Ca = \frac{\mu_{CP} W_{DP} Q_{CP}}{2\sigma h \Delta Z} \left[\frac{1}{W_{OR}} - \frac{1}{2W_{UP}} \right] \quad 3-1$$

$$Re_{CP} = \frac{\rho_{CP} Q_{CP}}{h \mu_{CP}} \quad 3-2$$

where, μ_{CP} is viscosity of the CP, Q_{CP} is the CP flow rate, σ is the interfacial tension between CP and DP, ρ_{CP} is the CP density, h is the depth of the channels, W_{OR} is the width of the orifice, W_{UP} is the width of the CP channels upstream of the orifice, ΔZ is the distance between the orifice and DP channel, and ' W_{DP} ' is the half-width of the DP channel at the intersection with the CP channel (**Figure 1-11**).

Comparing our finding with Anna and Mayer [38], we found that at CP flow rates less than 20 $\mu\text{L} / \text{min}$ the capillary number and Reynolds number in our simulations were smaller than 0.02 and 2.5 (based on **equations 3-1 and 3-2**), respectively.

The droplets formed under these conditions were larger than the orifice and formed under the geometry-controlled condition (**Figure 3-2, Figure 3-3 and Figure 3-5**). By increasing the flow rates, CP = 50 $\mu\text{L} / \text{min}$, the capillary and Reynolds numbers increase, and the DP extended further through the orifice, leading to a transitional droplet breakup into the dripping condition (**Figure 3-4**). When the CP flow rate increased further to 100 $\mu\text{L} / \text{min}$, a fluid thread formed which eventually broke non-uniformly into small droplets (i.e., transition into jetting condition, see **Figure 3-6**). These results indicate the capability of the model to accurately simulate the droplet generation under different flow and break-up regimes.

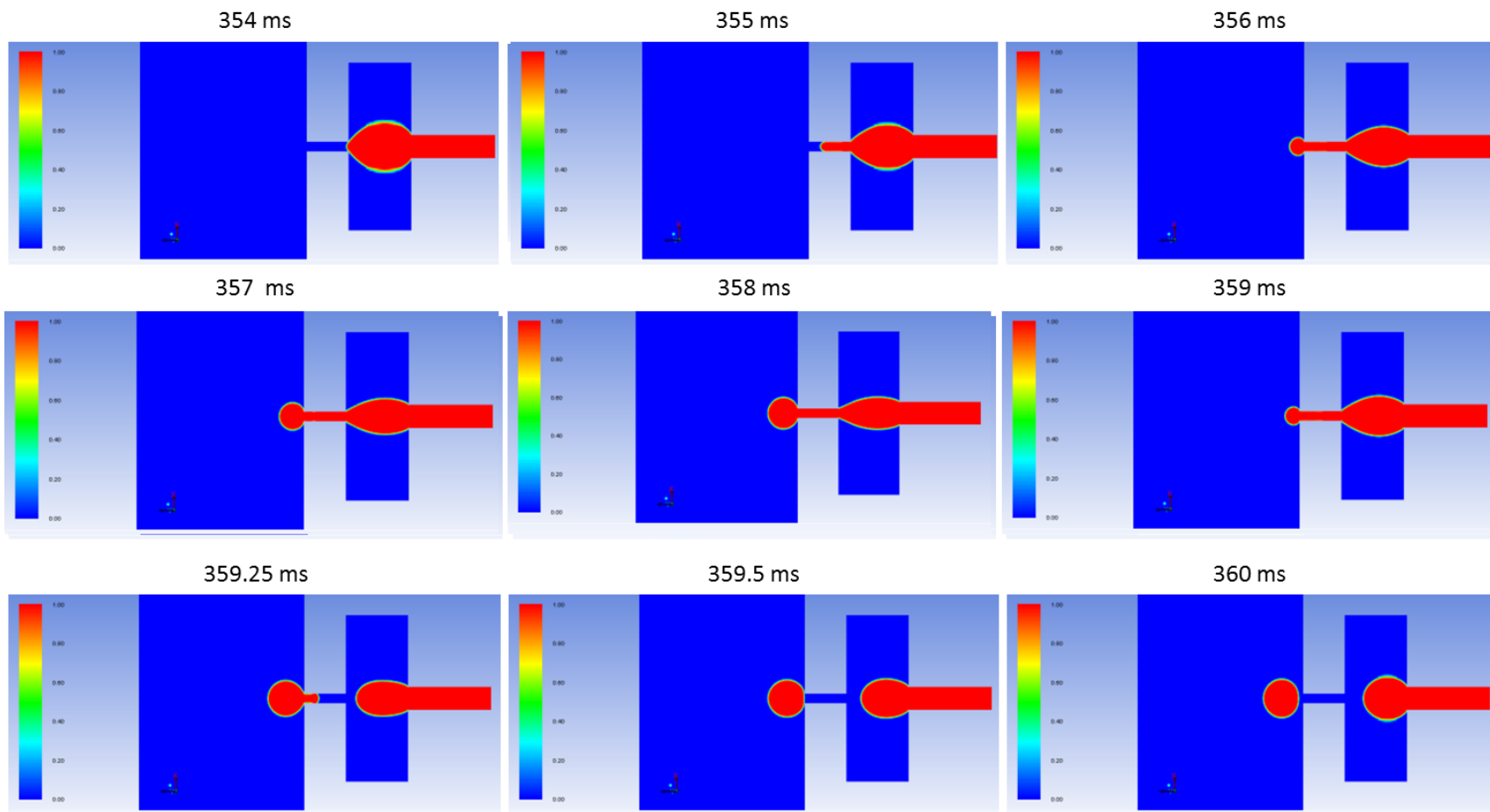


Figure 3-2. 3D simulation of sequential droplet generation in our microfluidic flow focusing system under geometry controlled conditions. Shown are the top-view of the channel with DP shown in red and CP shown in blue (see volume fraction legend). Flow rates used in the simulation were: $Q_{CP} = 5 \mu\text{L} / \text{min}$, $Q_{DP} = 0.1 \mu\text{L} / \text{min}$.

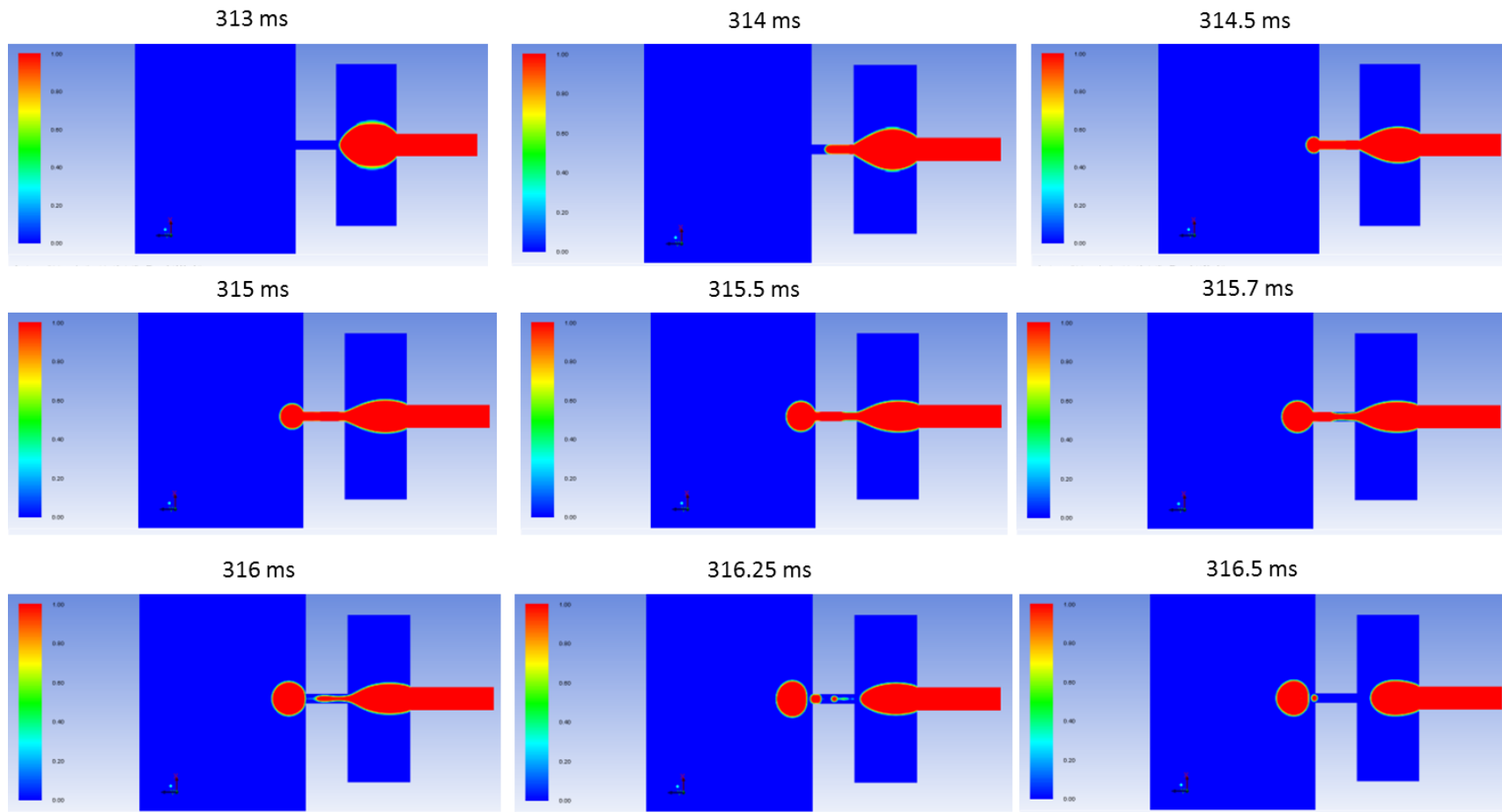


Figure 3-3. 3D simulation of sequential droplet generation in our microfluidic flow focusing system under geometry controlled conditions. Shown are the top-view of the channel with DP shown in red and CP shown in blue (see volume fraction legend). Flow rates used in the simulation were: $Q_{CP} = 10 \mu\text{L} / \text{min}$, $Q_{DP} = 0.1 \mu\text{L} / \text{min}$.

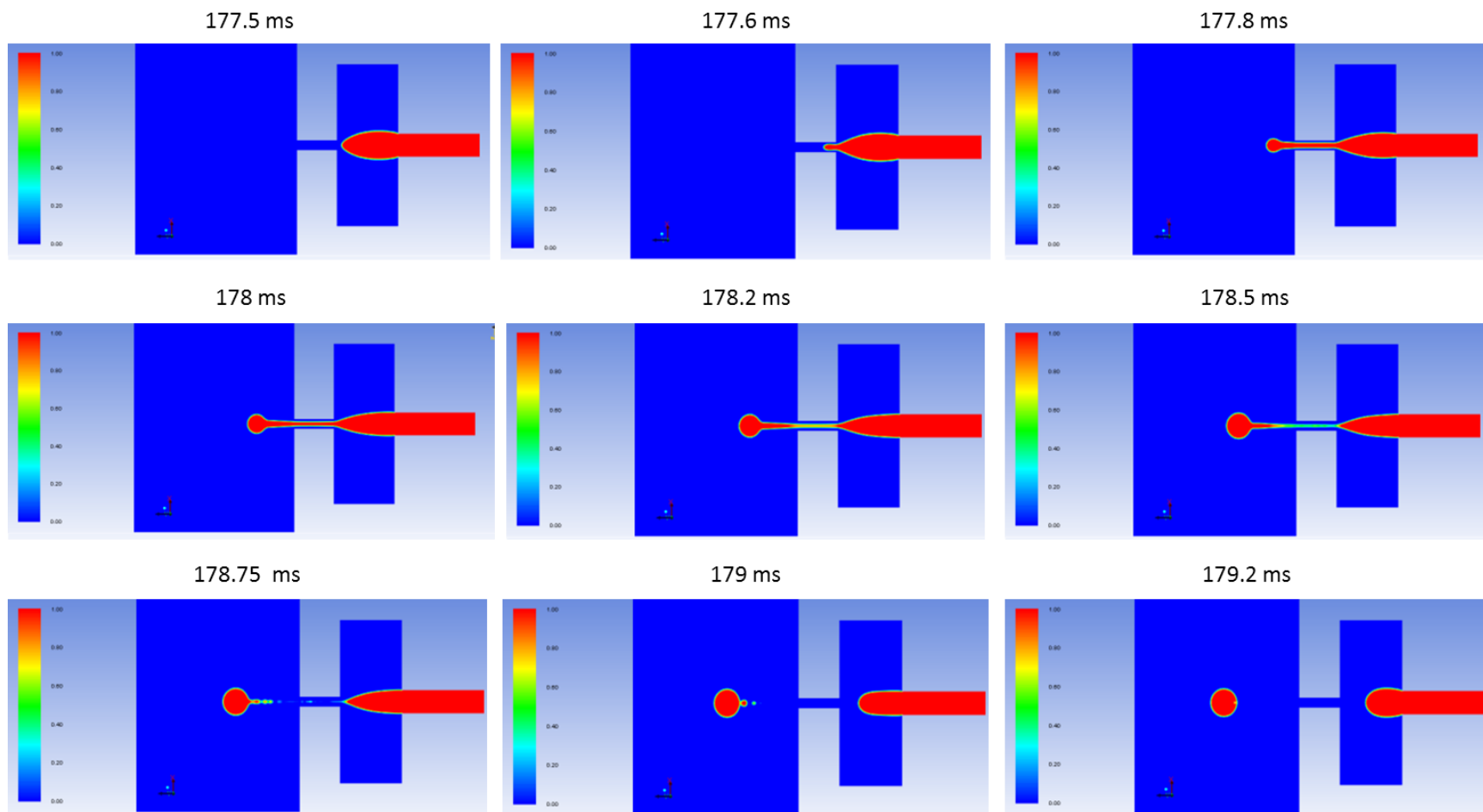


Figure 3-4. 3D simulation of sequential droplet generation in our microfluidic flow focusing system. Droplet generation is in transition to dripping regime. Shown are the top-view of the channel with DP shown in red and CP shown in blue (see volume fraction legend). Flow rates used in the simulation were: $Q_{CP} = 50 \mu\text{L} / \text{min}$, $Q_{DP} = 0.1 \mu\text{L} / \text{min}$.

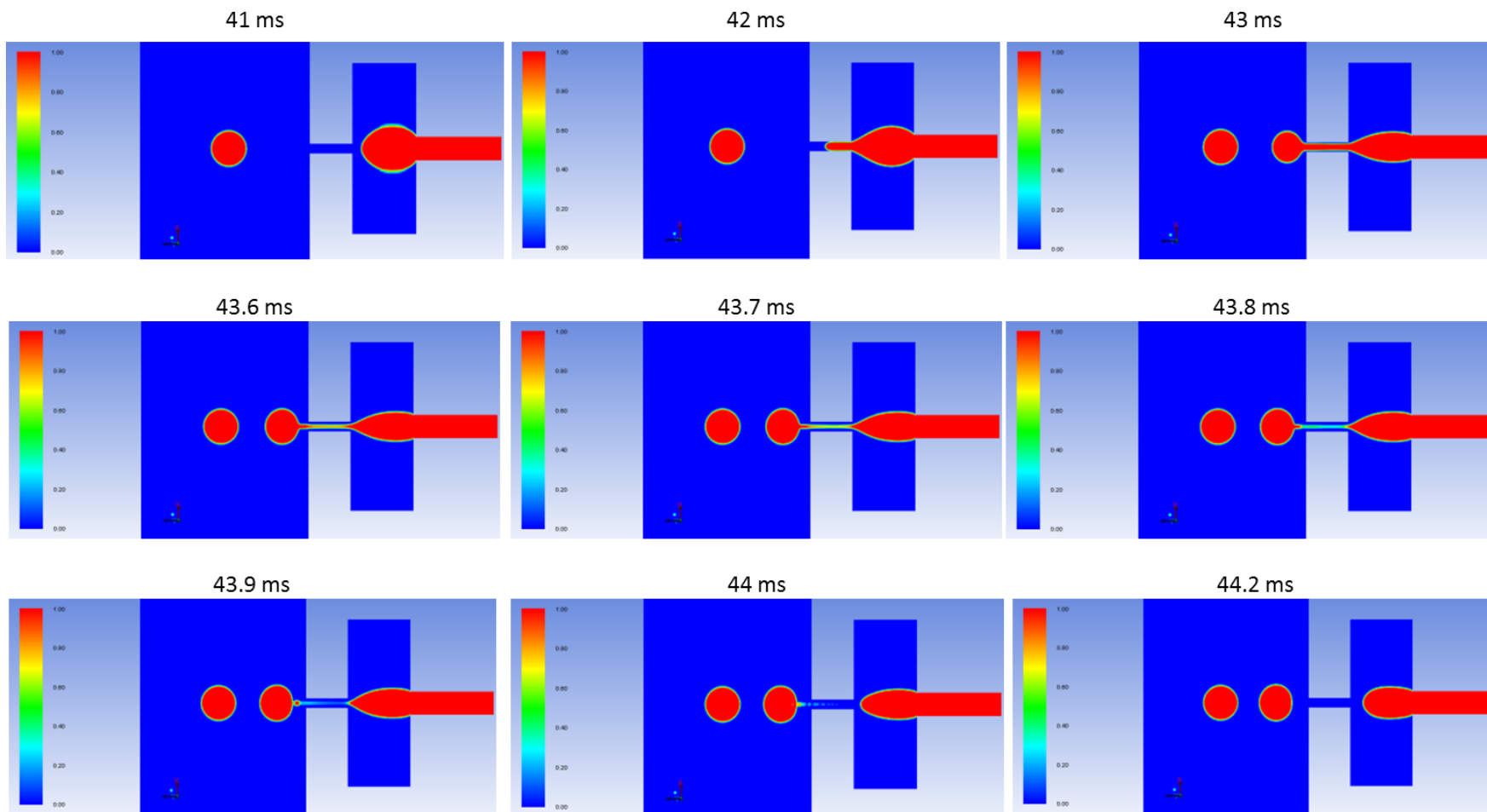


Figure 3-5. 3D simulation of the sequential droplet generation in our microfluidic flow focusing system under geometry controlled conditions. Shown are the top-view of the channel with DP shown in red and CP shown in blue (see volume fraction legend). Flow rates used in the simulation were: $Q_{CP} = 20 \mu\text{L} / \text{min}$, $Q_{DP} = 1 \mu\text{L} / \text{min}$.

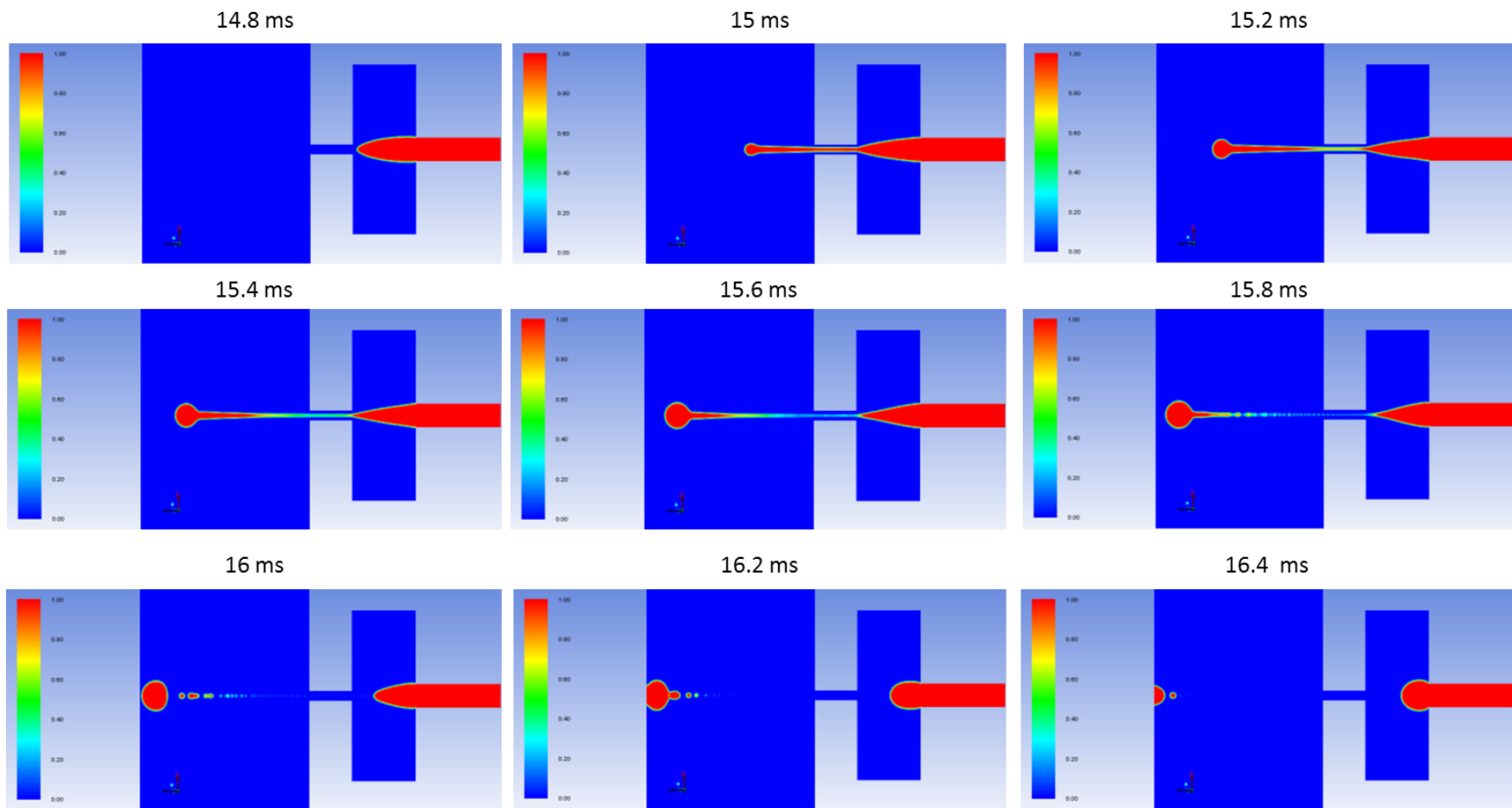


Figure 3-6. 3D simulation of the sequential droplet generation in our microfluidic flow focusing in a transition to jetting condition. Shown are the top-view of the channel with DP shown in red and CP shown in blue (see volume fraction legend). Flow rates used in the simulation were: $Q_{CP} = 100 \mu\text{L} / \text{min}$, $Q_{DP} = 1 \mu\text{L} / \text{min}$.

3.4 Conclusions

The droplet generation in our microfluidic flow focusing system was successfully simulated. The simulation results showed a similar reduction in the size of the droplets by increasing the CP flow rate as in our experiments and published experimental results of other research groups. The 3D computational model of the droplet generation in a microfluidic flow focusing system was robust and reliable for the prediction of the droplet size. The validation experiments showed deviations of less than 17% between the experiments and simulation at all conditions, and sometimes even only 1%.

In future work, the model will be valuable to computationally optimize parameters for the production of monodispersed particles (e.g., chip design, viscosity of the fluids, interfacial tension between the fluids), and save significant amounts of time and money during the fine-tuning of the microsphere preparation.

Chapter 4: Encapsulation of Magnetic Nanoparticles in Polymer

Microspheres Using the Microfluidic Flow Focusing System

4.1 Introduction

The efficacy of a given drug therapy is associated with its ability to concentrate or localize the drug in a targeted organ. Many tools and techniques have been developed to increase drug localization including direct injection, use of catheter, surface coating of the nano- or microcarriers with peptides, antibodies, or sugars, chemical modification of the drug, ultrasound or magnetic field assisted drug delivery. The last method, magnetic drug targeting, is an effective non-invasive method that uses magnetic particles as drug carriers to accumulate the therapeutic agent in a magnetically guided fashion at the site of action [84-86]. It employs the magnetic field of an external magnet, such as Stereotaxis' magnetic navigation system [87,88] or Halbach arrays [89], or an internal magnet, such as magnetizable wires [90] or magnetizable stents [91] to control the movement of the magnetic carriers inside the body.

Magnetic particles generate heat under the influence of an alternative magnetic field due to the physical rotation of particles (Brownian relaxation) and constant directional changes in their magnetic moment (Néel relaxation) [92,93]. The application of heat generating magnetic particles dates back to 1956 when Gilchrist increased the temperature in lymph nodes by directly injecting maghemite magnetic particles into them [94,95]. A few years later, in 1963, Meyers showed that iron magnetic particles can be directed to the site of action, the leg muscles in this case, with an externally applied magnetic field after intravenous injection of small iron particles [96].

Using well defined magnetic particles for the treatment of cancer was first introduced by Kato *et al.* [97] and Widder *et al.* [98] more than three decades ago. Widder *et al.* made 1 μm

albumin microspheres loaded with iron oxide magnetic nanoparticles to increase the drug concentration in a subcutaneous tumor located in the tail of rats [98], while Kato *et al.* prepared large magnetic microspheres that increased the drug concentration in the urinary bladder of rabbits after magnetic targeting [97]. In 1993, Jordan *et al.* showed that magnetic nanoparticles (MNPs) in an alternating magnetic field can produce significantly more heat than what was up to then known from larger magnetic microparticles (1 – 100 μm) and employed the effect for thermal ablation of cancer cells [99]. This method is now known as magnetic hyperthermia.

To obtain the desired temperature required for cell damage leading to cell death ($> 42\text{ }^\circ\text{C}$), a high concentration of magnetic nanoparticles is required in the target area (typically 10 to 100 mg of particles per cm^3 of tumor tissue depending on the thermal properties of the particles) [100,101]. The intravenous administration of such a high concentration of MNPs is likely to cause severe side effects due to the difficult to control distribution of the MNPs inside the body and potentially associated toxicity and immunogenicity. One approach of preventing such side effects is to encapsulate the MNPs into larger structures such as polymeric microspheres, which can then be guided and concentrated into target organ(s) much more efficiently. In addition, the resulting magnetic microspheres can be loaded with therapeutic agents (e.g., anticancer agents, chemosensitizers) that are released from the particles over an extended period of time and would enhance the hyperthermia treatment.

In the previous chapters the production of polymer microspheres in a novel custom designed microfluidic flow focusing system was explained and operational conditions for the production of monosized PLLA microspheres were determined. In this chapter, we investigate the feasibility of producing magnetic microspheres in the microfluidic flow focusing system and determine the optimal condition for the production of monosized magnetic microspheres.

4.2 Material and Methods

4.2.1 Magnetic Nanoparticles

Magnetic nanoparticles used in these experiments were magnetite nanoparticles (Fe_3O_4) coated with polyethylene oxide nitrodopamine (PEO-nitroDOPA). The particles provided by Dr. Thompson Mefford, Clemson University, Clemson, SC, USA were received in dichloromethane. For the following experiments, the MNPs were initially dried under vacuum and then mixed with the polymer and dissolved in chloroform.

4.2.2 Magnetic Microsphere Production

The magnetic microsphere production method in the microfluidic flow focusing system was the same as explained in section 2.2 but with an altered disperse phase. To produce magnetic microspheres, the DP was prepared from dried magnetic nanoparticles suspended in PLLA solution. Specifically, 9.58 mg of dried MNPs was mixed with 20 mg of PLLA, dissolved in 250 μL of chloroform and filled into a 0.5 mL glass syringe.

4.2.3 Microsphere Size Distribution Analysis

The size analysis of the microspheres was done after completion of the solvent evaporation. The particles were resuspended in distilled water and an *aliquot* imaged under an inverted microscope (Motic AE31). ImagePro software was used to analyze the size of each microsphere. The size distribution of microspheres based both on volume and number were determined using Origin 7 (OriginLab, Northampton, MA, USA) using at least 200 particles for each analysis. The polydispersity of the particles was determined by calculating the coefficient of variation (CV) as

$$\text{CV (\%)} = \left(\frac{\sigma}{D_p} \right) \times 100 \quad 4-1$$

where D_p is the average size of the particles and σ is the standard deviation of the particle size.

4.2.4 Scanning Electron Microscopy

The surface morphology of polymer microspheres was examined by Scanning Electron Microscopy (SEM; Hitachi S-4700, Tokyo, Japan). A droplet of aqueous microsphere suspension was placed on an aluminum stub covered with carbon adhesive, air dried and subsequently coated with 5 nm of gold/palladium under reduced pressure (<5 Pa) using a JFC-1600 fine coater (JEOL, Tokyo, Japan). The samples were imaged at 2 keV.

4.2.5 Thermal Property Measurement

Thermal properties of the magnetic microsphere suspensions were measured in alternating magnetic fields of 14 and 24.6 kA/m at 400 kHz and the specific absorption rate (SAR) was calculated from the measured heating curves as described before [102]. The temperature within the particles was measured during magnetic heating by means of a fiber optic temperature sensor (FOTEMP, Optocon, Germany). Obtained SARs were normalized to the amount of magnetic microspheres within the fluid to estimate their heating performance as well as to the total amount of magnetic nanoparticles in the sample to estimate heating performance of the incorporated MNP. Since the size of magnetic microspheres was too large to cause a particle rotation during alternating field exposure, Brownian relaxation could be excluded and magnetic losses were entirely attributed to Néel relaxation or hysteresis losses.

4.3 Results and Discussion

4.3.1 Selection of Magnetic Nanoparticles

Iron oxide (Fe_3O_4) nanoparticles are the most commonly used magnetic nanomaterials for biomedical application due to their low cytotoxicity, approval by FDA, and superparamagnetic properties [103]. Iron oxide nanoparticles are synthesized through co-precipitation of Fe^{2+} and Fe^{3+} . The uncoated produced particles are susceptible to oxidation and they also agglomerate and

form large clusters in physiological pH [104] that would affect response in magnetic field [105]. Coating of MNPs not only prevents particle aggregation but also enhance particle interaction with cells and can be used as attachment or linking site between drug molecules and MNPs [105,106].

Suitable magnetic nanoparticles for our application must be stable in organic solvents for successful encapsulation in polymer microspheres and highly stable in PBS to be able to use them effectively in biological media. The formation of a uniform and stable chloroform-MNP suspension is crucial for the encapsulation method that we use. In our process set up, the polymer-MNP suspension is injected into the microchip very slowly, therefore, phase separation will affect the microparticle production process and uniformity of the particles produced. As it was explained in chapter 1 and 2, the monodispersity of the particles produced in microfluidic flow focusing system is associated with the physicochemical properties of the fluids used in the system. Gradual separation of MNPs from the rest of the polymer solution changes the physicochemical properties of the dispersed phase and hence it affects the size distribution of the particles produced. Moreover, phase separation affects the uniform distribution of MNPs in the solution and in the produced microspheres

The particles stability in PBS is related to our future application when the MNPs will be mixed with protein solution and co-encapsulated in PLLA microspheres. Particles used in biological media or PBS must have a well-anchored coating that prevents their rapid replacement with media components. Different polymers have been used to coat MNPs such as dextran, chitosan, PEI, PEG, and phospholipids [106]. Recent research has shown that catechol-derived materials have great affinity toward magnetite and they bind firmly to the surface of iron oxide magnetic nanoparticles [105,107]. Amsted *et al.* has shown that nitrated 3,4 dihydroxy-L-phenylalanine

(nitroDOPA), a catecholamine, forms very stable coatings on magnetic nanoparticles in the biological environment and in PBS [108]. The PEG-nitroDOPA coated magnetic nanoparticles synthesized in Dr. Mefford group were both stable in biological media [105] and remained suspended in chloroform for many hours, so they were chosen for our encapsulation experiments.

4.3.2 Magnetic Microsphere Production

The addition of magnetic nanoparticles (MNPs) to the dispersed phase changed the physicochemical properties of the fluid and consequently affected the droplet formation. To determine appropriate flow rates for the production of monodispersed magnetic microspheres, additional optimization experiments were necessary. We observed irregular interruptions in the DP flow rates and droplet generation when the CP flow rate exceeded 60 $\mu\text{L}/\text{min}$. At flow rates higher than 60 $\mu\text{L}/\text{min}$, initially, droplet generation was hindered and a long thread of DP was formed after the orifice. Further increase of the CP flow rate, completely blocked the flow of DP and no droplets or thread was formed in the collecting chamber. Therefore, the CP flow rate was limited to 60 $\mu\text{L}/\text{min}$. The flow rate combinations used for optimization process can be seen in **Table 4-1** and the size distribution and optical microscopic images of magnetic microspheres produced at different flow rates are shown in **Figure 4-1** to **Figure 4-4**. Quasi-monodispersed particles were only produced at a flow rate of 60 $\mu\text{L}/\text{min}$ (**Figure 4-4**).

Further analysis of the particle size distribution of magnetic microspheres showed that the percentage of satellite droplets was generally lower in the experiments with magnetic microspheres compared to experiments with non-magnetic microspheres. Addition of MNPs to the polymer solution changed the rheological properties of the fluid, especially the viscosity.

MNPs have a tendency to agglomerate due to van der Waals forces and electrostatic interactions between individual particles.

Table 4-1. Size distribution of the PLLA microsphere loaded with iron oxide magnetic nanoparticles. In all experiments, the continuous phase was 2% PVA in water and the dispersed phase 20 mg PLLA and 9.58 mg of MNPs in 250 μL of chloroform.

Q_{CP} [$\mu\text{L}/\text{min}$]	Q_{DP} [$\mu\text{L}/\text{min}$]	D_v [μm]	D_n [μm]	CV_v [%]	CV_n [%]
30	0.3	33.63 \pm 7.60	31.66 \pm 5.42	22.6	17.12
40	0.3	25.89 \pm 5.51	24.06 \pm 3.77	21.27	15.67
60	0.3	25.55 \pm 4.58	22.35 \pm 3.82	18.65	17.09
30	1	41.01 \pm 20.65	31.62 \pm 12.15	50.35	38.42
40	1	42.11 \pm 7.63	38.98 \pm 7.12	18.12	18.27
60	1	29.11 \pm 3.36	28.37 \pm 3.5	11.53	12.34

Q = flow rate; D_v , D_n = volume and number based mean diameter; CV_v , CV_n = volume and number based coefficient of variation

The formation of agglomerates increases the viscosity of the dispersed phase [109,110]. In addition, suspension fluids with solid particles concentration higher than 40% (v/v) have a non-Newtonian behavior. At low shear rate, they are shear thinning followed by a Newtonian behavior as the shear rate increases, and at higher shear rate, they behave like a shear-thickening fluid. In general, relative viscosity of suspension correlates with reduced volume fraction of solid particles and the viscosity approaches to infinity as the reduced volume fraction approach to one. To determine the exact behavior in the range of the shear rates used in our experiments, several tests were required which was not possible due to the limitation of sample quantity. We speculate that overall rheological changes occur in the DP phase led to an increase in the viscosity of the fluids and reduction in the number of satellite droplets formed. Similar effects were observed earlier by Derzsi *et al.* (2013) that number of satellite droplet will reduce when the viscosity ratio of DP to CP increases, and was discussed in chapter 2.

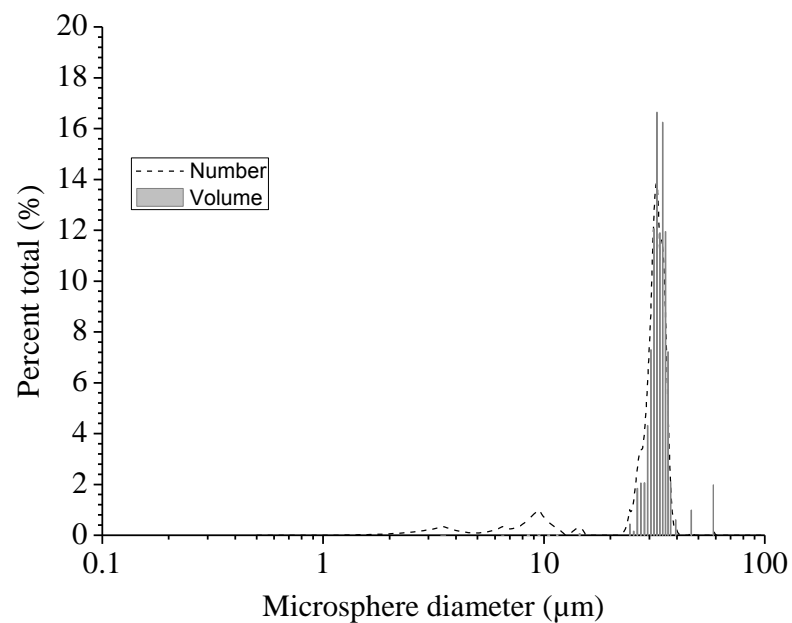
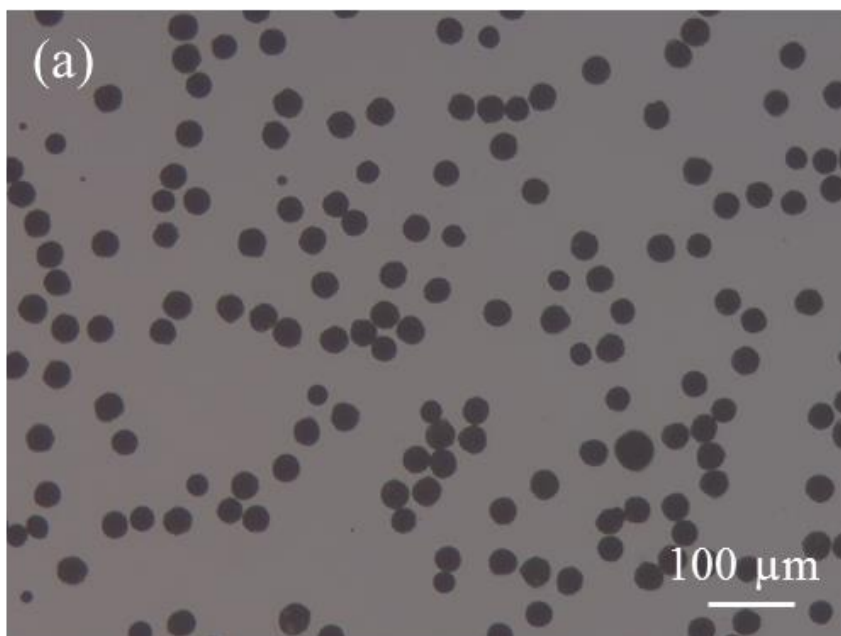


Figure 4-1: Size distribution analysis and microscopic images of the magnetic microspheres produced in a glass microfluidic flow focusing system at CP = 30 $\mu\text{L}/\text{min}$ and DP = 0.3 $\mu\text{L}/\text{min}$. Continuous phase was 2% PVA dissolved in water and dispersed phase was 20 mg PLLA and 9.58 mg MNPs dissolved in 250 μL chloroform.

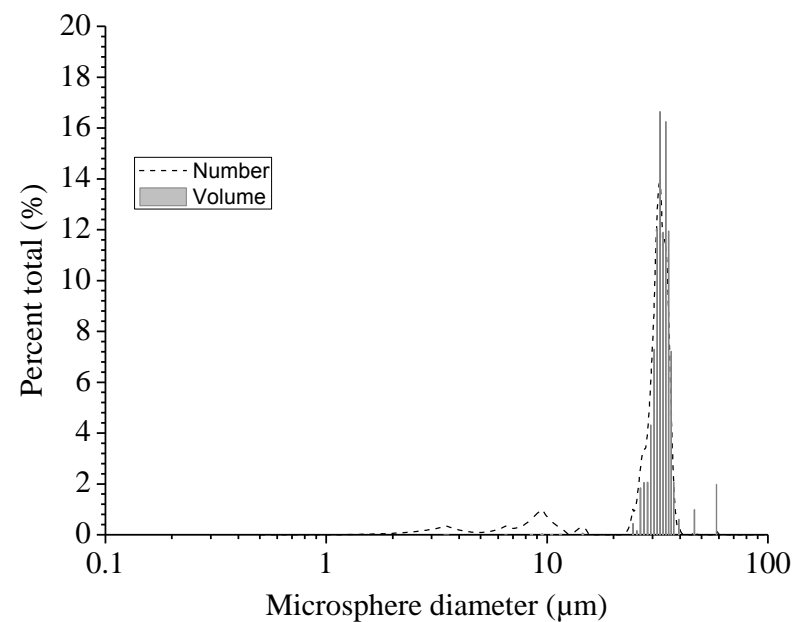
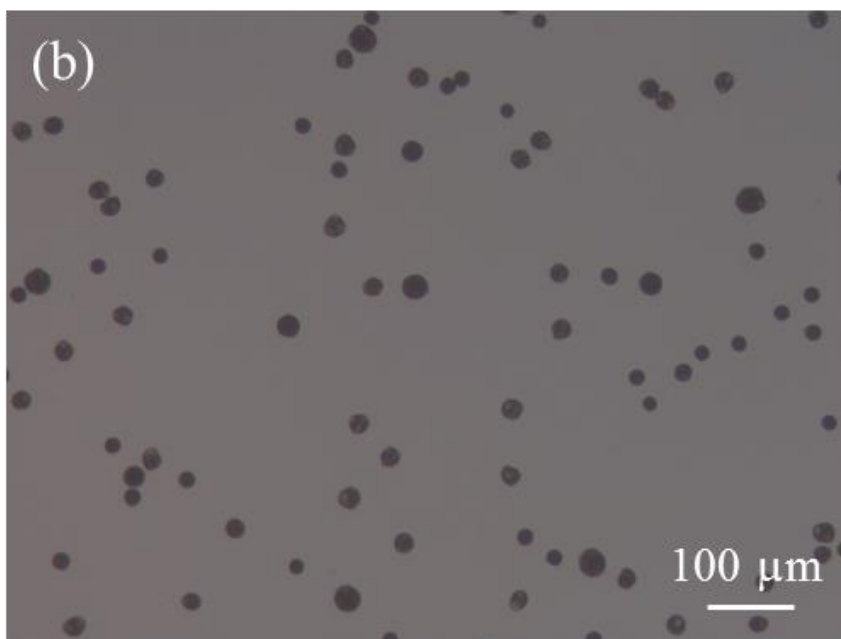


Figure 4-2: Size distribution analysis and microscopic images of the magnetic microspheres produced in a glass microfluidic flow focusing system at CP = 60 $\mu\text{L}/\text{min}$ and DP = 0.3 $\mu\text{L}/\text{min}$. Continuous phase was 2% PVA dissolved in water and dispersed phase was 20 mg PLLA and 9.58 mg MNPs dissolved in 250 μL chloroform.

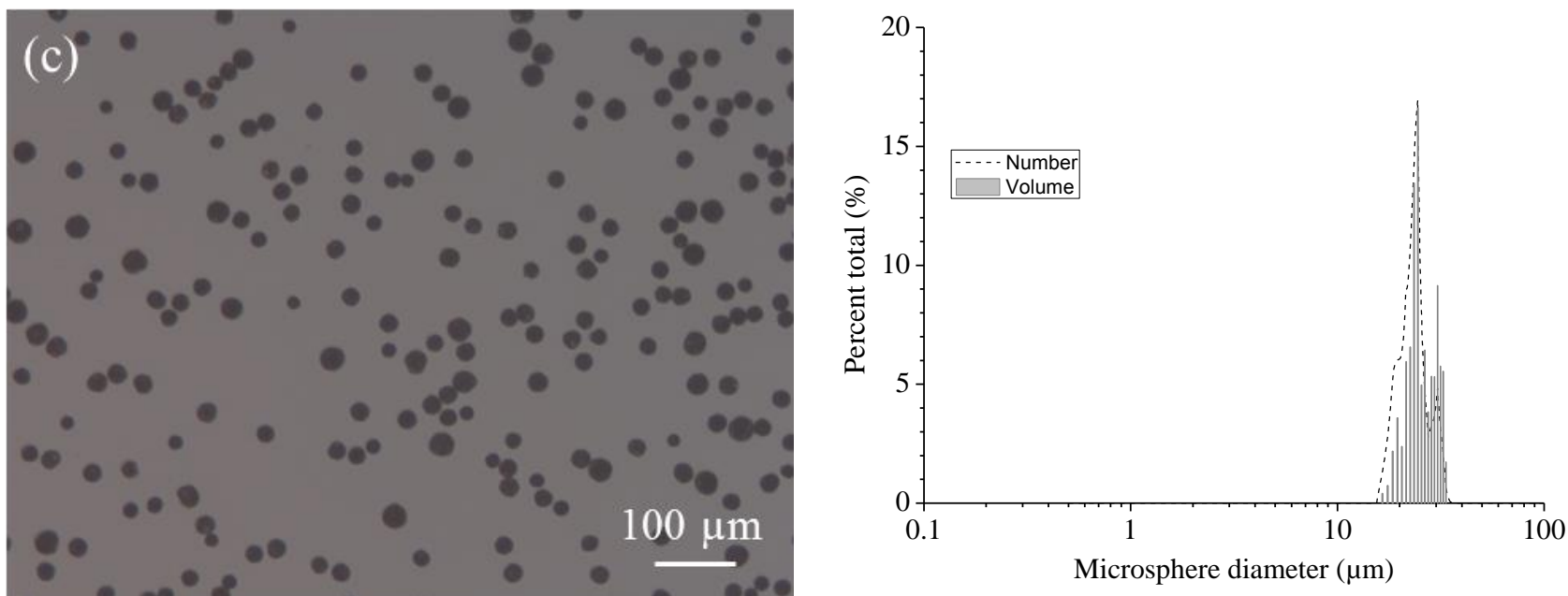


Figure 4-3: Size distribution analysis and microscopic images of the magnetic microspheres produced in a glass microfluidic flow focusing system at CP =40 $\mu\text{L}/\text{min}$ and DP = 0.3 $\mu\text{L}/\text{min}$. Continuous phase was 2% PVA dissolved in water and dispersed phase was 20 mg PLLA and 9.58 mg MNPs dissolved in 250 μL chloroform.

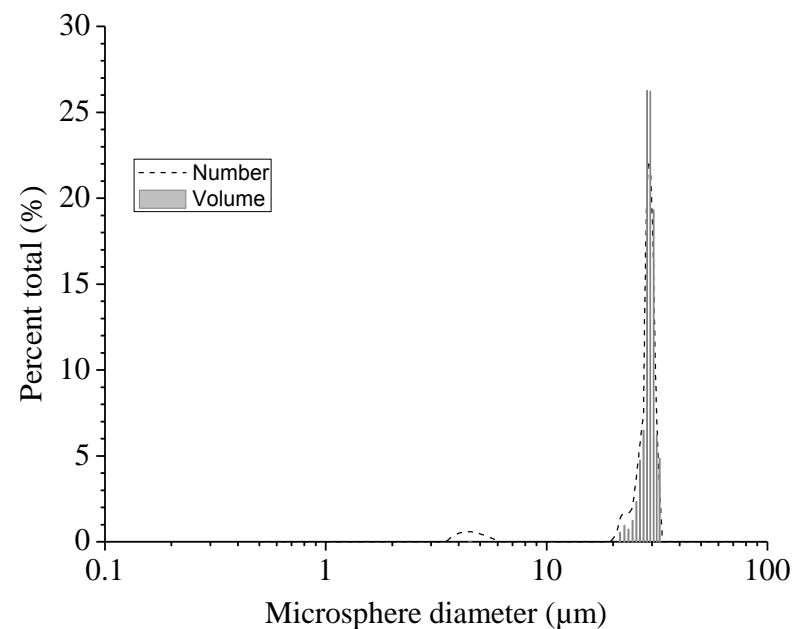
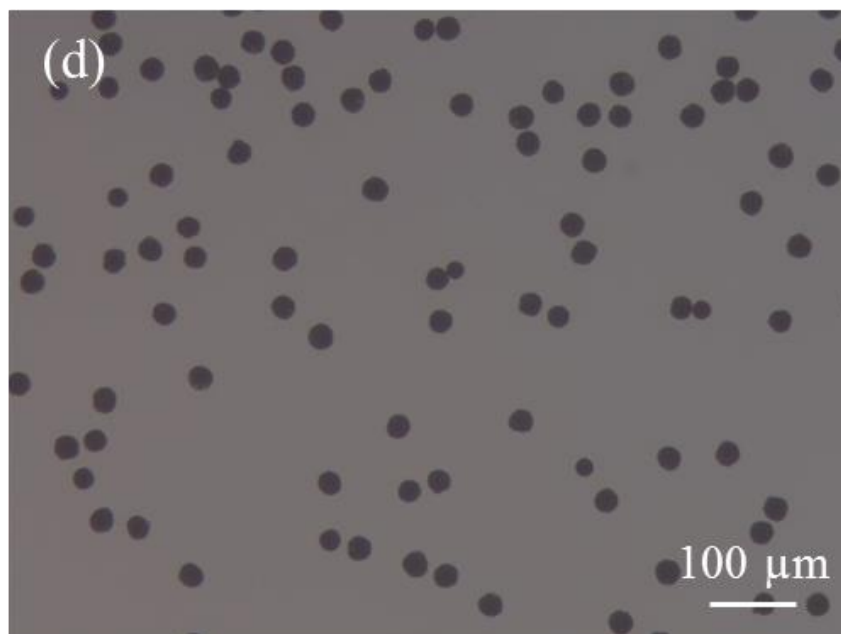


Figure 4-4: Size distribution analysis and microscopic images of the magnetic microspheres produced in a glass microfluidic flow focusing system at CP = 60 $\mu\text{L}/\text{min}$ and DP = 1 $\mu\text{L}/\text{min}$. Continuous phase was 2% PVA dissolved in water and dispersed phase was 20 mg PLLA and 9.58 mg MNPs dissolved in 250 μL chloroform.

Monosized magnetic microspheres such as the ones generated in our flow focusing chip are optimal, as it was discussed in section 4.1, for the predictable induction of heat in an alternating magnetic field (magnetic hyperthermia) or for the precise heat-inducible drug release when a thermosensitive polymer is used in the formulation. For both applications, or combinations thereof, magnetite loaded microspheres must be transferred to the site of action where they are immobilized, generate heat under the influence of an external magnetic field, and damage (cancer) cells, enhance drug release or increase malignant cell sensitivity to the encapsulated therapeutic agents in the microspheres. Different mechanisms of heat generation have been identified in magnetic nanoparticles under the influence of an external magnetic field. The details of these mechanisms are beyond the scope of this thesis, but are discussed comprehensively by Dutz and Hergt (2014).

The fabricated MMS were found to be superparamagnetic (**Figure 4-5**). They will therefore lose their magnetic properties after removal of the external magnetic field. To predict the usefulness of the particles for magnetic hyperthermia or heat induced drug release system, their specific absorption rate (SAR), which is the particles' heat generation capability, was determined at a constant frequency of 400 kHz and two different amplitudes. At low amplitudes, the changes in the SAR were only minimally dependent on the size of the magnetic microspheres (MMS). By normalizing SAR to the concentration of MNPs encapsulated, it can be seen that at both amplitudes, there is a high dependency on the SAR of MMS to their MNPs concentration (**Table 4-2**).

The heating power of our particles makes them suitable for hyperthermia treatment of the tumor size 5 mm or larger [100]. Temperature elevation in a tumor is due to a balance between heat generation capacity of the heating source and heat loss from the tumor. Heat generation

capacity is a characteristic property of MNPs and is fixed for each particle. Heat loss from the tumor is affected by the ratio of surface area to volume of the tumor [111].

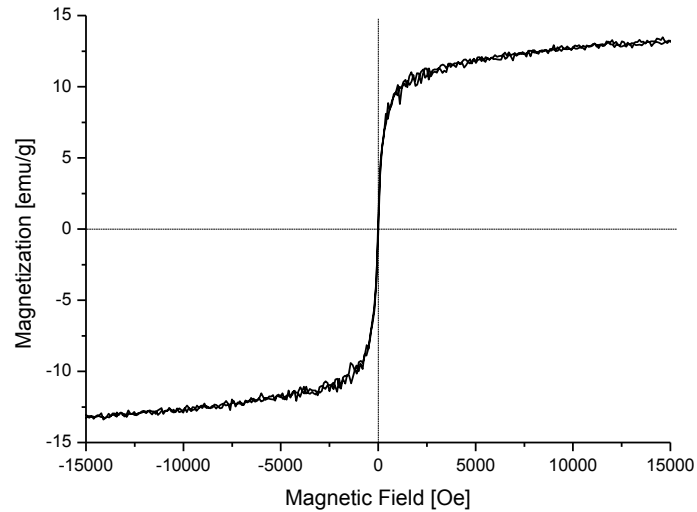


Figure 4-5 : Hysteresis curve of dry MMS confirms their superparamagnetic behavior as well as a magnetic concentration of about 20% by mass.

Therefore, as the size of the tumor decreases the surface area to volume ratio increases and consequently, amount of heat lost increases. As a result, smaller tumors require MNPs with substantially higher specific heating power, minimum 500 W/g [100,111]. The correlation between the SAR of the particles required for hyperthermia and cell thermoablation (irreversible damage to cells due to high temperature) and the tumor size has been studied by several groups [100,111,112].

Instead of changing the heating power of the MNPs, another approach to increase the heat generating capacity of the magnetic microspheres is to increase the concentration of MNPs in the polymer microspheres to 50% or higher that will linearly increase the total amount of heat dissipated from the particles This magnetite concentration in PLA microspheres has been

reached before [113]. However, further improvements in the biocompatibility of the then-used magnetic nanoparticle coating (ferrofluid W-40, Taiho Industries Co. Ltd., Japan) are necessary, as the resulting magnetic microspheres showed hemolytic activity at higher concentrations.

Table 4-2. Magnetic and thermal properties of PLLA magnetic microspheres (MMS).

Diameter of MMS (μm)	31.66\pm5.42	28.37\pm3.50	24.06\pm3.77
Saturation magnetization [emu / g]	13.1	12.0	11.1
MNP content [% by mass]	18.7	17.1	15.8
Coercivity [Oe]	9.9	4.0	12.5
SAR [W / g (MMS)]			
@ 14 kA/m, 400 kHz	20.9	18.8	16.6
@ 24.6 kA/m, 400 kHz	37.0	29.0	32.1
SAR [W / g (MNP)]			
@ 14 kA/m, 400 kHz	111.5	109.5	103.2
@ 24.6 kA/m, 400 kHz	197.5	169.0	202.6

Future applications for the produced microspheres are their use in combination therapies such as thermal/chemotherapy or thermal/radiotherapy with targetability properties. The immobilization of chemotherapeutic drugs or therapeutic radioisotopes along with MNPs into monosized microspheres (i) reduces the drugs' blood concentration and enhances the availability of the drug locally over extended periods, and (ii) reduces the cytotoxicity to non-target organs and the monophagocytic system. The thermal properties of the particles can additionally be used as a tool to increase potency of the chemo or radio therapy.

4.3.3 Morphology of the Magnetic Microspheres

The addition of MNPs caused morphological changes in the particle matrix and introduced pores and uneven surfaces (**Figure 4-6**) in contrast to poly (lactic acid) and poly(lactic-co-glycolic acid) microparticles which generally have a smooth surface as described in chapter 2.

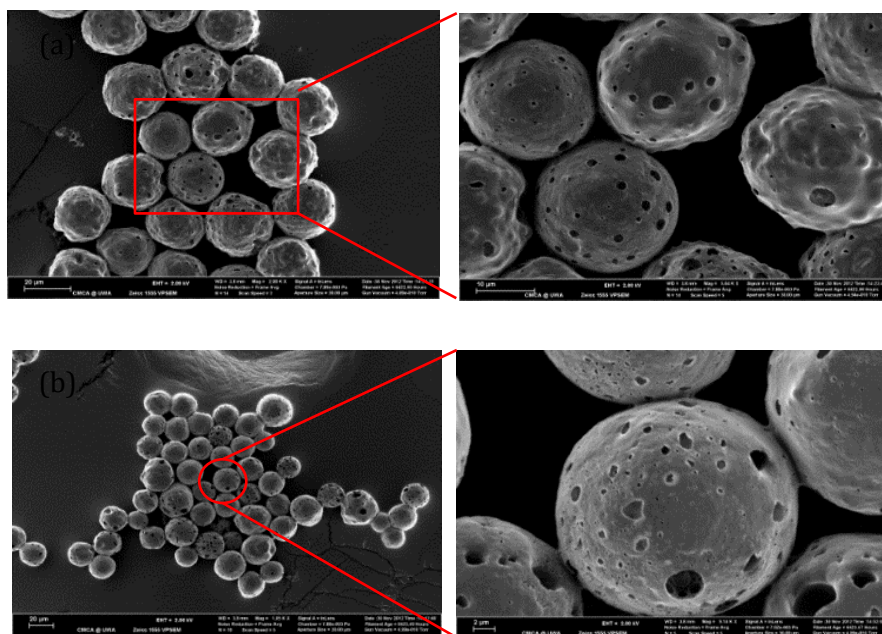


Figure 4-6. Scanning electron microscopy images of PLLA microspheres. Continuous phase was 2% PVA in water and disperse phase was 20 mg PLLA and 9.8 mg MNPs in 250 μ L chloroform. The particles were produced at (a) CP = 60 μ L/min and DP = 1 μ L/min and (b) CP = 40 μ L/min and DP = 0.3 μ L/min.

Poly(lactic acid) and poly(lactic-co-glycolic acid) microspheres produced by the emulsification method have generally smooth surfaces [66,69]. Many potential reasons have been identified that might cause formation of holes on the surface of magnetic PLLA microspheres.

The most likely cause of pores formation on the surface of our magnetic microspheres is the formation of jammed nanoparticles on the surface of the microspheres. During the solvent evaporation, the size of the droplets decreases and MNPs come closer together, jam and form a relatively stable hard layer on the surface of the particles. This increases the internal pressure of the droplet. Eventually, the outward pressure of the solvent trapped inside the particles breaks through the MNP layer and causes holes on the surface of the particles that become the large visible pores [114,115]. Further investigations will be required to determine the origin of the differences in the particle surface, but they are beyond the scope of our study.

Another potential reason for the pore formation is the mechanism and rate of solvent removal from the generated droplets, a theory that is mainly discussed in the literature [68]. The pore formation on the surface of our particles might, however, not stem from this, as the mechanism of solvent removal was the same here as it was for non-magnetic PLLA microspheres shown in chapter 2 where no pores were observed

Two other reasons for pore formation are drug release during solidification [116] and addition of solid drugs to the fluid mixture during emulsification [66] when particles are loaded with drugs. The nanoparticles added to the mixture might behave like drugs and cause the formation of pores on the surface due to one or a combination of these two mechanisms. A definitive reason for the hole formation is, however, not clear and will require further investigations.

4.4 Conclusions

Our microfluidic flow focusing system was for the first time able to produce quasi-monodispersed magnetic microspheres, which means particles with a coefficient of variation of less than 16%. Scanning electron microscopy image of the particles showed spherical microspheres with pores on their surface.

The addition of MNPs to the DP reduced the number of satellite droplets formed in the flow focusing system (compared to the nonmagnetic droplet generation, see chapter 2). The observed changes might be due to an increase in the viscosity of the DP. The higher DP to CP viscosity ratio in viscoelastic fluids causes a reduction in the number of satellite droplets as shown for example by Derzsi *et al.* [54].

The thermal heating power of the generated magnetic microspheres, at 37 W/g of microspheres, indicates that these microspheres are useful for magnetic hyperthermia and thermal cell ablation of large size tumors. By increasing the concentration of magnetic

nanoparticles to 50%, which is achievable [113], or by using magnetic nanoparticles with a minimum specific absorption rate of 500 W/g, which have been described in the literature [100], smaller tumors could also be treated.

Chapter 5: Encapsulation of Protein in Polymer Microspheres using a Microfluidic System

5.1 Introduction

Maintaining a therapeutic drug concentration in the blood stream or tissue is the basis of drug therapy and is the crucial factor to be considered in drug formulation and determining drug dosage. A therapeutic drug concentration can be achieved by multiple drug administration at predefined intervals, which is the conventional method that has been practiced for a long time, or by a single administration of a long lasting drug formulation, i.e., controlled release. The latter is a more recent approach that is more convenient for the patient and health care providers as it will reduce the frequency of drug administration. In controlled release formulation, a relatively constant drug concentration is achieved in the blood for extended periods of time.

For protein drugs, the most common approach to achieve a constant release rate over time (zero-order drug release) is to encapsulate the protein in a micro- or nanocarrier [117,118]. In these carriers, the drug is thoroughly dispersed in a polymer matrix of for example, micro- or nanospheres, or it is concentrated in the center of for example micro- or nanocapsules. After administration, the drug is released from the polymer matrix by diffusion of the drug molecules through the pores of the matrix or by disintegration of the matrix, or by a combination of both [118-120].

The most common polymers used for protein encapsulation are poly(lactic acid) and poly(glycolic acid) and their copolymers. Their advantages as microcarriers were discussed in chapter 1. The mechanism of drug release from these polymers (PLA, PLGA or PGA) is a combination of diffusion and erosion. The rate of the drug release depends therefore on the

molecular weight of the polymer, its hydrophobicity and the size of the particles that entrapped the protein [117]. The polymer molecular weight and its hydrophobicity directly affect the rate of polymer degradation. We briefly discussed the mechanism of poly(ester) degradation and factors affecting it in chapter 1, and a detailed discussion can be found in a review by Gopferich [121].

Particle size is also an important factor in the rate of drug release from the particles. Considering Fickian diffusion law (**Eq.1-1**) for drug release from inside of the particle into a liquid media, correlation between the drug release rate and particle size becomes clearer. It was discussed in detail in chapter 1, section 1.1.3.

The particle diameter is another important factor which determines disintegration rate. Particles with larger diameter have smaller surface to volume ratio that limits water penetration into the particles and causes slower degradation of the polymer and consequently, slower diffusion of the drugs [117]. Therefore, to design a reliable and predictable sustained release drug delivery system, it is essential to have particles with narrow size distribution.

In the previous chapters, the advantages of microfluidic systems in the production of narrow sized microspheres were described and a robust microfluidic flow focusing system was designed and tested for this purpose. To be able to encapsulate proteins inside the PLLA microspheres, a double emulsion technique should be used and a water-in-oil-in-water (w/o/w) emulsion must be generated in the microfluidic system in order to maximize the encapsulation efficiency.

Several designs have been described in the literature for the generation of double emulsions in microfluidic systems [122-129]. Okushima *et al.* (2004) used two T-junction droplet generation units for the generation of a double emulsion from model fluids (**Figure 5-1a**) [125]. They successfully generated W/O/W and O/W/O emulsions. Their system performance was better when each emulsification step was done in a separate chip. Double emulsion generation in one

chip required very precise control of the flow rates. Small fluctuations affected droplet generation and double emulsion formation. Utada *et al.* (2005) and Abbaspourrad *et al.* (2013) showed a microcapillary flow focusing system that generates a double emulsion by passing three fluids coaxially through an orifice (**Figure 5-1b and c**) [122,126]. The double emulsion was generated either when same fluids were used for Inner phase (IP) and CP or when the viscosity of IP and CP is equal. In the system designed by Utada *et al.* (**Figure 5-1b**), double emulsion was generated when viscosity of the inner phase and dispersed phase was equal [126] which is not a practical condition when using protein and polymer solutions. Abbaspourrad *et al.* used the same design, yet their droplet generation was limited to core-shell structures with ultra-thin shell layers (**Figure 5-1 c**). They have also used a 10% PVA solution for both inner phase and outer phase to have a similar interfacial tension on both sides of the middle phase [122]. Chu *et al.* (2007) showed the possibility of generating a double or triple emulsion in microfluidic systems by separating the fluids and performing two or more independent emulsifications on a chip (**Figure 5-1d**) [124]. In their system, initial droplets were generated in the co-flowing section of the chip and then the droplets passed through a short channel to the flow focusing part where the final water droplet encapsulated in an oil droplet was generated. Their design could also generate multiple core droplets by careful adjustment of the flow rates and it was even used for triple emulsion (W/O/W/O) generation by simple modification [124]. Their strategy was reconfirmed by Abate and Weitz (2009). They showed the possibility of connecting several flow focusing droplet generation units in series and they produced from single to quintuple emulsions in one chip [129]. For multicore droplet generation Adams *et al.* (2012) reported a design similar to Utada *et al.* that incorporated two or more different species into the core of one droplet (**Figure 5-1e**). For their purpose, they changed the single inlet for the inner fluid to a multiple

fluid inlet and carefully aligned them with the orifice of the collection tube [123]. It was an improvement in terms of encapsulating different core materials into one droplet. Yet, similar to Utada *et al.*'s system they only tested it with model fluids (oil and water) and discussed only the formation of droplets, not of microspheres. Deng *et al.* (2014) used a completely new technique for the generation of a double emulsion. Core-shell droplets were generated based on the principle of drop-pairing (**Figure 5-1f**). In their system, water and oil droplets were generated separately in two channels which came into contact with each other in an expanded chamber. By controlling the flow rate and interfacial tension between the two phases, one droplet engulfed the other one [128].

The aforementioned designs showed the feasibility of a double emulsion generation in microfluidic systems. The authors showed robust and novel designs and studied the effect of different parameters on the droplet size and on the mechanism of droplet generation. However, all these designs have only been tested on a limited range of model fluids. We are not aware of any research group that showed a microfluidic design that can successfully generate a double emulsion of a protein solution as the inner phase and a biocompatible polymer as the disperse phase. In addition, the majority of work discussed here only mentions the formation of droplets, not of the microspheres / microcapsule morphology and encapsulation efficiency after extracting and/or evaporating solvents.

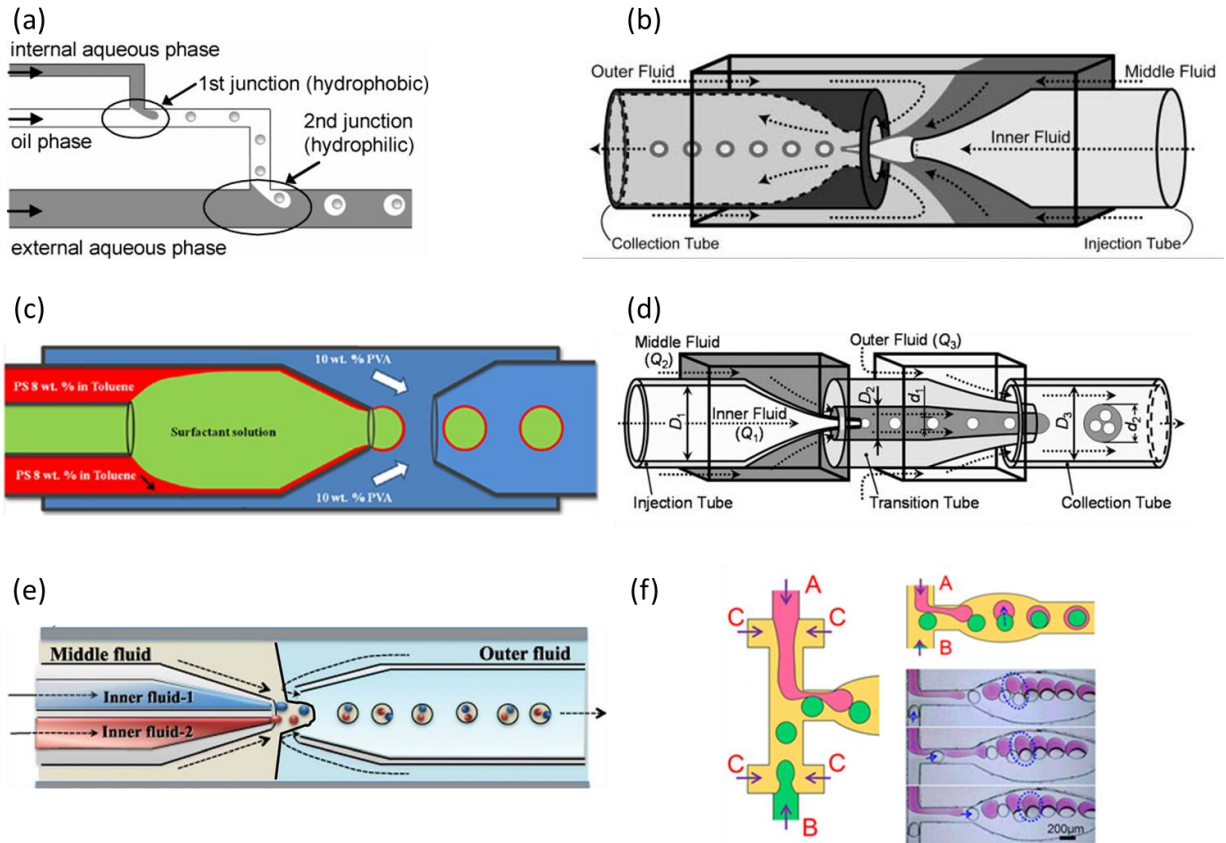


Figure 5-1: Different designs for performing double emulsion in microfluidic chip. (a) double T-junction system purposed by Okushima et al. [125], (b) single flow focusing system purposed by Utada et al. [126], (c) single flow focusing system purposed by Abbaspourrad et al. [122], (d) multiple flow focusing- co-flowing system for single or multiple core droplet generation purposed by Chu et al. [124], (e) single flow focusing system for multi-core droplet generation purposed by Adams et al. [123], and (f) Drop-pairing system for core-shell droplet generation proposed by Deng et al. [128].

Substituting model fluids with protein and polymer solutions affects the droplet generation mechanism, size of the inner (core) and outer (shell) droplets and emulsion stability. The parameters that determine droplet size and properties were discussed in the previous chapters and are defined by ratio of viscous force to interfacial tension, Ca , ratio of inertial force to interfacial tension, We , and ratio of inertia to viscose force, Re . These numbers vary when physicochemical

properties and operational conditions of the system change, hence, the mechanism of droplet generation is affected.

A microfluidic system that can generate the double emulsion for encapsulation of protein based drugs in polymer microspheres directly on a microfluidic chip has not been described yet in the literature, to the best of our knowledge. Here, we designed a microfluidic system for the encapsulation of proteins in biocompatible polymers and show the design and the results obtained from the encapsulation of bovine serum albumin in biocompatible and biodegradable PLLA microspheres.

5.2 Material and Methods

5.2.1 Fabrication of the Double Emulsion Generating Microfluidic System

The designed system (**Figure 5-2b**) contained two droplet generation units and a passive droplet break up section. Section 1 contained a flow focusing system and the passive droplet break up unit, referred as FF-PDB section and section two contained a flow focusing droplet generation unit. Each section had been printed on a separate mask and labeled mask 1 and mask 2, respectively. The whole system was fabricated on a 100 mm diameter and 2 mm thick borofloat glass wafer with one reference flat and standard transparent finish 60/40 (Valley Design Corp., Shirley, MA, USA).

The wafer was coated with 0.02 μm of chromium and 0.25 μm gold and then spin coated with positive photoresist (Shipley S1813; MicroChem Corp., Newton, MA, USA; **Figure 5-2a.1**). The pattern on mask 2 was transferred using a Canon PLA-501F mask aligner and developed with MF-319 photo developer (Rohm and Hass Electronic Material LLC, Marlborough, MA, USA; **Figure 5-2a.2**). After removing the photoresist (**Figure 5-2a.3**), the channels were etched 33-38 μm deep using concentrated HF (49%; Avantor; **Figure 5-2a.4**). The wafer spin coated with

photoresist S1813 one more time (**Figure 5-2a.5**). Pattern on mask 1 was aligned with structure on the wafer and transferred onto the wafer using the Canon mask aligner (**Figure 5-2a.6**). The pattern was developed and then the photoresist was removed (**Figure 5-2a.7**). The wafer was immersed into 49% HF solution to etch the channels.

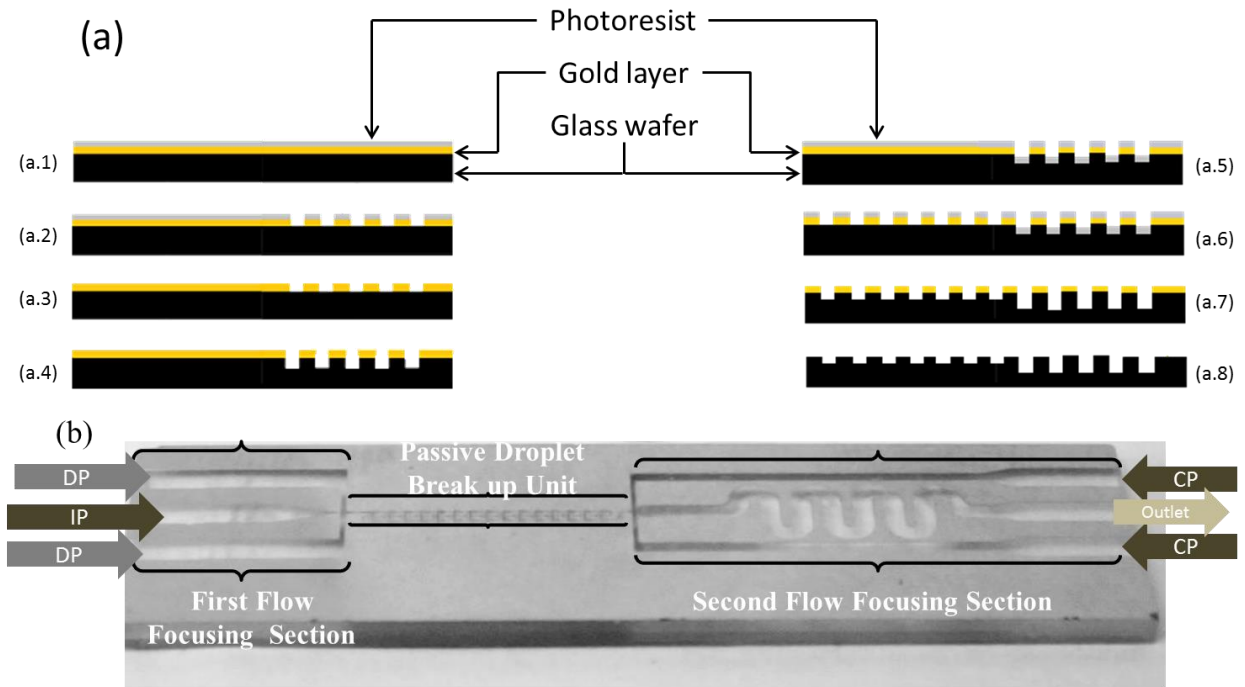


Figure 5-2. Schematic microfabrication process of the microfluidic system for double emulsion generation system. A 100 mm glass wafer was coated with chromium, gold, and a positive photoresist (a.1). After microfluidic flow focusing pattern transformation, coating was removed from the pattern area (a.2) and the photoresist was removed from the whole wafer (a.3). The glass was etched with highly concentrated HF (a.4). The wafer was coated with the positive photoresist again (a.5). FF-PDB pattern on mask 1 is transferred and then photoresist in removed (a.6). Channels were etched by submerging the wafer into high concentration of HF solution (a.7) followed by removing all coated materials (a.8). The wafer was cut into 50×15 mm² slices and bonded onto another glass wafer of the same size to cover the channels. (b) Fabricated microfluidic glass chip before bonding.

Etching stopped when the channel depth in the FF-PDB section of the chip was between 10 – 12 μm . The chip features were measured by an Alpha step 200 profilometer (Tencore instrument, Mountain View, Ca, USA). Gold and chromium coating were removed (**Figure 5-2a.8**) and the wafer was diced into $50 \times 15 \text{ mm}^2$ chips. Glass lids of the same size were cut from another wafer and thermally bonded to the microchips (6 h at $650 \text{ }^\circ\text{C}$).

5.2.2 Coating of the Chip

Before bonding the glass slide to the chip, the FF-PDB section of the chip was coated with 1H, 1H, 2H, 2H-perfluorododecyltrichlorosilane (PFDTCS; Santa Cruz Biotechnology Inc., Santa Cruz, CA, U.S.A.) (**Figure 5-3**).

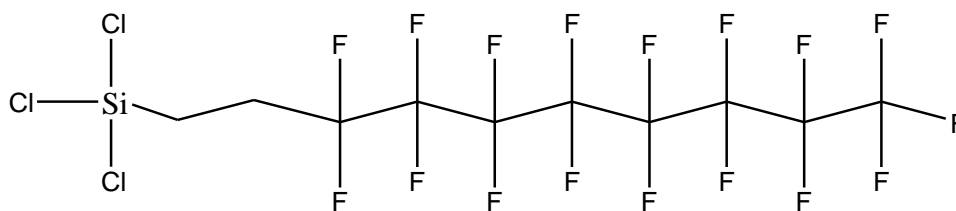


Figure 5-3. Molecular structure of 1H, 1H, 2H, 2H-perfluorododecylchlorosilane.

Coating was done according to the method explained by Srinivasan [130] with slight modification. Specifically, a sealed flask was weighed and a tip of the spatula of the PFDTCS was added to that and weighed again. Immediately, the flask was placed under vacuum for 5-10 min and then filled with argon gas. Iso-octane was added to the system to get to the final concentration of 1 mM PFDTCS in iso-octane, while the solution was kept under argon gas. The chip which had been etched by HF and rinsed thoroughly with water was immersed in a Petri dish filled with 2-propanol. After 5 min it was transferred to another Petri dish filled with iso-octane. Solvent was removed after 5 minutes, the dish filled with fresh iso-octane and the chip incubated in there for another 5 min. The chip was then vertically placed into the flask

containing the PFDTCS solution, so that the solution only covered the FF-PDB section of the chip. Argon was pushed into the flask and purged from the outlet port for 3 min, the system closed and left for 10 min for the PFDTCS-coating reaction to take place. After 10 min, the chip was removed from the flask and placed in a Petri dish filled with iso-octane for 10 min with a solvent change after 5 min, followed by two more 5 min incubations in a 2-propanol filled dish. Finally, it was submerged into water for 5 min and rinsed and dried thoroughly.

The hydrophobicity of the surface after coating was determined via contact angle measurement of a water droplet on the coated surface using the free version of the Analysis Software “First Ten Angstroms Drop” (FTA32 2.0, Portsmouth, VA, USA) and compared the results to the contact angle of an uncoated chip.

5.2.3 Protein Loaded Microsphere Production

Three phases were required for the generation of w/o/w emulsion in the chip. The inner phase (IP) was prepared by dissolving BSA in PBS. The dispersed phase (DP) was made of 10% PLLA (2 - 3 kDa) in chloroform. Different concentrations of Span 80 (Sigma-Aldrich, Canada) were added to the dispersed phase to stabilize the formed water in oil emulsion. The continuous phase (CP) was 2% PVA (13-23 kDa and 83-87% hydrolyzed). Solutions were prepared fresh for the day and filled in glass syringes. Different operational conditions (**Table 5-1**) were used to optimize the encapsulation of BSA in PLLA microsphere. Droplets generated were collected and placed under vacuum (60 – 70 mTorr) for 45 min for solvent removal, washed three times and then suspended in distilled water and lyophilized.

5.2.4 Protein Labeling

In all experiments BSA was tagged with a fluorescent dye, Alexa 555 (A555) before preparing inner phase solution. For this purpose, 10 mg of BSA was dissolved in 500 μ L PBS at pH 7.2

and a solution of 20 μL of A555 dissolved in DMSO (1 mg/mL) added. After shaking overnight at 500 rpm, the unconjugated dye was separated from the solution by centrifugation at 14000 $\times g$ in a micro-concentrator. The filtrate was washed by resuspension in 200 μL of PBS and centrifugation at 5000 $\times g$. The washing step was repeated several times until the wash-off liquid became colorless. To collect BSA conjugated A555 (BSA-A555), 50 μL PBS was added to the insert, shaken, the insert of the micro-concentrator flipped over into another clean tube and centrifuged at 4000 $\times g$ for 10 min. This was repeated 3 times to recover the maximum amount of BSA-A555.

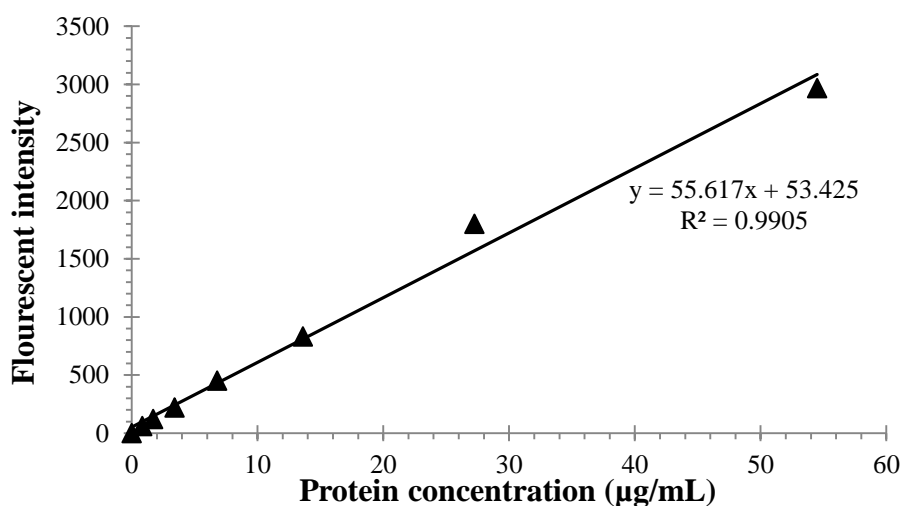


Figure 5-4. Protein standard curve. Known concentration of BSA labelled with Alexa 555 (BSA-A555) was diluted in 5% SDS in 0.1 N NaOH solution. The fluorescent intensity of the solutions was measured at 550 nm and 585 nm excitation and emission wavelength, respectively.

The protein concentration in the solution was measured using a standard μBCA assay. A standard curve (**Figure 5-4**) was prepared by diluting the protein solution in 5% sodium dodecyl sulphate (SDS) solution of 0.1 N NaOH. From each dilution, 100 μL was added to a 96-well

plate, the fluorescent dye excited at 550 nm and the fluorescent intensity measured at an emission wavelength 585 nm.

5.2.5 Protein Encapsulation Efficiency

To determine the mass of encapsulated protein, ~ 2.5 mg of dried microspheres were mixed with 1 mL of 5% SDS in 0.1 N NaOH solution. The suspension was mixed at 500 rpm in the dark at room temperature overnight for complete polymer disintegration. A 100 μ L aliquot was then taken from the solution and added to a 96-well plate. Fluorescent intensity of the BSA-A555 in the solution was determined at 550 nm and 585 nm excitation and emission wavelength, respectively. The protein concentration was determined from the standard curve (**Figure 5-4**). The protein encapsulation efficiency (EE) was then determined as

$$EE (\%) = \frac{\text{mass of protein encapsulated}}{\text{initial mass of protein}} \times 100 \quad 5-1$$

5.3 Results and Discussion

5.3.1 Microchip Surface Coating

The initially prepared glass chip has a hydrophilic surface. Since the FF-PDB part of the chip will be used for the generation of water in oil emulsion, the surface needs to be coated with a hydrophobic material that can tolerate chloroform. A literature search found PFDTCS to be an effective compound to hydrophobically coat glass surfaces that then can tolerate chloroform. The coating takes place by a self-assemble mechanism (SAM) (**Figure 5-5**) from the liquid phase [130].

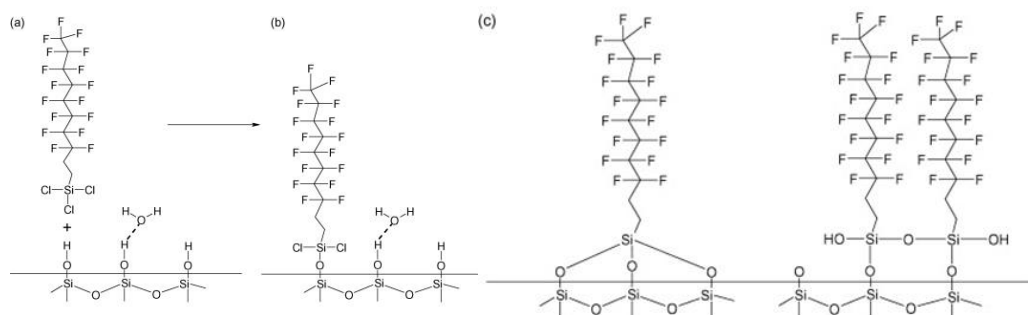


Figure 5-5. Self-assembly mechanism of PFDTCS coating on the glass surface [131].

Images taken from two water droplets on the coated and uncoated part of the chip clearly showed that the coated surface is more hydrophobic than the uncoated one. The contact angle of a water droplet on these surfaces was 52° and 106° for the uncoated and coated surfaces, respectively.



Figure 5-6. Water droplets on the microfluidic glass chip (a) coated with PFDTCS, and (b) uncoated.

5.3.2 Protein Encapsulation in Microfluidic System

A microfluidic system was designed and optimized that can be used for the encapsulation of hydrophilic drugs, small molecules or proteins, in polymer microspheres. For this purpose, we modified the designs of the system reported by Chu *et al.* [124] by adding a modified passive droplet break up unit [132] between the two droplet generating units (**Figure 5-7**).

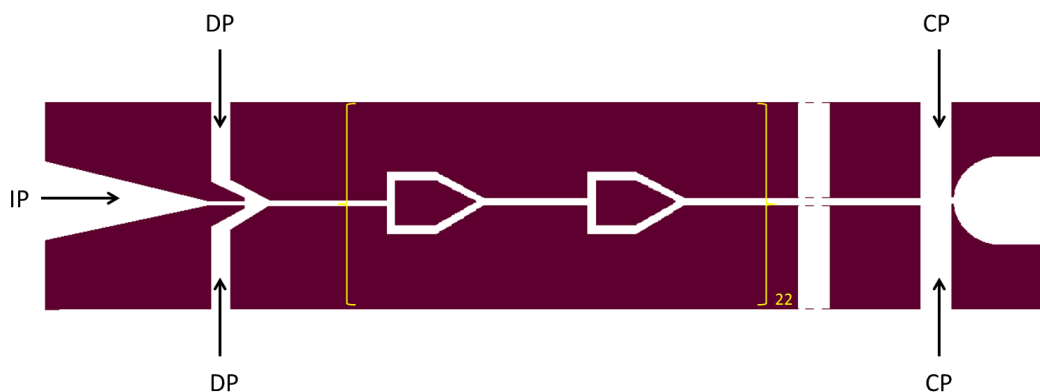


Figure 5-7: Schematic diagram of the double emulsion generating microfluidic system used for BSA encapsulation in PLLA microspheres.

In our system, the initial water droplets were generated in the first flow focusing unit. The generated droplets were then broken down into smaller droplets by letting them collide with a barrier and splitting the flow into two parts (similar to a T-junction unit reported by Link *et al.* 2004). The two flows were combined again before the second and next splitting unit. In the passive droplet break up section, the droplets collided into a barrier and they break up into smaller ones then the splitted stream rejoined again. This cycle is repeated several times (i.e., 22 times in **Figure 5-7**). Due to the several time splitting and rejoining of the mixture of protein droplets and polymer solution in this section, protein droplets disperse in the polymer solution and form a stable heterogeneous emulsion (different sizes of protein droplets are distributed throughout the polymer solution) before entering in the second flow focusing section of the chip for secondary droplet generation that will lead to the formation of the final microspheres.

The mechanism of droplet break up in sequential T-junction units has been studied by Link *et al.* [132]. They showed that the droplet breakup at the junction depends on the velocity of the flow. Below the so-called critical velocity, the breakup does not happen. In Link *et al.*'s system, the initial flow was divided several times sequentially and then recombined at the end.

To guarantee the critical velocity even at the final splitting unit, a minimal initial flow rate was required. As mentioned by the authors, the required high initial pressure might be beyond the tolerable pressure of the system [132] whereas in our system, the flow rate remains constant throughout the splitting and rejoining which allows us to work with much lower flow rates while assuring a fluid velocity at the T-junction units above the critical velocity. Our system is thus not limited by the number of splitting units that can be used.

In order to create protein loaded microspheres, protein droplets must be distributed throughout the polymer matrix during the emulsion generation period. In conventional emulsion generation systems, the stable emulsion is generated by mixing the two fluids with a high speed homogenizer. As discussed in chapter 1 in the microfluidic systems, fluids are mixed either by diffusion (for miscible fluids) or by generating chaotic advection (for miscible and immiscible fluids). In our system, the flow pattern is laminar throughout the channels and the channels are straight with smooth surfaces, so chaotic advection cannot be generated in the system. The droplets flowing through these channels have different sizes, which makes them flow at different velocities. This difference in velocity causes the particles to collide with each other inside the straight channels and when the two channels meet again. As a result, the straight movement of the droplets in the channels is disturbed. Collision happens all the time during their movement in the channels before entering the second droplet generating unit. At the same time, the collisions cause the droplets to remain suspended in the polymer solution.

The performance of the chip for generation of w/o/w emulsion was initially tested by using fluorescein sodium dye in water as the inner phase. The droplet generation process was observed under a light microscope and the encapsulation of yellow droplets inside the polymer droplets indicated the formation of a stable double emulsion inside the chip (**Figure 5-8a**). The

fluorescence microscopy image of the dried microsphere confirmed the encapsulation of the sodium dye inside the microspheres as well (**Figure 5-8b to d**).

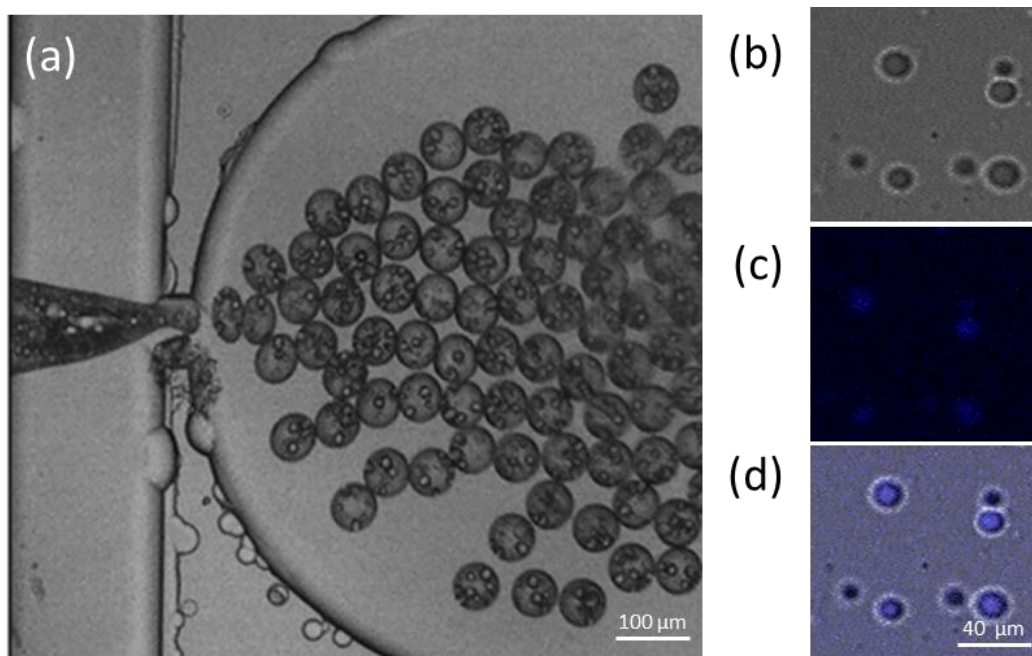


Figure 5-8. (a) Light microscope image of double emulsion generation in the microfluidic system. (b-d) Bright field and fluorescent microscopy images of the PLLA microspheres that show successful encapsulation of the dye inside the polymer microspheres. (b) Bright field image of the microsphere. (c) Fluorescent image of the particles. The excitation wavelength was ~490 nm. (d) Superimposed image of the particles. The inner phase was fluorescein sodium dye dissolved in water and its flow rate was 0.2 $\mu\text{L}/\text{min}$, the dispersed phase is 10% PLLA in chloroform and 10% Span 80 and its flow rate was 0.8 $\mu\text{L}/\text{min}$, and the CP was 2% PVA and its flow rate was 30 $\mu\text{L}/\text{min}$.

The successful dye encapsulation inside the PLLA microsphere confirmed the capability of the developed microchip for the generation of double emulsion and was a proof of our idea for the generation of drug loaded microspheres by combining droplet generating flow focusing system with a passive droplet break up unit. This initial result can be generalized for the encapsulation of small molecule drugs, yet encapsulation of protein would be a challenge since the addition of protein to the inner phase significantly changes (increases) the viscosity of the phase.

It is well known that proteins have a tendency to arrange themselves at the interface of water and organic solvents, the property that affects the interfacial tension between the two solutions and consequently would affect the droplet formation in our system. Therefore, a simple generalization from a model dye to a protein solution is not possible and extensive optimization is required.

BSA conjugated with Alexa 555 was used as model protein to investigate the effect of different operational conditions including flow rate of the inner phase, concentration of Span 80 in dispersed phase and flow rate of the CP on the protein encapsulation efficiency in the PLLA microspheres. Other conditions such as the concentration of polymer in the dispersed phase and dispersed phase flow rates had been optimized for the production of monosized microspheres before (chapter 2). We used the same conditions to reduce the number of variables.

The presence of surfactant in the disperse phase is crucial for the generation of a stable w/o emulsion in the FF-PDB section of the chip. In the initial performance experiment, the concentration of Span 80 (10% (v/v)) was relatively high. As the residual surfactant in the final product is a potential source of toxic reactions *in vitro* and *in vivo*, it would be better to minimize its use in the particle generation. To optimize the surfactant concentration, the formation of stable droplets in the first flow focusing unit was monitored at different Span 80 concentration. The initial emulsion in the FF-PDB section of the chip did not form reliably when the concentration of surfactant (Span 80) in the dispersed phase was below 4% (v/v), phase separation between the protein and polymer solution was observed (**Figure 5-9**).

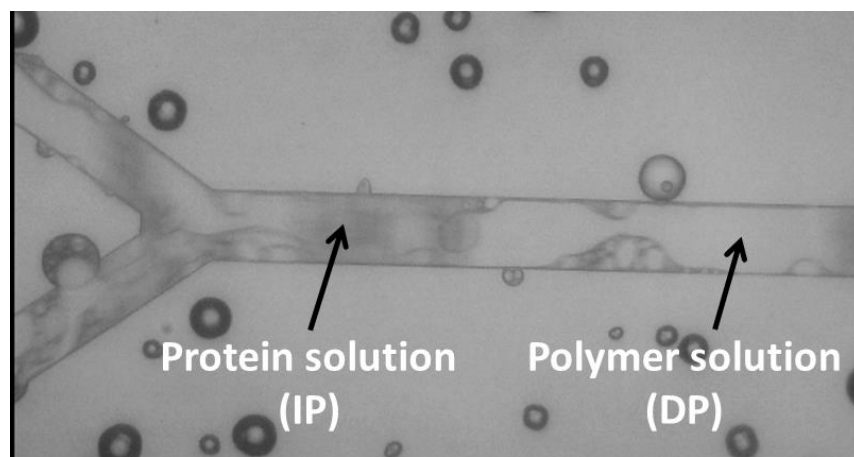


Figure 5-9: A snapshot of passive droplet break up section of the double emulsion generation microfluidic system that shows the phase separation between IP and DP when Span concentration is 1% (v/v).

For the rest of the experiments and to investigate the effect of the inner phase (IP) and CP flow rates, the concentration of surfactant in the dispersed phase was set to 4% (v/v). **Table 5-1** shows the encapsulation efficiency of BSA-A555 in PLLA microspheres at different IP and CP flow rates. The results clearly show that our newly designed microfluidic system is capable of producing protein loaded microspheres with high protein encapsulation efficiency.

The maximum encapsulation efficiency was achieved when the IP flow rate was 0.05 $\mu\text{L}/\text{min}$. At this flow rate, protein encapsulation efficiencies of 68% or more were achieved reliably and reproducibly (**Figure 5-10**). At higher flow rates, encapsulation efficiency decreased. When the IP flow rate exceeded 0.1 $\mu\text{L}/\text{min}$, no droplets formed in the FF-PDB section. At flow rates smaller than 0.04 $\mu\text{L}/\text{min}$, the system became completely unstable and the flow of the IP frequently blocked by the dispersed phase.

Table 5-1. Comparison of encapsulation efficiency of the BSA in PLLA microspheres using the double emulsion generating microfluidic system at different IP and CP flow rates.

Inner phase flow rate ($\mu\text{L}/\text{min}$)	Dispersed phase flow rate ($\mu\text{L}/\text{min}$)	Continuous phase flow rate ($\mu\text{L}/\text{min}$)	Encapsulation efficiency (%)	Maximum encapsulation efficiency (%)
0.07	1	10	5.84	5.84
0.07	1	40	7.27	7.27
0.05	1	10	68.21 \pm 4.40	84.05
0.05	1	20	69.70 \pm 11.18	82.25
0.05	1	40	77.65 \pm 16.35	96.02

In all experiments, the IP was 5.45 mg/mL BSA in PBS; DP was 10% (PLLA and PEG-PCL at a 96:4 ratio) and 4% Span 80 in chloroform; and CP was 2% PVA in water.

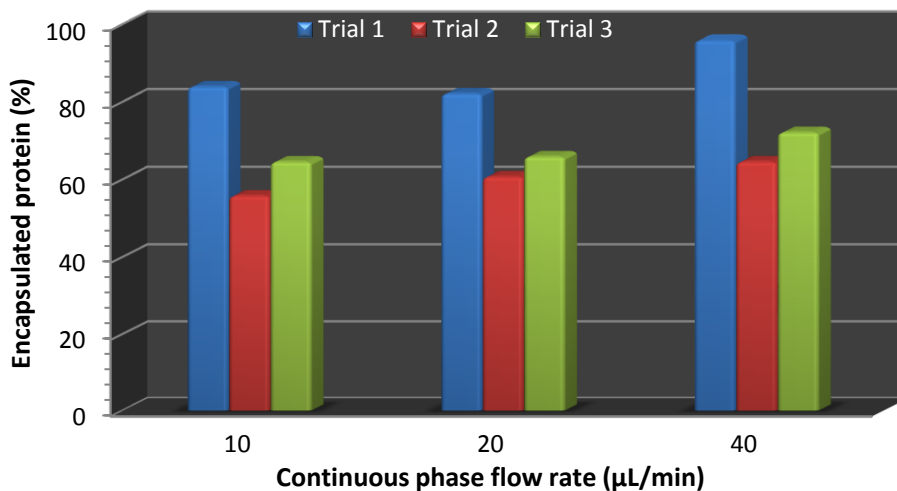


Figure 5-10. Protein encapsulation efficiency in PLLA microsphere produced at different CP flow rate. In all experiments, inner phase was 5.4 mg/mL BSA-A555 in PBS and IP flow rate was 0.05 $\mu\text{L}/\text{min}$, disperse phase was 10% (PLLA and PEG-PCL in 96 to 4 mass ratio) in chloroform and 4%(v/v) Span 80 and DP flow rate was 1 $\mu\text{L}/\text{min}$, and CP was 2% PVA in water.

As explained in chapter 1, droplet generation depends in flow focusing systems on the interfacial tension and viscous forces between the fluids and on their flow rate ratios. Therefore, increasing the flow rate of the inner phase may require increasing in the flow rate of the disperse phase to keep the balance of the forces in favor of droplet generation.

Higher flow rates correspond to higher pressure for pumping, their correlation between the two can be seen in **equation 5-2** [133].

$$R_{ch} = \frac{\Delta P}{Q} \quad 5-2$$

' R_{ch} ' is known as resistance to flow. Flow resistance depends on the geometry of the channels and for a fully developed flow in a rectangular channel with $W/H < 1$ can be calculated from **equation 5-3** [133]

$$R = \frac{a_{ch}\mu l}{Wh^3} \quad 5-3$$

Therefore,

$$\Delta P = \frac{a_{ch}\mu Ql}{Wh^3} \quad 5-4$$

where, ' a_{ch} ' is a dimensionless parameter calculated from **equation 5-5** [133], μ (kg/m·s) is the viscosity of the fluid, Q (m^3/s) is the fluid flow rate, l (m) is the length of the channel, W (m) is the channel width and h (m) is the channel depth.

$$a_{ch} = 12 \left[1 - \frac{192h}{\pi^5 W} \tanh\left(\frac{\pi W}{2h}\right) \right]^{-1} \quad 5-5$$

For an arbitrary microchannel cross-section, the pressure drop can be calculated from **equation 5-6** [134,135]:

$$\Delta P = 16\pi^2 \mu Q I_P^* \frac{L}{A^2} \quad 5-6$$

These equations indicate that the flow resistance in a channel is very sensitive to the channel dimensions, flow rates of the fluids and their viscosity. Due to the small channel sizes in the FF-PDB section of the chip, increasing the disperse phase flow rate caused a significant increase in the back pressure. For example, the pressure drop along 1 μm length of the channel in the FF-PDB section when $\mu = 2.92$ cP, $w=30$ μm , and $h=10$ μm , is $2.5 \times 10^{10} \times Q$ (Pa). This high back pressure led to difficulties in pumping the fluids into the chip. It also created a very high pressure at the orifice where DP and IP come into contact with each other and interrupted the flow of the IP. The workable flow rate for the inner phase was therefore between 0.05 to 0.07 $\mu\text{L}/\text{min}$ with the maximum encapsulation efficiency at DP = 0.05 $\mu\text{L}/\text{min}$.

At the optimal IP flow rate, we observed that the protein encapsulation efficiency increased with increasing CP flow rate (**Figure 5-10**). The higher encapsulation efficiency at higher CP flow rate might be associated with the droplet size formed in the second flow focusing section of the chip and the rate of solvent extraction from the droplets. Solvent removal from the particles takes place in three stages: (1) diffusion of the solvent from the inside of the droplets to their surface, (2) dissolution of the solvent in the CP surrounding the droplets and (3) evaporation of the solvent at the CP-air interface. Stage two and three are independent of particle size and depend on the solvent solubility in the CP and its vapor pressure. Stage one, the rate of solvent diffusion, however, is size dependent [136] and the Fickian diffusion law applies for the rate of

solvent diffusion in the polymer droplets (**Eq. 1-2**). By increasing the CP flow rate, the size of the polymer droplets decreases. Consequently, the solvent extraction time decreases and the polymer matrix solidifies faster which minimizes the rate of protein loss from the droplets during the solvent extraction and evaporation process.

5.4 Conclusions

Being able to encapsulate the 66 kDa protein BSA at high encapsulation efficiencies of up to 96% with the help of our purpose-designed flow focusing chip containing 3 connected sections proves that the idea of making a continuous protein loaded microsphere on a chip works. There are still a few hurdles to overcome. For example, the flow rates are rather limited, which restricts the amounts of microspheres that can be produced. More specifically, the emulsion generation in the first section of the chip relies on the formation of droplets in the flow focusing unit. Due to the small dimension of the channels in this section, the system faces a limitation on the range of workable flow rates. The highest possible flow rate for the inner phase was 0.07 $\mu\text{L}/\text{min}$ and the optimal flow rate of IP was observed to be 0.05 $\mu\text{L}/\text{min}$. Yet, at this flow rate, the protein encapsulation efficiency was high, between 55% and 96%.

Moreover, the concentration of the surfactant in the IP is relative high, and the size of the generated droplets in the FF-PDB section is still large compared to the size of the droplet generated in the second flow focusing section. Further improvement in the design of the chip, i.e., using parallel FF-PDB system, or proportionally increase the dimension of the channels, is required in order to increase the workable range of fluids and hence increase the production rate.

Chapter 6: Summary, Conclusions and Suggestions for Future

Work

6.1 Summary

The development of therapeutic proteins and nucleic acid therapeutics escalated the development of advanced drug delivery systems that can deliver high concentrations of drugs to a specific tissue/organ with minimal side effects or that protect the susceptible protein from rapid degradation or deactivation [2-4,6]. The first advanced drug delivery systems for proteins were reported by Langer and Folkman [137] who encapsulated proteins in a non-biodegradable polymer. In spite of the successful entrapment of protein, difficulties in administration of non-biodegradable devices resulted in the development of biodegradable microparticles as an alternative approach [2].

Different techniques have been used for the production of biodegradable polymer microspheres with emulsification being the most common method. In this method, polymer rich droplets are formed by mixing two immiscible fluids and then applying stress to the system to break the polymer phase into small droplets. The droplet size is proportional to the magnitude and time of the force applied to each droplet. From each droplet, a microsphere is obtained through the process of solvent extraction and/or solvent evaporation. In bulk emulsification methods, where high speed homogenizers are used to introduce force into the system, controlling the size of the particles is very difficult and the size distribution is generally broad. Emulsifications done in microfluidic channels are much better controlled and apply stress more homogeneously leading to better controlled droplet generation [138-141].

Microfluidic flow focusing systems are generally fabricated out of silicone, polymers or glass. The material choices depend on the application, cost and ease of fabrication method [59]. For our purpose, chip transparency and resistance to chloroform were the most important criteria that led to the selection of borofloat glass for chip fabrication. The chip design was developed from our previous flow focusing system [69] by modifying the shape of the orifice and increasing the length of the downstream channel in order to simplify the fabrication process and facilitate partial solvent extraction directly on the chip.

6.1.1 Production of Polymer Microspheres in a Microfluidic Flow Focusing System

In chapter 2 the effect of operational conditions on the size and size distribution of the produced microspheres was investigated. Droplet generation in a microfluidic flow focusing system is generally categorized into geometry–controlled, dripping, jetting, and tip-streaming regimes. The regime is determined by the flow rates and viscosity of the fluids, interfacial tension between fluids, and the geometry of the channels.

Our chip was optimized for the production of narrow size distribution particles at different flow rates with distinct sizes between 7 – 40 μm . At low flow rates, $Q_{\text{CP}} < 20 \mu\text{L}/\text{min}$ and $\text{Ca} < 0.01$, droplets formed under geometry controlled conditions with sizes bigger than the size of the orifice. These large particles break down into smaller droplets as they move through the channels. At higher flow rates, $Q_{\text{CP}} = 150 \mu\text{L}/\text{min}$ and $\text{Ca} = 0.05$, droplets formed under jetting condition with a large size distribution. More narrowly sized quasi-monodisperse microspheres ($\text{CV} < 16\%$) were produced at CP flow rates between 30 to 80 $\mu\text{L}/\text{min}$ and $\text{Ca} < 0.04$.

The Ca number achieved in our system for each regime was significantly different from the Ca defined by Anna and Mayer [38]. The deviation observed is speculated to be due to the different

fluids used in our system. Changing the fluids from Newtonian fluids, as in Anna and Mayer's work, to non-Newtonian fluids, as in our work, affects the rheological properties of the fluids and might alter the mechanism of droplet generation in our system. Figuring out the differences in detail, however, will require further investigation.

Our results show bimodal size distributions for all the different flow rates and flow rate ratios that we tested. The peak with the larger droplets describes the primary droplets, while the peak with the smaller droplets describes the satellite droplets whose volume is less than 1% of the primary droplets. The formation of satellite droplets in a viscoelastic system like ours can be explained by the physicochemical properties of the used fluids as they affect necking and pinch off time of the fluids

The mechanism of droplet formation in a flow focusing system has shown that a droplet pinches off from the dispersed phase stream after it is necked and elongated [38,40]. Satellite droplets form when the neck becomes asymmetric before the droplet pinches off [53,62]. In addition, the viscosity ratio of the dispersed phase to the continuous phase can influence not only the size of the droplets but their size distribution because it changes the necking process and separation time. Drezsi *et al* showed that satellite droplets are generated when the DP to CP viscosity ratio is smaller than 1 [54].

According to these criteria, satellite droplets should have been eliminated in our system. Other potential reasons for the formation of satellite droplets in our system might be the pump accuracy and precision in delivery of fluids.

6.1.2 Computational Modeling of Droplet Generation in Microfluidic Flow

Focusing System

The experimental investigation of all the different parameters of droplet generation in a flow focusing system is a time consuming and demanding process, and we decided to develop a computational modeling system of droplet generation. In chapter 3, a 3D computational model is described that simulates the droplet formation in our microfluidic flow focusing system. Simulations were performed for five different flow rate combinations and compared to the experimental results obtained in our microfluidic chip. The experimental droplet size agreed with the 3D simulation results within 0.7% to 17% for all conditions. This indicates the accuracy of the model used for the prediction of the droplet generation in our microfluidic flow focusing system.

6.1.3 Encapsulation of Magnetic Nanoparticles in Quasi-Monodisperse Polymer Microspheres

Adding magnetic nanoparticles to the dispersed phase changed its physicochemical properties and consequently affected the droplet formation conditions. It was observed that the percentage of satellite droplets was generally lower in the magnetic microspheres than in the non-magnetic ones due to an increase in the DP viscosity.

The magnetic microspheres (MMS) were superparamagnetic and thus suitable agents for internal administration, as such MMS do not aggregate *in vivo*. To investigate the applicability of the fabricated MMS for hyperthermia and heat inducing drug release formulation, their thermal properties were also measured in an alternating magnetic field. The highest measured particle specific absorption rate was 202.6 W/g of MNPs, giving the MMS an overall SAR of 32.1W/g. Particles with this thermal capacity can be used for hyperthermia treatment of cancer with tumors

sized 5 mm or larger. Smaller tumors would require particles with a minimum SAR of 500 W/g [100], which could be obtained by increasing the content of MNP in our MMS and/or the help of larger magnetic nanoparticles that have been described to improve the SAR many folds.

6.1.4 Encapsulation of BSA in PLLA Quasi-Monodisperse Microspheres

Protein encapsulation into polymeric microspheres is challenging. In the conventional method, proteins are made into an emulsion with the organic solvent with a high speed homogenizer and then formed into microspheres using the double emulsion technique. The risk of protein aggregation and conformational change in that procedure is rather high. Forming a double emulsion directly in a microfluidic flow focusing chip reduces the risk of the protein damage by the high speed homogenization as the method is much more controlled and very rapid.

In Chapter 4, the design and fabricating of a microfluidic system is described for encapsulation of BSA in PLLA quasi-monodisperse microspheres. The final system contains two droplet generation units separated by a passive droplet break up unit and is fabricated on a single chip. The optimal operational conditions for maximum protein encapsulation efficiency were determined in Chapter 5 and showed that the system is capable of producing protein rich droplets in polymer solution at very low flow rates of the internal phase (IP), 0.07 and 0.05 $\mu\text{L}/\text{min}$. The system, however, is rather sensitive to small changes. For example, at lower flow rates, the IP flow is blocked by the DP stream. At flow rates higher than 0.07 $\mu\text{L}/\text{min}$, flow does not break into droplets at all. BSA encapsulation efficiencies of 55% to 96% could be achieved reliably and reproducibly at the IP flow rate of 0.05 $\mu\text{L}/\text{min}$.

6.2 Contributions

With this thesis, the following contributions to the field were achieved:

- ✓ Confirmed the feasibility of continuous production of drug loaded and magnetically targetable PLLA microsphere with a microfluidic system.
- ✓ Designed a microfluidic system that can be used for the production of reproducible quasi-monodisperse microspheres with distinct sizes between 7 – 40 μm .
- ✓ Showed the importance of geometry of the channels downstream of the orifice to retain the monodispersity of the generated droplet. The length of the channels after the orifice must be long enough to allow for partial solvent extraction from the droplets already inside the chip and the width of the channels should remain constant throughout the downstream channels to prevent particle coalescence and break up inside the chip.
- ✓ Encapsulated for the first time MNPs into polymer microspheres using a microfluidic flow focusing system.
- ✓ Produced MMS with superparamagnetic properties that are suitable for the hyperthermia of large tumors in cancer therapy.
- ✓ Designed a microfluidic system with integrated passive droplet break up for the generation of a stable water-in-oil-in-water emulsion.
- ✓ Encapsulated protein in polymer microspheres with encapsulation efficiencies up to 96% using an integrated one-chip microfluidic system.
- ✓ Performed 3D computational modeling that was able to simulate the droplet generation in a microfluidic flow focusing system reliably and accurately with less than 17% deviation between the simulation and experimental data.

6.3 Conclusions

The presented work is a first step in advancing our knowledge of how to design microfluidic systems that are able to encapsulate drugs into polymeric microspheres with narrow size

distribution. The newly designed flow focusing system can be used as a valuable tool for the production of differently sized microspheres made with clinically (FDA) approved polymers for use in clinical applications. The feasibility of this idea was supported by the production of ^{99m}Tc -radiolabeled PLLA microspheres that can be used for lung perfusion imaging, and when radiolabeled with ^{188}Re , for liver tumor radioembolization.

In conclusion, microfluidic systems are a reliable method for the continuous production of monodisperse polymer microspheres containing diagnostic and therapeutic agents, drugs and proteins for imaging and therapeutic application.

6.4 Suggestions for Future Work

The design of microfluidic flow focusing systems will further benefit from additional geometrical improvements. We showed that partial extraction of solvent in the chip can improve microspheres size distribution. Further experiments or computational modeling are required to correlate the particle size distribution and the shape and dimension of the channels after the orifice.

The current flow focusing system is capable of producing up to 5 mg of microspheres per hour. This low production capacity can be improved by connecting several of these chips in parallel. Further work needs to be done to determine the correct alignment of the chips in order to have constant, equal and uniform flow rates in all connected chips.

We showed two clinical applications for the use of quasi-monodispersed polymer microspheres. The lung perfusion study showed that a high concentration of PLLA microspheres accumulates in the lungs after a single intravenous injection. This mode of drug delivery to the lungs might be useful if oral or nasal drug delivery is not possible or if their efficiency is low.

Drugs could be easily incorporated into our biodegradable monosized microspheres to be slowly released in the lung capillaries for local therapy.

We also showed that quasi-monosized large PLLA microspheres sized between 30 and 40 μm can be produced in our chip with $^{99\text{m}}\text{Tc}$ chelators on the particle surface. Such microspheres can be radiolabeled with $^{99\text{m}}\text{Tc}$, a diagnostic gamma-emitting radioisotope, and its congener ^{188}Re , a beta-emitting therapeutic (cancer cell killing) radioisotope. The particles' safety and efficacy should be evaluated in an animal model for the radioembolization of liver cancer.

Drug loaded quasi-monosized microspheres might also be useful for drug delivery to the back of the eye, to the retina, for the treatment of chronic diseases that require long term drug therapy. For instance, the model protein BSA incorporated into microspheres in this dissertation can be substituted with an anti-vascular endothelial growth factor (anti-VEGF) and used in drug formulations for the treatment of age-related macular degeneration. Intravitreally administered anti-VEGF loaded PLLA microspheres could remain in the eye for many weeks and release the drug over the same time span. This will reduce the number of injections required for the treatment. In addition, the efficacy of the drug therapy can be improved if both drug and magnetic nanoparticles are co-encapsulated into the microspheres. Such microspheres could be directed magnetically towards specific areas of the retina with the help of an external magnetic field, followed by an extended period of localized drug delivery.

References

- [1] Sperling LH, Wiley-Blackwell Online B (2006). *Introduction to physical polymer science*. Wiley, Hoboken, N.J.
- [2] Griffith LG (2000). *Polymeric biomaterials*. Acta Mater **48**, 263-277.
- [3] Haag R, Kratz F (2006). *Polymer therapeutics: Concepts and applications*. Angewandte Chemie-International Edition **45**, 1198-1215.
- [4] Langer R (1998). *Drug delivery and targeting*. Nature **392**, 5-10.
- [5] Langer RS, Peppas NA (1981). *Present and future applications of biomaterials in controlled drug delivery systems*. Biomaterials **2**, 201-214.
- [6] Kissel T, Maretschek S, et al. (2006). *Microencapsulation techniques for parenteral depot systems and their application in the pharmaceutical industry*. Taylor & Francis Group, Boca Raton, FL.
- [7] Langer R (1990). *New methods of drug delivery*. Science **249**, 1527-1533.
- [8] Li M, Rouaud O, Poncelet D (2008). *Microencapsulation by solvent evaporation: State of the art for process engineering approaches*. Int J Pharm **363**, 26-39.
- [9] Erbacher C, Bessoth FG, et al. (1999). *Towards integrated continuous-flow chemical reactors*. Mikrochim Acta **131**, 19-24.
- [10] Nair LS, Laurencin CT (2007). *Biodegradable polymers as biomaterials*. Prog Polym Sci **32**, 762-798.
- [11] Jain RA (2000). *The manufacturing techniques of various drug loaded biodegradable poly(lactide-co-glycolide) (PLGA) devices*. Biomaterials **21**, 2475-2490.
- [12] Kumbar S, Laurencin C, et al. (2014). *Natural and synthetic biomedical polymers*. Elsevier Science, Amsterdam; Boston.
- [13] Auras R, Harte B, Selke S (2004). *An overview of polylactides as packaging materials*. Macromol Biosci **4**, 835-864.
- [14] Nihant N, Grandfils C, et al. (1995). *Microencapsulation by coacervation of poly(lactide-co-glycolide).4. Effect of the porcessing parameters on coacervation and encapsulation*. J Controlled Release **35**, 117-125.
- [15] Jyothi NVN, Prasanna PM, et al. (2010). *Microencapsulation techniques, factors influencing encapsulation efficiency*. J Microencapsulation **27**, 187-197.
- [16] Thomasin C, Ho NT, et al. (1998). *Drug microencapsulation by PLA/PLGA coacervation in the light of thermodynamics. 1. Overview and theoretical considerations*. J Pharm Sci **87**, 259-268.
- [17] Thomasin C, Merkle HP, Gander B (1998). *Drug microencapsulation by PLA/PLGA coacervation in the light of thermodynamics. 2. Parameters determining microsphere formation*. J Pharm Sci **87**, 269-275.
- [18] Tewes F, Boury F, Benoit J-P (2006). *Biodegradable Microspheres: Advances in Production Technology*. In: Benita S (ed) *Microencapsulation: Methods and Industrial Applications*. Taylor & Francis, New York,
- [19] Baras B, Benoit MA, Gillard J (2000). *Parameters influencing the antigen release from spray-dried poly(DL-lactide) microparticles*. Int J Pharm **200**, 133-145.
- [20] Vladisavljevic GT, Kobayashi I, Nakajima M (2012). *Production of uniform droplets using membrane, microchannel and microfluidic emulsification devices*. Microfluidics and Nanofluidics **13**, 151-178.

- [21] Crank J (1975). *The Mathematics of Diffusion*. Oxford University Press, UK
- [22] Pessi J, Santos HA, et al. (2014). *Microfluidics-assisted engineering of polymeric microcapsules with high encapsulation efficiency for protein drug delivery*. *Int J Pharm* **472**, 82-87.
- [23] Katzhendler I, Hoffman A, et al. (1997). *Modeling of drug release from erodible tablets*. *J Pharm Sci* **86**, 110-115.
- [24] Cherry EM, Maxim PG, Eaton JK (2010). *Particle size, magnetic field, and blood velocity effects on particle retention in magnetic drug targeting*. *Med Phys* **37**, 175-182.
- [25] Senyei AE, Driscoll CF, Widder KJ (1985). *Biophysical drug targeting: magnetically responsive albumin microspheres*. *Methods Enzymol* **112**, 56-67.
- [26] Whitesides GM (2006). *The origins and the future of microfluidics*. *Nature* **442**, 368-373.
- [27] Stone HA, Stroock AD, Ajdari A (2004). *Engineering flows in small devices: Microfluidics toward a lab-on-a-chip*. *Annual Review of Fluid Mechanics* **36**, 381-411.
- [28] Dendukuri D, Doyle PS (2009). *The Synthesis and Assembly of Polymeric Microparticles Using Microfluidics*. *Adv Mater* **21**, 4071-4086.
- [29] Kawakatsu T, Kikuchi Y, Nakajima M (1997). *Regular-sized cell creation in microchannel emulsification by visual microprocessing method*. *J Am Oil Chem Soc* **74**, 317-321.
- [30] Seemann R, Brinkmann M, et al. (2012). *Droplet based microfluidics*. *Rep Prog Phys* **75**
- [31] Christopher GF, Anna SL (2007). *Microfluidic methods for generating continuous droplet streams*. *J Phys D: Appl Phys* **40**, R319-R336.
- [32] Baroud CN, Gallaire F, Dangla R (2010). *Dynamics of microfluidic droplets*. *Lab Chip* **10**, 2032-2045.
- [33] Herrmann JB, Kelly RJ, Higgins GA (1970). *Polyglycolic acid sutures - laboratory and clinical evaluation of a new absorbable suture material*. *Arch Surg* **100**, 486-&.
- [34] Utada AS, Fernandez-Nieves A, et al. (2007). *Dripping to jetting transitions in coflowing liquid streams*. *Phys Rev Lett* **99**
- [35] Cramer C, Fischer P, Windhab EJ (2004). *Drop formation in a co-flowing ambient fluid*. *Chem Eng Sci* **59**, 3045-3058.
- [36] Anna SL, Bontoux N, Stone HA (2003). *Formation of dispersions using "flow focusing" in microchannels*. *Appl Phys Lett* **82**, 364-366.
- [37] Utada AS, Chu LY, et al. (2007). *Dripping, jetting, drops, and wetting: The magic of microfluidics*. *MRS Bull* **32**, 702-708.
- [38] Anna SL, Mayer HC (2006). *Microscale tipstreaming in a microfluidic flow focusing device*. *Phys Fluids* **18**
- [39] Nie ZH, Seo MS, et al. (2008). *Emulsification in a microfluidic flow-focusing device: effect of the viscosities of the liquids*. *Microfluidics and Nanofluidics* **5**, 585-594.
- [40] Garstecki P, Stone HA, Whitesides GM (2005). *Mechanism for flow-rate controlled breakup in confined geometries: A route to monodisperse emulsions*. *Phys Rev Lett* **94**, 164501.
- [41] Hessel V, Lowe H, Schonfeld F (2005). *Micromixers - a review on passive and active mixing principles*. *Chem Eng Sci* **60**, 2479-2501.
- [42] Lee CY, Chang CL, et al. (2011). *Microfluidic Mixing: A Review*. *Int J Mol Sci* **12**, 3263-3287.

- [43] Nguyen NT, Wu ZG (2005). *Micromixers - a review*. Journal of Micromechanics and Microengineering **15**, R1-R16.
- [44] Lin CH, Tsai CH, Fu LM (2005). *A rapid three-dimensional vortex micromixer utilizing self-rotation effects under low Reynolds number conditions*. Journal of Micromechanics and Microengineering **15**, 935-943.
- [45] Knight JB, Vishwanath A, et al. (1998). *Hydrodynamic focusing on a silicon chip: Mixing nanoliters in microseconds*. Phys Rev Lett **80**, 3863-3866.
- [46] Liu RH, Stremler MA, et al. (2000). *Passive mixing in a three-dimensional serpentine microchannel*. Journal of Microelectromechanical Systems **9**, 190-197.
- [47] Buchegger W, Wagner C, et al. (2011). *A highly uniform lamination micromixer with wedge shaped inlet channels for time resolved infrared spectroscopy*. Microfluidics and Nanofluidics **10**, 889-897.
- [48] Mansur EA, Ye MX, et al. (2008). *A state-of-the-art review of mixing in microfluidic mixers*. Chin J Chem Eng **16**, 503-516.
- [49] Muzykantov V, Torchilin V, et al. (2002). *Biomedical Aspects of Drug Targeting*. Springer US, Boston, MA.
- [50] Stroock AD, Dertinger SKW, et al. (2002). *Chaotic mixer for microchannels*. Science **295**, 647-651.
- [51] Kim DS, Lee SW, et al. (2004). *A barrier embedded chaotic micromixer*. Journal of Micromechanics and Microengineering **14**, 798-805.
- [52] Mae K, Maki T, et al. (2004). *Development of a new micromixer based on split/recombination for mass production and its application to soap free emulsifier*. Chem Eng J **101**, 31-38.
- [53] Steinhaus B, Shen AQ, Sureshkumar R (2007). *Dynamics of viscoelastic fluid filaments in microfluidic devices*. Phys Fluids **19**, 073103.
- [54] Derzsi L, Kasprzyk M, et al. (2013). *Flow focusing with viscoelastic liquids*. Phys Fluids **25**, 092001.
- [55] Fu TT, Wu YN, et al. (2012). *Droplet formation and breakup dynamics in microfluidic flow-focusing devices: From dripping to jetting*. Chem Eng Sci **84**, 207-217.
- [56] Kintses B, van Vliet LD, et al. (2010). *Microfluidic droplets: new integrated workflows for biological experiments*. Curr Opin Chem Biol **14**, 548-555.
- [57] Hufnagel H, Huebner A, et al. (2009). *An integrated cell culture lab on a chip: modular microdevices for cultivation of mammalian cells and delivery into microfluidic microdroplets*. Lab Chip **9**, 1576-1582.
- [58] Bai YP, He XM, et al. (2010). *A double droplet trap system for studying mass transport across a droplet-droplet interface*. Lab Chip **10**, 1281-1285.
- [59] Finehout E, Tian W-C (2009). *Microfluidics for Biological Applications*. Springer-Verlag, Boston, MA.
- [60] Tan YC, Cristini V, Lee AP (2006). *Monodispersed microfluidic droplet generation by shear focusing microfluidic device*. Sensors and Actuators B-Chemical **114**, 350-356.
- [61] Tirtaatmadja V, McKinley GH, Cooper-White JJ (2006). *Drop formation and breakup of low viscosity elastic fluids: Effects of molecular weight and concentration*. Phys Fluids **18**, 043101.
- [62] Wagner C, Amarouchene Y, et al. (2005). *Droplet detachment and satellite bead formation in viscoelastic fluids*. Phys Rev Lett **95**, 164504.

- [63] Zhou CF, Yue PT, Feng JJ (2006). *Formation of simple and compound drops in microfluidic devices*. Phys Fluids **18**, 092105.
- [64] Yue P, Zhou C, et al. (2006). *Phase-field simulations of interfacial dynamics in viscoelastic fluids using finite elements with adaptive meshing*. J Comput Phys **219**, 47-67.
- [65] Sinha VR, Aggarwal A, Trehan A (2004). *Biodegradable PEGylated Microspheres and Nanospheres*. American Journal of Drug Delivery **2**, 157-171.
- [66] Jiang WL, Schwendeman SP (2001). *Stabilization and controlled release of bovine serum albumin encapsulated in poly(D, L-lactide) and poly(ethylene glycol) microsphere blends*. Pharm Res **18**, 878-885.
- [67] Chung TW, Huang YY, Liu YZ (2001). *Effects of the rate of solvent evaporation on the characteristics of drug loaded PLLA and PDLLA microspheres*. Int J Pharm **212**, 161-169.
- [68] Uchida T, Martin S, et al. (1994). *Dose and load studies for subcutaneous and oral delivery of poly(lactide-co-glycolide) microspheres containing ovalbumin*. Pharm Res **11**, 1009-1015.
- [69] Häfeli UO, Saatchi K, et al. (2010). *Lung perfusion imaging with monosized biodegradable microspheres*. Biomacromolecules **11**, 561-567.
- [70] Torchilin VP (2006). *Nanoparticulates as drug carriers*. Imperial College Press, Hackensack, N.J;London;.
- [71] Devarajan PV, Jain S, et al. (2015). *Targeted Drug Delivery: Concepts and Design*. Springer International Publishing, Cham.
- [72] Mallol J, Diaz RV (1997). *Particle size and its mathematical distribution in six human albumin macroaggregate (MAA) kits*. Nucl Med Commun **18**, 87-88.
- [73] Saatchi K, Häfeli UO (2007). *One-pot syntheses, coordination and characterization of application-specific biodegradable ligand-polymers*. Dalton Trans **39**, 4439-4445.
- [74] Zastre J, Jackson J, et al. (2002). *Enhanced cellular accumulation of a P-glycoprotein substrate, rhodamine-123, by Caco-2 cells using low molecular weight methoxypolyethylene glycol-block-polycaprolactone diblock copolymers*. Eur J Pharm Biopharm **54**, 299-309.
- [75] Salem R, Thurston KG (2006). *Radioembolization with yttrium-90 microspheres: A state-of-the-art brachytherapy treatment for primary and secondary liver malignancies - Part 3: Comprehensive literature review and future direction*. J Vasc Interv Radiol **17**, 1571-1593.
- [76] Kennedy A, Coldwell D, et al. (2012). *Radioembolization for the Treatment of Liver Tumors General Principles*. American Journal of Clinical Oncology-Cancer Clinical Trials **35**, 91-99.
- [77] Stickel JJ, Powell RL (2005). *Fluid mechanics and rheology of dense suspensions*. Annual Review of Fluid Mechanics, vol 37, 129-149.
- [78] Cristini V, Tan YC (2004). *Theory and numerical simulation of droplet dynamics in complex flows - a review*. Lab Chip **4**, 257-264.
- [79] Worner M (2012). *Numerical modeling of multiphase flows in microfluidics and micro process engineering: a review of methods and applications*. Microfluidics and Nanofluidics **12**, 841-886.

- [80] Chen AU, Notz PK, Basaran OA (2002). *Computational and experimental analysis of pinch-off and scaling*. Phys Rev Lett **88**, 174501.
- [81] Yue PT, Zhou CF, Feng JJ (2006). *A computational study of the coalescence between a drop and an interface in Newtonian and viscoelastic fluids*. Phys Fluids **18**, 102102.
- [82] Yue PT, Zhou CF, Feng JJ (2007). *Spontaneous shrinkage of drops and mass conservation in phase-field simulations*. J Comput Phys **223**, 1-9.
- [83] Zhou CF, Yue PT, et al. (2010). *3D phase-field simulations of interfacial dynamics in Newtonian and viscoelastic fluids*. J Comput Phys **229**, 498-511.
- [84] Shaw S, Murthy PVS, Sibanda P (2013). *Magnetic drug targeting in a permeable microvessel*. Microvasc Res **85**, 77-85.
- [85] Lübke AS, Alexiou C, Bergemann C (2001). *Clinical Applications of Magnetic Drug Targeting*. J Surg Res **95**, 200-206.
- [86] Pankhurst QA, Connolly J, et al. (2003). *Applications of magnetic nanoparticles in biomedicine*. J Phys D: Appl Phys **36**, R167-R181.
- [87] Ammar S, Deisenhofer I, et al. (2014). *Remote-controlled magnetic navigation and ablation of atrial flutter in a patient with an extracardiac total cavopulmonary connection*. Clin Res Cardiol **103**, 753-754.
- [88] Gillies GT, Ritter RC, et al. (1994). *Magnetic manipulation instrumentation for medical physics research* Rev Sci Instrum **65**, 533-562.
- [89] Hayden ME, Häfeli UO (2006). *'Magnetic bandages' for targeted delivery of therapeutic agents*. J Phys : Condens Matter **18**, S2877-S2891.
- [90] Iacob G, Rotariu O, et al. (2004). *Magnetizable needles and wires - modeling an efficient way to target magnetic microspheres in vivo*. Biorheology **41**, 599-612.
- [91] Kempe H, Kempe M (2010). *The use of magnetite nanoparticles for implant-assisted magnetic drug targeting in thrombolytic therapy*. Biomaterials **31**, 9499-9510.
- [92] Brule S, Levy M, et al. (2011). *Doxorubicin Release Triggered by Alginate Embedded Magnetic Nanoheaters: A Combined Therapy*. Adv Mater **23**, 787-790.
- [93] Dutz S, Kettering M, et al. (2011). *Magnetic multicore nanoparticles for hyperthermia-influence of particle immobilization in tumour tissue on magnetic properties*. Nanotechnology **22**, 265102.
- [94] Häfeli UO (2004). *Magnetically modulated therapeutic systems*. Int J Pharm **277**, 19-24.
- [95] Gilchrist RK, Medal R, et al. (1957). *Selective inductive heating of lymph nodes*
- [96] Meyers PH, Nice CM, Cronin F (1963). *Experimental approach in use and magnetic control of metallic iron particles in lymphatic and vascular system of dogs as a contrast and isotopic agent*. American Journal of Roentgenology Radium Therapy and Nuclear Medicine **90**, 1068-&.
- [97] Kato T, Nemoto R, et al. (1984). *Magnetic microcapsules for targeted delivery of anticancer drugs*. Appl Biochem Biotechnol **10**, 199-211.
- [98] Widder KJ, Morris RM, et al. (1981). *Tumor remission in Yoshida sarcoma-bearing rats by selective targeting of magnetic albumin microspheres containing doxorubicin*. Proc Natl Acad Sci U S A ; Biological Sciences **78**, 579-581.
- [99] Jordan A, Wust P, et al. (1993). *Inductive heating of ferrimagnetic particles and magnetic fluids - physical evaluation of their potential for hyperthermia* Int J Hyperthermia **9**, 51-68.

- [100] Dutz S, Hergt R (2014). *Magnetic particle hyperthermia-a promising tumour therapy?* Nanotechnology **25**, 452001.
- [101] Hilger I (2013). *In vivo applications of magnetic nanoparticle hyperthermia.* Int J Hyperthermia **29**, 828-834.
- [102] Müller R, Dutz S, et al. (2013). *Magnetic heating effect of nanoparticles with different sizes and size distributions.* J Magn Magn Mater **328**, 80-85.
- [103] Mahmoudi M, Simchi A, et al. (2010). *A new approach for the in vitro identification of the cytotoxicity of superparamagnetic iron oxide nanoparticles.* Colloids and Surfaces B: Biointerfaces **75**, 300-309.
- [104] Gupta AK, Gupta M (2005). *Synthesis and surface engineering of iron oxide nanoparticles for biomedical applications.* Biomaterials **26**, 3995-4021.
- [105] Saville SL, Stone RC, et al. (2012). *Investigation of the stability of magnetite nanoparticles functionalized with catechol based ligands in biological media.* J Mater Chem **22**, 24909-24917.
- [106] Veisoh O, Gunn JW, Zhang MQ (2010). *Design and fabrication of magnetic nanoparticles for targeted drug delivery and imaging.* Adv Drug Delivery Rev **62**, 284-304.
- [107] Stone RC, Qi B, et al. (2014). *A versatile stable platform for multifunctional applications: synthesis of a nitroDOPA-PEO-alkyne scaffold for iron oxide nanoparticles.* Journal of Materials Chemistry B **2**, 4789-4793.
- [108] Amstad E, Gillich T, et al. (2009). *Ultrastable Iron Oxide Nanoparticle Colloidal Suspensions Using Dispersants with Catechol-Derived Anchor Groups.* Nano Lett **9**, 4042-4048.
- [109] Osman MA, Atallah A (2006). *Effect of the particle size on the viscoelastic properties of filled polyethylene.* Polymer **47**, 2357-2368.
- [110] Zubarev AY, Fleischer J, Odenbach S (2005). *Towards a theory of dynamical properties of polydisperse magnetic fluids: Effect of chain-like aggregates.* Phys A (Amsterdam, Neth) **358**, 475-491.
- [111] Yamada K, Oda T, et al. (2010). *Minimally required heat doses for various tumour sizes in induction heating cancer therapy determined by computer simulation using experimental data.* Int J Hyperthermia **26**, 465-474.
- [112] Shardt O, Derksen JJ, Mita SK (2013). *Simulations of Droplet Coalescence in Simple Shear Flow.* Langmuir **29**, 6201-6212.
- [113] Zhao H, Saatchi K, Häfeli UO (2009). *Preparation of biodegradable magnetic microspheres with poly(lactic acid)-coated magnetite.* J Magn Magn Mater **321**, 1356-1363.
- [114] Sen D, Bahadur J, et al. (2012). *Formation of hollow spherical and doughnut microcapsules by evaporation induced self-assembly of nanoparticles: effects of particle size and polydispersity.* Soft Matter **8**, 10036-10044.
- [115] Cui MM, Emrick T, Russell TP (2013). *Stabilizing Liquid Drops in Nonequilibrium Shapes by the Interfacial Jamming of Nanoparticles.* Science **342**, 460-463.
- [116] Qi F, Wu J, et al. (2014). *Mechanistic studies for monodisperse exenatide-loaded PLGA microspheres prepared by different methods based on SPG membrane emulsification.* Acta Biomaterialia **10**, 4247-4256.

- [117] Pai SS, Tilton RD, Przybycien TM (2009). *Poly(ethylene glycol)-Modified Proteins: Implications for Poly(lactide-co-glycolide)-Based Microsphere Delivery*. *Aaps J* **11**, 88-98.
- [118] Determan AS, Trewyn BG, et al. (2004). *Encapsulation, stabilization, and release of BSA-FITC from polyanhydride microspheres*. *J Controlled Release* **100**, 97-109.
- [119] Yang YY, Chung TS, Ng NP (2001). *Morphology, drug distribution, and in vitro release profiles of biodegradable polymeric microspheres containing protein fabricated by double-emulsion solvent extraction/evaporation method*. *Biomaterials* **22**, 231-241.
- [120] Freiberg S, Zhu X (2004). *Polymer microspheres for controlled drug release*. *Int J Pharm* **282**, 1-18.
- [121] Gopferich A (1996). *Mechanisms of polymer degradation and erosion*. *Biomaterials* **17**, 103-114.
- [122] Abbaspourrad A, Carroll NJ, et al. (2013). *Polymer Microcapsules with Programmable Active Release*. *J Am Chem Soc* **135**, 7744-7750.
- [123] Adams LLA, Kodger TE, et al. (2012). *Single step emulsification for the generation of multi-component double emulsions*. *Soft Matter* **8**, 10719-10724.
- [124] Chu LY, Utada AS, et al. (2007). *Controllable monodisperse multiple emulsions*. *Angewandte Chemie-International Edition* **46**, 8970-8974.
- [125] Okushima S, Nisisako T, et al. (2004). *Controlled production of monodisperse double emulsions by two-step droplet breakup in microfluidic devices*. *Langmuir* **20**, 9905-9908.
- [126] Utada AS, Lorenceau E, et al. (2005). *Monodisperse double emulsions generated from a microcapillary device*. *Science* **308**, 537-541.
- [127] Wang W, Zhang MJ, Chu LY (2014). *Microfluidic approach for encapsulation via double emulsions*. *Curr Opin Pharmacol* **18**, 35-41.
- [128] Deng NN, Mou CL, et al. (2014). *Multiple emulsion formation from controllable drop pairs in microfluidics*. *Microfluidics and Nanofluidics* **17**, 967-972.
- [129] Abate AR, Weitz DA (2009). *High-Order Multiple Emulsions Formed in Poly(dimethylsiloxane) Microfluidics*. *Small* **5**, 2030-2032.
- [130] Srinivasan U, Houston MR, et al. (1998). *Alkyltrichlorosilane-based self-assembled monolayer films for stiction reduction in silicon micromachines*. *Journal of Microelectromechanical Systems* **7**, 252-260.
- [131] Fuchs A, Kanoufi F, et al. (2007). *Wetting and surface properties of (modified) fluorosilanised glass*. *Colloids and Surfaces a-Physicochemical and Engineering Aspects* **307**, 7-15.
- [132] Link DR, Anna SL, et al. (2004). *Geometrically mediated breakup of drops in microfluidic devices*. *Phys Rev Lett* **92**
- [133] Fuerstman MJ, Lai A, et al. (2007). *The pressure drop along rectangular microchannels containing bubbles*. *Lab Chip* **7**, 1479-1489.
- [134] Bokharaei M, Schneider T, et al. (2016). *Production of monodispersed magnetic polymeric microspheres in a microfluidic chip and 3D simulation*. *Microfluidics and Nanofluidics* **20**, 1-14.
- [135] Bahrami M, Yovanovich MM, Culham JR (2006). *Pressure drop of fully-developed laminar flow in microchannels of arbitrary cross-section*. *Journal of Fluids Engineering-Transactions of the Asme* **128**, 1036-1044.

- [136] Katou H, Wandrey AJ, Gander B (2008). *Kinetics of solvent extraction/evaporation process for PLGA microparticle fabrication*. Int J Pharm **364**, 45-53.
- [137] Langer R, Folkman J (1976). *Polymers for sustained release proteins and other macromolecules*. Nature **263**, 797-800.
- [138] Ghate D, Edelhauser HF (2006). *Ocular Drug Delivery*. Expert opinion **3**, 275-287.
- [139] Janoria KG, Gunda S, et al. (2007). *Novel Approaches to retinal Drug Delivery*. Expert opinion **4**, 371-388.
- [140] Sigurdsson HH, Konraosdottir F, et al. (2007). *Topical and systemic absorption in delivery of dexamethasone to the anterior and posterior segments of the eye*. Acta Ophthalmol Scand **85**, 598-602.
- [141] Xu QB, Hashimoto M, et al. (2009). *Preparation of monodisperse biodegradable polymer microparticles using a microfluidic mlow-focusing device for controlled drug delivery*. Small **5**, 1575-1581.